

Sky Coverage Computation for the Surface Detector of the Pierre Auger Observatory

DIPLOMARBEIT
zur Erlangung des akademischen Grades
Diplom-Physiker

vorgelegt von
Marius Grigat,
geboren am 31. August 1979 in Waldbröl,

eingereicht beim Fachbereich Physik
der Universität Siegen

Siegen
Juli 2007

Contents

1	Introduction	1
1.1	Cosmic Rays	1
1.1.1	History	1
1.1.2	Energy Spectrum	2
1.2	Air Showers	4
1.2.1	Hadronic Component	4
1.2.2	Electromagnetic Component	5
1.2.3	Muonic Component	6
1.2.4	Neutrino Component	6
1.3	Anisotropy	6
1.4	Scope of This Thesis	7
2	Pierre Auger Observatory	9
2.1	Detection Techniques	10
2.1.1	Surface Detector (SD)	10
2.1.2	Fluorescence Detector (FD)	11
2.1.3	Hybrid Detector	11
2.1.4	Radio Detector	13
2.2	SD Triggers and Data Acquisition	14
2.2.1	Local Triggers	14
2.2.2	Event Triggers	14
2.2.3	Quality Trigger	15
2.2.4	Tank Trigger Efficiency	16
2.3	SD Reconstruction	16
2.3.1	Energy Estimation	17
3	Angular Reconstruction for the Surface Detector	21
3.1	Estimation of Arrival Times	21
3.2	Angular Resolution	24
3.2.1	Time Variance Model	24
3.3	Conclusions	26
4	Celestial Positioning	27
4.1	Reference Frames	28
4.1.1	Geographic Coordinates	28
4.1.2	Horizontal Coordinates	28

4.1.3	Equatorial Coordinates	28
4.1.4	Galactic Coordinates	31
4.2	The HEALPix Pixelization	31
5	Sky Coverage	35
5.1	Data Set of Real Showers	35
5.1.1	Skymap of Events	36
5.1.2	Azimuth Angle Distribution	37
5.2	Shuffling	37
5.2.1	Shuffling JD	39
5.2.2	Shuffling JD_{int} and JD_{rest}	39
5.2.3	Julian Day Distributions	40
5.2.4	Advantages and Drawbacks	42
5.3	Semi-Analytical	42
5.3.1	Polynomial Zenith Angle Fit	43
5.3.2	Physical Zenith Angle Fit	43
5.3.3	Comparison of Fits	45
5.4	Coverage Maps	45
5.5	Full Acceptance	48
5.5.1	Zenith Angle Distribution	48
5.5.2	Coverage Maps	50
6	Averaging on Lines of Constant Declination	55
6.1	Declination Profiles	57
6.2	Spread around Mean	57
6.3	Conclusions	60
7	Zenith Angle Distributions of Fake Sources and Fake Isotropy	65
7.1	Point Sources	65
7.2	Zenith Angle Distributions	67
7.3	Conclusions	69
8	Summary and Outlook	71
A	Factorizable Acceptance Model	73
	List of Figures	76
	List of Tables	77
	List of Acronyms	79
	Bibliography	81
	Acknowledgement	85

Chapter 1

Introduction

1.1 Cosmic Rays

Highly energetic particles coming from outer space are permanently hitting and penetrating the Earth's atmosphere. The charged part of these is commonly referred to as cosmic radiation, which mainly consists of ionized nuclei (98%) such as protons (87%), α -particles (12%) and heavier nuclei (1%); electrons yield the remaining 2%. Neutrinos and photons finally make up the neutral part of the incoming particles [Lon92].

1.1.1 History

In 1785, Henry Coulomb observed the ionizing effect of cosmic radiation, when he found, that a simple electroscope loses its charge though being well insulated. After the discovery of radioactivity in 1896 by Becquerel, it was believed, that ionization by naturally radioactive material could explain the charge leakage.

A series of experiments followed, investigating this phenomenon and its dependence on altitude above ground, i.e. distance to the potential sources. Measurements on the Eiffel tower [Wul09] showed a significant drop of the ionization rate. In order to increase the distance to ground Victor Hess performed balloon flights in 1912, reaching altitudes of 5300m. He found out, that the ionizing radiation indeed diminished up to 1500m, then started to increase again finally reaching even larger rates at 3600m compared to ground level [Hes12]. This led to the idea of an extraterrestrial origin of the radiation. Further experiments could establish this idea and even show, that the radiation was of extrasolar origin.

In 1925 Robert Millikan discovered, that this cosmic radiation was capable of causing changes of the atmospheric composition; the interactions of cosmic rays and particles of the Earth's atmosphere, i.e. usually nitrogen nuclei, produce secondary particles, which themselves may interact with atmospheric constituents. The particles produced during this process are referred to as secondary cosmic rays. A few years after Millikan's explorations of cosmic rays and secondary particles, the first individual particles could be identified by means of photographic plates and cloud chambers, e.g. the pion, the muon, the kaon and the positron.

In the late 1930s, while the Nobel prize was given to Victor Hess in 1936, Pierre Auger observed time coincidences of particle detections in horizontally separated detec-

energy	10^{12} eV	10^{14} eV	10^{16} eV	10^{18} eV	10^{20} eV
flux	$10/m^2$ min	$5/m^2$ d	$1/m^2$ y	$65/km^2$ y	$0.005/km^2$ y

Table 1.1: Typical values for the correlation between primary energy and particle flux.

tors on ground level [Aug38]. Relying on Millikan's investigations his conclusion was to assume a common origin of these coincidentally measured particles. Cosmic ray primaries initiate cascades of secondary particles originating from the point of interaction with an atmospheric constituent. The measurement of these cascades, commonly referred to as air showers, provided a first means to estimate an upper limit of the energy of cosmic rays.

While Pierre Auger was capable of measuring energies to an upper limit of 10^{15} eV, the energy range of cosmic particles as being measured in several air shower experiments during the last decades continuously grew up to 10^{20} eV. The highest energetic cosmic ray event reported so far was recorded in 1994 by the Fly's Eye experiment at an energy of $3.2 \cdot 10^{20}$ eV.

1.1.2 Energy Spectrum

The energy spectrum of cosmic rays can be described as the particle flux I depending on the energy E . The differential expression commonly used as an approximation for several orders of magnitude is the following power law:

$$\frac{dI}{dE} \propto E^{-\gamma}, \quad (1.1)$$

where γ is called the spectral index. For energies starting from 10^{11} eV γ equals 2.7. A convex bent in the spectrum around $3 \cdot 10^{15}$ eV, often being referred to as the 'knee', corresponds to an increasing spectral index: γ changes to 3.1. At $3 \cdot 10^{18}$ eV, it returns to a value of 2.7, corresponding to a concave bent of the spectrum curve, the so-called 'ankle' (see figure (1.1)). For energies beyond $6 \cdot 10^{19}$ eV Greisen, Zatsepin and Kuzmin predicted a cut-off of the flux (GZK cut-off); at this limit, primary particles are supposed to start interacting with cosmic microwave background (CMB) photons [Gre66]. This was found shortly after the detection of the CMB in the 1960s [Pen65]. Some values of the flux are given in table 1.1 for typical energies.

The altitude of cascade initiation by a primary cosmic particle typically is 20km. Therefore only satellite and balloon experiments are applicable to measure cosmic rays directly. For obvious reasons, this limits the detection area, so that only primaries below 10^{15} eV may be measured directly with reasonably high statistics. Alternatively, ground experiments are suitable to detect secondary particles, that yield information about their origin i.e. the cosmic ray primary. On ground level, huge detection areas allow to access energies up to several 10^{21} eV with sufficient statistics. Therefore, it is necessary to investigate and understand the properties of air showers.

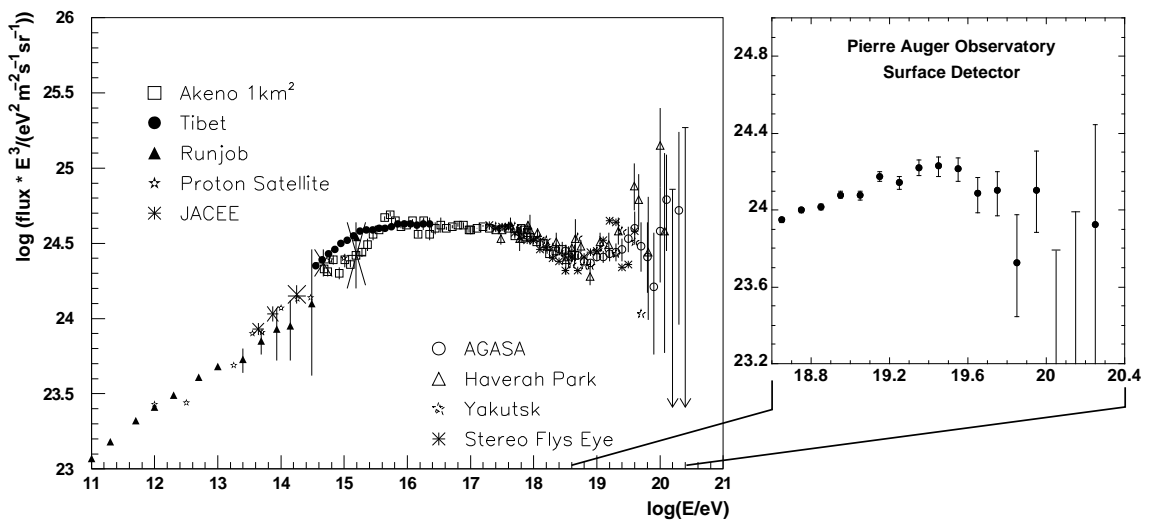


Figure 1.1: Left: cosmic ray energy spectrum for all particles: direct measurements below 10^{16} eV by JACEE, RUNJOB and Proton Satellite; indirect measurements above 10^{18} eV by AGASA, Haverah Park, Yakutsk and Fly's Eye [Nag00]. For the sake of visibility considering the structures of the spectrum as discussed in the text, the flux has been multiplied by the third power of the energy. Right: estimated differential energy spectrum by the surface detector (SD) of the Pierre Auger Observatory, July 2007 [Yam07]. The scales of both the flux and the energy axis are the same as for the spectrum on the left. Error bars on points indicate statistical uncertainty. Systematic uncertainty is dominantly affected by the 21 % uncertainty in the energy scale of the fluorescence detector, which is used here for the calibration of the SD energy. Events are included for zenith angles $0^\circ - 60^\circ$, energies above ~ 3 EeV are reported.

particle type	photons	electrons	muons	hadrons
percentage	80%	18%	1.7%	0.3%

Table 1.2: Integral composition of secondary particles: relative amount of particles produced during the development of an air shower in the atmosphere

1.2 Air Showers

When a cosmic ray particle hits the Earth's atmosphere, it undergoes a nuclear reaction with an atmospheric constituent. In most cases, this would be the nucleus of a nitrogen atom, according to the composition of the atmosphere. This first interaction forms a multitude of secondary particles, which themselves interact with atmospheric constituents, thus initiating a cascade (see figure 1.2, left). The particles in such an air shower form a disc with a thickness of a few meters and a lateral diameter of up to some kilometers (see figure 1.2, right), depending on energy and type of the primary particle. Furthermore, the thickness of this disc is small at the shower center, while increasing to its edge. The shower disc propagates through the atmosphere with the speed of light, virtually; despite the curved shape the shower front can be considered as plane in first order approximation.

The number of particles being produced rises with the total energy of the primary. A proton at an energy of 10^{15} eV for example produces 10^6 secondary particles [Gru00]. The instantaneous number of particles varies while the air shower propagates in atmosphere. It firstly rises as described by the cascade like process. As soon as the particle energies drop below the production limit of new secondaries, the number of particles falls exponentially with atmospheric depth. The ground distance of the point, where the shower reaches its maximum number of particles is commonly called X_{max} .

Cosmic rays at high energies generate extensive air showers, whose secondary particles are capable of reaching the Earth's surface. The integral composition of secondary particles, as being produced during the development of an air shower, is given by table 1.2. These particles are not only created by hadronic, but also by electromagnetic interaction; the corresponding components of an air shower will be described in the following subsections.

1.2.1 Hadronic Component

When a hadron (most likely a proton) enters the atmosphere, it collides with atmospheric constituents being subject to strong interaction. In case the primary is a proton this first collision will take place in an altitude of 15 to 20 km because of the proton interaction length of 90 g/cm^2 [Gru05]. Thus a hadronic cascade is initiated producing secondary particles, i.e. mostly pions. Kaon production on the other hand is less likely with a relative probability of 10% compared to pions. Charged pions are supposed to be subject to further hadronic interaction, whereas neutral pions decay most likely $\pi^0 \rightarrow 2\gamma$, as the decay life time of the latter is much shorter than the interaction length.

The transverse momenta of highly energetic hadrons on average is rather low compared to their total momenta; thus, they are concentrated within a radius of ~ 10 m around the shower axis. When the energy of a hadron drops below the pion production threshold,

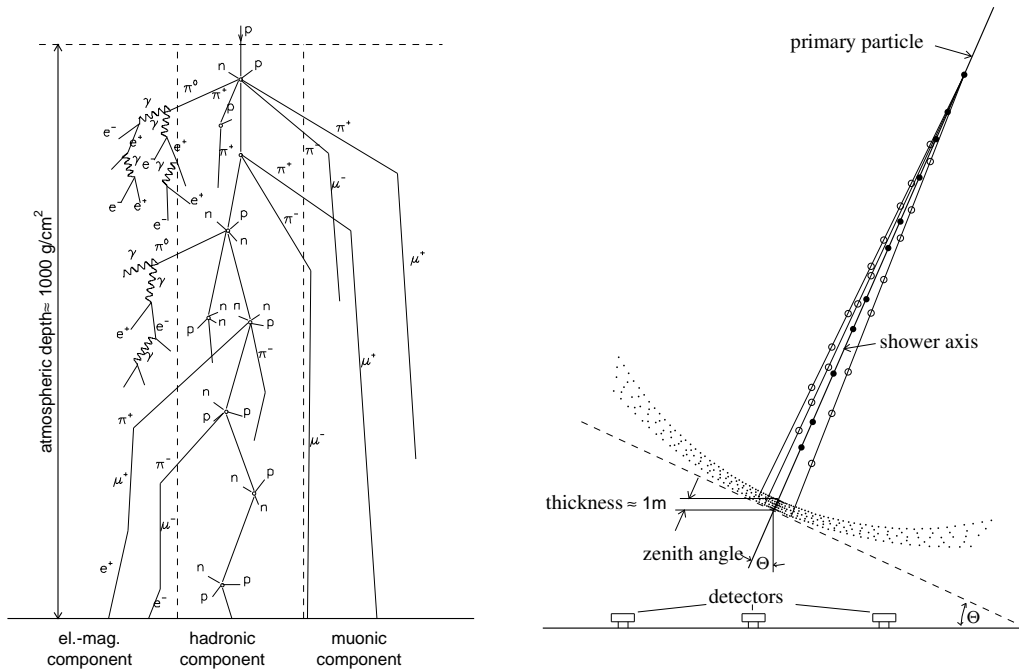


Figure 1.2: Schematic view of an extensive air shower [Alk75].

it loses energy through ionization until it decays or is stopped.

1.2.2 Electromagnetic Component

The π^0 decay initiates an electromagnetic cascade; the γ 's produced generate $e^+ e^-$ pairs (pair production), that in turn create new γ 's via bremsstrahlung, thus forming a cascade. Other electromagnetic interactions like photo-electric effect, Compton effect (photons) and ionization (electrons) can be neglected with respect to the high energies necessary for the cascade development [Rao98]. The short radiation length of electrons and photons in air (36.66 g/cm^2) results in a rapid absorption of these particles, therefore commonly being referred to as the soft component. An electromagnetic cascade will also be initiated by a primary electron; in this case the generation of a hadronic component in turn is unlikely.

The lateral spread of the electromagnetic component of an air shower reaches values of up to several kilometers depending on energy. This lateral development is due to multiple Coulomb scattering; the corresponding lateral density function (LDF) can model this development, which is commonly done by the so-called Nishimura-Kamata-Greisen (NKG) approach [Gre56]

$$\Delta(N_e, r) = \frac{N_e}{2\pi r_0^2} \frac{\Gamma(4.5 - s)}{\Gamma(s)\Gamma(4.5 - 2s)} \left(\frac{r}{r_0}\right)^{(s-2)} \left(1 + \frac{r}{r_0}\right)^{(s-4.5)}, \quad (1.2)$$

where $\Delta(N_e, r)$ is the area density of particles (per m^2) at distance r from the shower axis in a plane perpendicular to this axis; N_e is the total number of particles in the shower

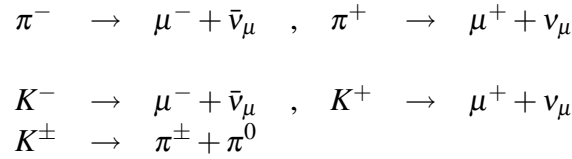


Table 1.3: Muon production / decay of charged mesons.

(shower size), s parameterizes the age of the shower and r_0 is the Molière radius. According to Greisen referring to the exponential nature of the atmosphere, r_0 should be taken at 2 radiation lengths above observation level, e.g. at sea level it is 81 m. The shower age is $s = 0$ at the point of shower initiation, $s = 1$ at the shower maximum and $s = 2$ at the point where the shower dies out. The validity of the NKG function ranges from $0.8 < s < 1.6$.

1.2.3 Muonic Component

80 % of the charged particles reaching sea-level are muons. They are produced by the decay of charged mesons; the decay modes given by table 1.3 are dominant. Muons live 100 times longer than pions; moreover, their range is extended by relativistic time dilatation enabling them to reach the Earth's surface. Suffering less from scattering compared to electrons, muons spread only little with respect to their lateral development.

1.2.4 Neutrino Component

Neutrinos in an air shower primarily are generated by both muon and pion decay. They play an inferior role in EAS measurement, as their interaction cross section is very low, thus providing only small statistics. However, for the same reason (inter alia) neutrino astronomy is an important issue:

- neutrinos as primary particles do not suffer from early decay during their travel from source to Earth;
- neutrinos are not influenced by magnetic fields and are penetrating as well; thus, their incoming direction points back directly to their source;
- it is possible to distinguish between neutrino and antineutrino, which basically allows to find out whether their source was matter or antimatter;

These advantages include one big disadvantage, the same that makes them useless for EAS measurement; the small interaction cross section results in a huge difficulty to detect neutrinos on Earth.

1.3 Anisotropy

The distribution of arrival directions of cosmic ray primaries is remarkably uniform. Especially for the huge statistics of particles with energies below 10^{14} eV only 0.5 % deviation from isotropy was observed.

As cosmic rays are charged particles, they suffer from galactic and extragalactic magnetic fields while travelling through outer space. Thus, directional information originally carried by the particles may be lost, depending on the energy of the primary, the distance of its origin and strength and topology of the magnetic field it is exposed to. Since the deflection decreases at higher energies, it is not too unlikely, that the arrival directions of highest energy cosmic ray primaries point back almost directly to their sources. The fact, that gyration radii are expected to be rather large at these high energies (e.g. estimations yield a few hundred parsec at 10^{18} eV for a field strength of $1.4 \mu\text{G}$), does not reduce the necessity to take into account the magnetic fields and even their evolution through the last tens of million years; sources may easily reside at distances larger than 10 Mpc corresponding to $32.6 \cdot 10^6$ ly [Gru00]. Unfortunately, only little is known about the topology of such fields. However, the AGASA experiment has seen clusters of primary directions in a few events beyond $4 \cdot 10^{19}$ eV. Assuming isotropy, the observation of such clustering has a chance probability of less than 1% [Tak99]. This may not only indicate possible anisotropies, but also yield an upper limit on the influence of the magnetic fields on cosmic rays.

1.4 Scope of This Thesis

The main issue of this thesis is the computation of coverage maps for the Pierre Auger Observatory. Coverage maps provide a view of the visible part of the sky as seen by the observatory. The computation of the sky coverage is a necessary tool in anisotropy search, as it allows comparison with sky maps of the events recorded and reconstructed by the experiment.

- The following chapter 2 contains a brief introduction to the Pierre Auger Observatory in general.
- Chapter 3 deals with the angular reconstruction performed by the surface detector of the Pierre Auger experiment. Furthermore the angular resolution will be discussed.
- The different reference frames for the display of celestial positions and directions are presented in chapter 4; the transformations between some of them are given.
- In chapter 5, several methods of coverage map computation are presented and discussed. A comparison of the coverage maps obtained from these procedures is given.
- An inherent quality check strongly correlated to the assumption of isotropy is investigated in chapter 6.
- Chapter 7 is dedicated to the investigation of the impact of point sources on the coverage. Furthermore, fake isotropy will be created in order to display the purely geometric detector acceptance at full efficiency.
- Finally, chapter 8 summarizes the contents of this thesis, including a brief outlook on possible further studies.

Chapter 2

Pierre Auger Observatory

The southern part of the Pierre Auger Observatory (PAO) is located in the Pampa Amarilla, near Malargüe in the province of Mendoza, Argentina. It is an air shower experiment dedicated to the measurement of extensive air showers as being initiated by ultra high energy cosmic rays (UHECR), which carry energies ranging from 10^{17} eV (0.1 EeV) to 10^{21} eV (1000 EeV). The PAO combines two complementary observation techniques to a hybrid approach: the detection of particles at ground and the observation of associated fluorescence light generated in the atmosphere above the ground.

Several almost unique conditions resulted in the selection of the Pampa as the optimum place for such a measurement. The experiment is set up on an elevated plain at the base of the Andes mountains. The plateau has an altitude of 1400 m above sea-level, corresponding to an atmospheric depth of $X_0 = 875$ g/cm². The Andes act as a shield, thus forwarding almost perfect weather conditions during the entire year. Only little precipitation can be measured, while Malargüe weather statistics promise mostly clear sky. The advantage of the altitude of the observatory obviously is the decrease of distance to the shower maximum. X_{max} typically is situated in a few kilometers height above sea level, depending on energy and inclination; therefore, being on this elevated height, many showers may be recorded with higher statistics.

By the indirect measurement of UHECRs the PAO aims at solving today's cosmological puzzles. Certainly, one of the main issues is the validation of the GZK cut-off. For that reason it is of huge importance to discover the origin of high energy cosmic rays and understand the underlying acceleration mechanisms. Further issues are the estimation of location and distance of potential sources, as well as the investigation of strength and topology of galactic and extra-galactic magnetic fields.

Therefore, a hybrid detector concept is applied, based on both a surface array of water Cherenkov tanks and fluorescence detectors. The 1600 water tanks ($\frac{3}{4}$ of them employed and operating by May 2007) cover an area of 3000 km² (figure 2), which is surrounded by four×six fluorescence telescopes observing the above sky. Data taking started on a trial basis by means of a preliminary set of surface detectors and one telescope site, the so-called engineering array (EA). A second observatory, being referred to as Auger North, will be build on the northern hemisphere in Colorado in the near future.

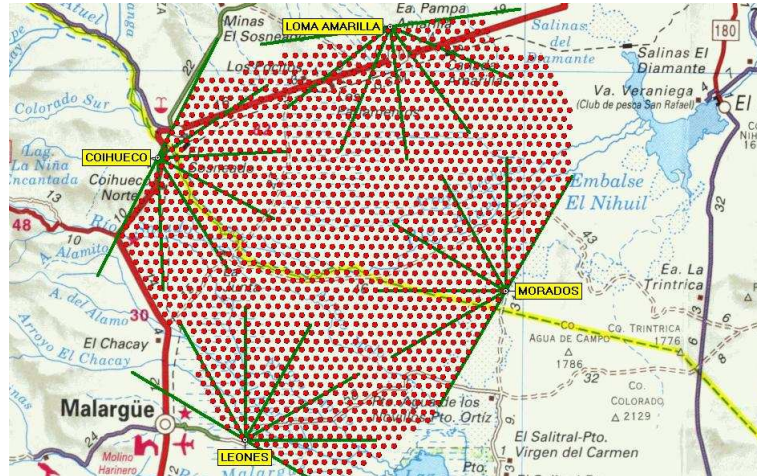


Figure 2.1: Pierre Auger Observatory in the Pampa Amarilla (Yellow Pampa) near Malargüe [PAO07]: The map shows the array of SD tanks (red) surrounded by the FD telescope eyes (green); the array covers an area of 3000 km^2 ; the field of view of each telescope eye is $30^\circ \times 180^\circ$.

2.1 Detection Techniques

2.1.1 Surface Detector (SD)

The 1600 tanks of the Auger SD are uniformly distributed on a hexagonal grid, facing each other in a distance of 1500 m. This spatial alignment yields full efficiency for EAS detection above $10^{18.5} \text{ eV}$ [Kam04]. The trigger efficiency of the SD tank is shown in section 2.2.4 as a function of energy deposit, i.e. signal size in the tank triggered, and zenith angle. Every tank has cylindrical shape covering an area of 10 m^2 with a height of 1.2 m, as shown in figure 2.2. Thus, the surface array covers a detection area of $3 \cdot 10^9 \text{ m}^2$ with an instrumented area of $1.6 \cdot 10^5 \text{ m}^2$. 10 tons of water are filled in each tank, purified to a quality of about $15 \text{ M}\Omega\text{cm}$. Each tank is powered independently by its own stand-alone solar panel and battery system. A GPS (Global Positioning System) antenna provides positioning of each tank at a resolution of $\sim 10 \text{ m}$. Data is transferred via a wireless communication system.

Cosmic rays of energies beyond 10^{14} eV produce a large number of secondary particles, of whom a significant fraction may reach the Earth's surface. If these ionizing shower particles enter a detector tank, they will penetrate the water with a speed faster than that of light in water, thus producing Cherenkov radiation. More specific, this light is produced by traversing muons and electrons. It is supposed to be reflected by the white diffusive Tyvek(R) layer that covers the tank walls. Three photomultiplier tubes (PMT) facing the tank's bottom independently are capable of detecting the light reflections. PMT signals from both the anode and the last dynode are continuously sampled every 25 ns by 10 bit FADCs, yielding a dynamic signal range of 15 bits. Ring buffer memories read the digitized signals on the one hand to allow first and second level trigger conditions to be processed, and on the other hand to keep the data ready for transfer to the Central Data Acquisition System (CDAS) in case of a three-fold shower trigger coincidence of adjacent

tanks (section 2.2).

The surface tanks are self calibrating making use of single cosmic muons. The average charge signal caused by a vertically penetrating muon was chosen to be the basic signal unit (Vertical Equivalent Muon, VEM). The corresponding photocurrent is called I_{VEM}^{est} [All05]. For further calibration studies based on real data, twin (and triplet) tanks have been installed. These are pairs (triples) of SD tanks positioned only 11 m distant from each other, therefore seeing almost the same part of the shower. From the particles' arrival times measured in the detectors, one can determine the shower direction at a resolution of the order of $\sim 1^\circ$ (section 3.2). Besides, the energy deposit in the detectors yields a measure of the number of particles.

2.1.2 Fluorescence Detector (FD)

24 telescopes surround the surface array, six being housed in each of the four 'eyes'. The telescopes' field of view measures $30^\circ \times 30^\circ$ each; the observation direction of their individual center is inclined to 16° altitude. Thus, each eye provides a lateral view of 180° towards the array center, observing the above sky between 1° and 31° .

The ionizing particles of an air shower excite nitrogen molecules while penetrating the atmosphere. When in turn falling back to ground state, these molecules emit fluorescence light in the ultra violet range. The optical telescopes are sensitive to this range and allow imaging the track of the air shower propagating through the atmosphere. Furthermore, by recording the light produced, the telescopes can make a near calorimetric measurement of the energy [Man05]. As only a small fraction of the shower energy is transferred to fluorescence light emission, this method is efficient only above an energy of 10^{17} eV. The measurement period is constricted to moonless nights, limiting the duty cycle to $\sim 12\%$.

2.1.3 Hybrid Detector

One of the great benefits of applying two detection techniques, that are individually capable of detecting air showers and determining their parameters, is the chance of calibration cross-checks. These are performed on hybrid data, i.e. shower data, that has been recorded coincidentally by both detectors, as illustrated in figure 2.3. For example, energy measurement by the surface detector is very complicated, as suffering from shower-to-shower fluctuations. The hybrid detector design allows the SD energy calibration to be supported by FD energy measurements.

Furthermore, provided that the time synchronization between FD and SD is sufficient, hybrid reconstruction is an important issue. Air showers, which cannot be reconstructed by one of the detectors individually, may fulfill reconstruction requirements when making use of both FD and SD information. As an example, one might consider the case of one lonely tank trigger coinciding with FD signals. In this so-called 'single-tank hybrid mode' the lonely tank itself is obviously useless, but especially its timing can be valuable and relevant to support the FD shower reconstruction. In order to verify and calibrate this procedure, a Central Laser Facility (CLF) has been installed in about the middle of the array next to a surface tank. The vertically directed laser shots are visible for all telescopes; simultaneously, the nearby tank is triggered by a small portion of the same laser pulse using a light fiber. The resolution of the estimated shower core position with the FD

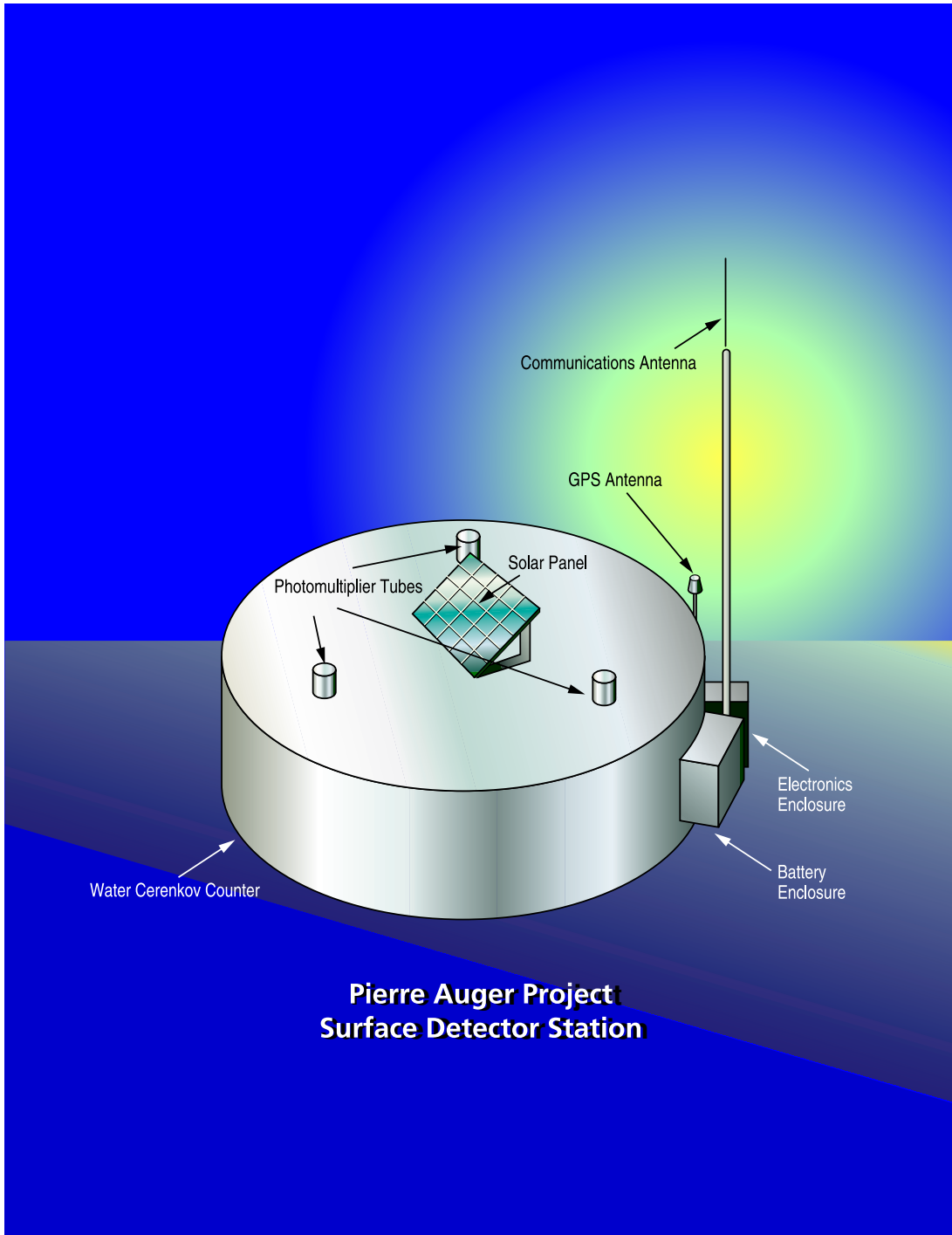


Figure 2.2: Schematic view of a surface detector tank [PDR97].

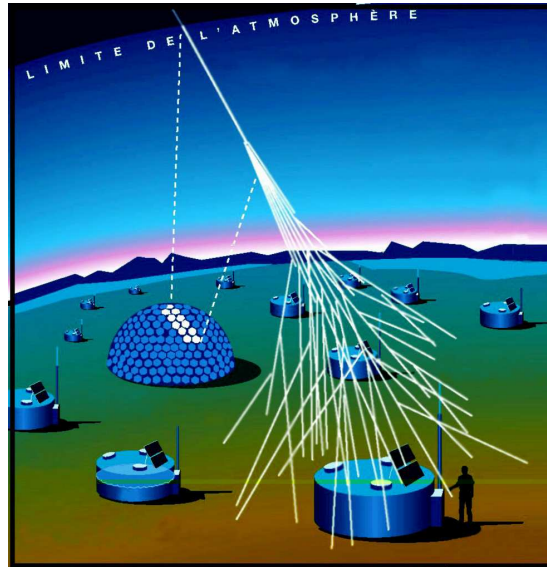


Figure 2.3: The principle of hybrid air shower detection [Fer07]. The track of fluorescence light is indicated on the Fly's Eye - like telescope; particles of the same shower hit the detector tanks on ground level.

improves by a factor of ~ 25 , e.g. from 550 m in 'mono-mode' to 20 m after including the timing information of the single water tank. The angular resolution of this technique is $\sim 0.6^\circ$ [Bon05][Mos05].

2.1.4 Radio Detector

Particles in an air shower are subject to two mechanisms of radio emission. Firstly, they travel faster than the speed of light in air, thus emitting Cherenkov radiation. As the physical size of an air shower is smaller than typical radio wavelengths ($\lesssim 10$ km for radio frequencies of $\gtrsim 10$ kHz), the emission of Cherenkov light is coherent [Hor06]. The negative charge excess developed by the shower results in the fact, that the radio signals do not cancel out each other, but are somewhat proportional to this charge excess [Ask65]. This allows an air shower to emit Cherenkov radiation at radio wavelengths in its forward direction.

Secondly, the charged shower particles are accelerated by the Earth's magnetic field. Two equivalent points of view are convenient to explain this phenomenon: On the one hand it can be understood as spatial separation of the negatively (electrons) and positively (positrons) charged part of the shower, which in turn would lead to transverse currents; thus, the air shower would emit dipole radiation [Kah66]. On the other hand Falcke and Gorham interpreted this phenomenon as synchrotron radiation of charged particles, travelling on their gyration circles in the geomagnetic field [Fal03].

Radio emission was found in the 1960s, when detection technology and equipment was limited and did not allow to do air shower analysis by means of radio signals; the most discouraging drawback was given by the continuous growth of background within the radio frequency range, being produced by commercial TV and radio stations. Recent studies, however, have been able to evidence, that today's measurement tools are basically capable of filtering such background; this yields the possibility of detecting air showers

by recording their radio signals.

The PAO aims at including the radio detection technique into the hybrid detector concept. Work on this new complementary detector component is ongoing and first results are expected to be published in the current year 2007.

2.2 SD Triggers and Data Acquisition

The trigger system of the surface detector has been designed to operate at a wide range of primary energies from 10^{17} eV to 10^{21} eV, yielding full efficiency above $10^{18.3}$ eV. It aims at selecting events of interest, while rejecting background and uninteresting events. The SD trigger system is hierarchical with two local trigger levels (T1, T2), a coincidence level (T3) formed at the observatory and two offline levels selecting physical (T4, physics trigger) and accurate (T5, quality trigger) events, respectively [LY05]. This trigger chain allows to decrease the local stations' hit rates from 3 ms^{-1} mainly due to background muons to 3 d^{-1} due to real showers.

2.2.1 Local Triggers

The T1 level contains two different trigger modes. Firstly, a Time over Threshold (ToT) trigger is implemented, requiring a two PMT coincidence of in each case 13 bins within a 120 bins window being above a threshold of $0.2 \cdot I_{VEM}^{est}$ (with I_{VEM}^{est} the reference unit for local calibration, see 2.1.1). The measured ToT rate of 1.6 Hz matches the expectation for the rate of double muons in an Auger tank. The technique of checking a bin window instead of a single bin is extremely efficient for detecting both high energy distant EAS and low energy showers; these showers typically provide rather small but spread signals. Furthermore, the background of single muons is ignored by application of this procedure. In parallel, the second trigger within the T1 level requires a three PMT coincidence of a simple $1.75 \cdot I_{VEM}^{est}$ threshold. At a rate of 100 Hz it is more noisy; nevertheless it is essential in order to detect the muonic component of air showers which generates fast signals ($< 200 \text{ ns}$, corresponding to < 8 bins).

A ToT at T1 level is directly promoted T2, whereas only 20% of the T1 single bin threshold triggers fulfill the T2 requirement of a three-fold coincidence at a higher threshold of $3.2 \cdot I_{VEM}^{est}$. Thus, the T2 rate is reduced to about 20 Hz. Only triggers passing the T2 level are used to define the T3. Besides, monitoring the T2 rate for each station individually, provides both a valuable tool to monitor the SD array performance and a means to calculate the array exposure [Par05].

2.2.2 Event Triggers

The T3 trigger level is based on the implementation of two different criteria. Firstly, the coincidence of three adjacent tanks, meeting the ToT requirement, defines the so-called 3ToT. It selects 90% physical events, as being based on the local low-background ToT. The other trigger within the T3, being applied in parallel again, is more permissive: Indeed, four tanks must pass the T2 level coincidentally, but they are allowed to be spread

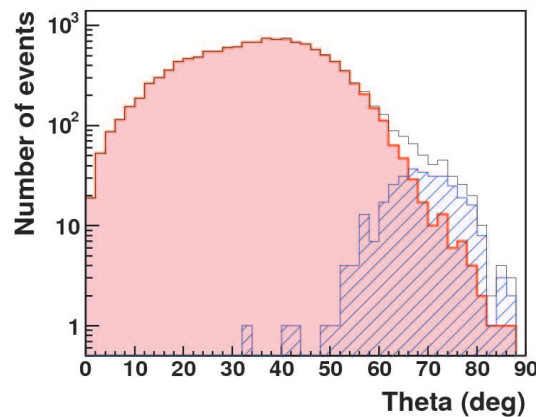


Figure 2.4: Zenith angle distribution for events satisfying the T4 condition applied (see text for details). Red shaded area corresponds to 3ToT events, while blue dashed area shows 4C1 events. Events that passed both conditions are counted in the 3ToT distribution [LY05].

up to 6 km distant, as long as they coincide within a reasonable time window. Only 2% of the events selected by this T3 are real showers; nevertheless it is needed to allow for the detection of strongly inclined up to horizontal showers, that produce both fast signals and spread footprints.

All data obtained from events that meet the T3 requirements are stored; a physical trigger (T4) performs real shower selection on this T3 data offline. Again one of two different requirements has to be met; applying the zenith angle cut improves the selection efficiency for the 3ToT criterion on T3 level from 90% to 99%, which hence simply proceeds to T4 level. Alternatively, the so-called 4C1 trigger condition has to be fulfilled; among the tanks triggered, at least one station must be surrounded by three firing tanks out of its six closest neighbors. In any case, reasonable timing conditions have to be observed, assuming the speed of light as the particle velocity and thus, allowing a tolerance window of 200 ns; due to chance coincidences, some accidental tanks have to be removed in most selected events. The two trigger methods work somewhat complementarily, as the few showers lost by the 3ToT are likely to be recorded by the 4C1, see figure 2.4.

2.2.3 Quality Trigger

The final trigger step T5 performs quality cuts on the T4 data. Each event has to be reconstructable with respect to energy and angular accuracy; in most cases, lack of reconstructability is caused by an inaccurate estimation of the shower core position. If an event comes down close to the border of the array, its core position will probably be estimated incorrectly, as parts of the shower are missing. To account for this problem, the T5 requires, that the tank with highest signal must have at least five coincidently working tanks among its six closest neighbors, and besides, the reconstructed core has to be located in an equilateral triangle of working stations. Besides the T5 trigger condition, a final cut is commonly applied offline selecting only events at zenith angles below 60° ; this provides compactness of the triggered tanks and supports stations whose FADC traces fulfill the more reliable ToT condition.

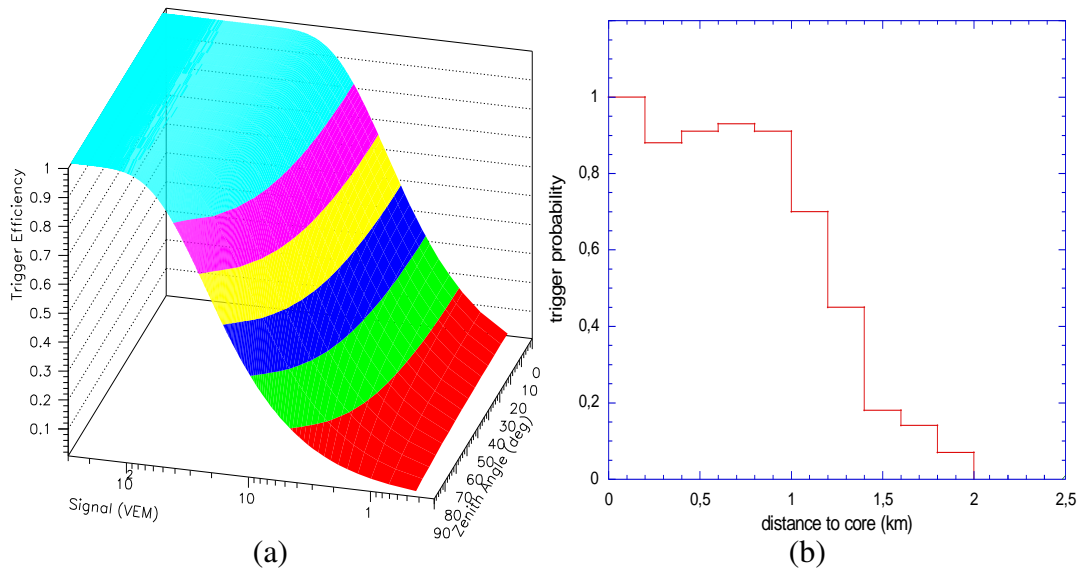


Figure 2.5: (a) Local tank trigger efficiency depending on signal size and zenith angle [Bau03].
 (b) Lateral trigger probability for core distances up to 2.5 km [Lhe03].

2.2.4 Tank Trigger Efficiency

The efficiency of the PAO SD trigger system depends on various parameters. In figure 2.5(a) the tank trigger efficiency as a function of energy and zenith angle is displayed. Due to shower to shower fluctuations, it is difficult to estimate the energy of a primary cosmic particle only by means of the energy deposit in the SD tanks, i.e. the tank signal. Thus, the energy axis in the efficiency plot is indicated by the individual tank's signal size in units of VEM. The conversion from signal size in VEM to shower energy in eV, which is basically linear, will be described in the next section 2.3.1. However, the plot clearly displays, that the efficiency decreases for increasing zenith angles and decreasing signal size.

Furthermore, the dependence of the tank trigger probability on the respective tank's distance to the shower core, i.e. the so-called lateral trigger probability (LTP), has to be accounted for. Figure 2.5(b) displays this dependency for a small set of data taken from the EA; only events with zenith angles below 45° and energies between 1 EeV and 2 EeV have been considered. Even though being quite preliminary, it shows, that the trigger probability decreases with increasing distance to the shower core, which corresponds to the expectation of less particles and smaller signal sizes at larger core distances: The strong relation to the LDF, section 1.2.2, is obvious.

2.3 SD Reconstruction

This section is dedicated to the reconstruction of shower parameters performed on SD data. Horizontal arrival direction, curvature of the shower front, lateral development and energy are the main quantities and attributes necessary in order to characterize a shower. Figure 2.6 displays three plots and a summary of data obtained from SD reconstruction: The upper left plot shows a plan of the SD array detecting an EAS with the diameters of

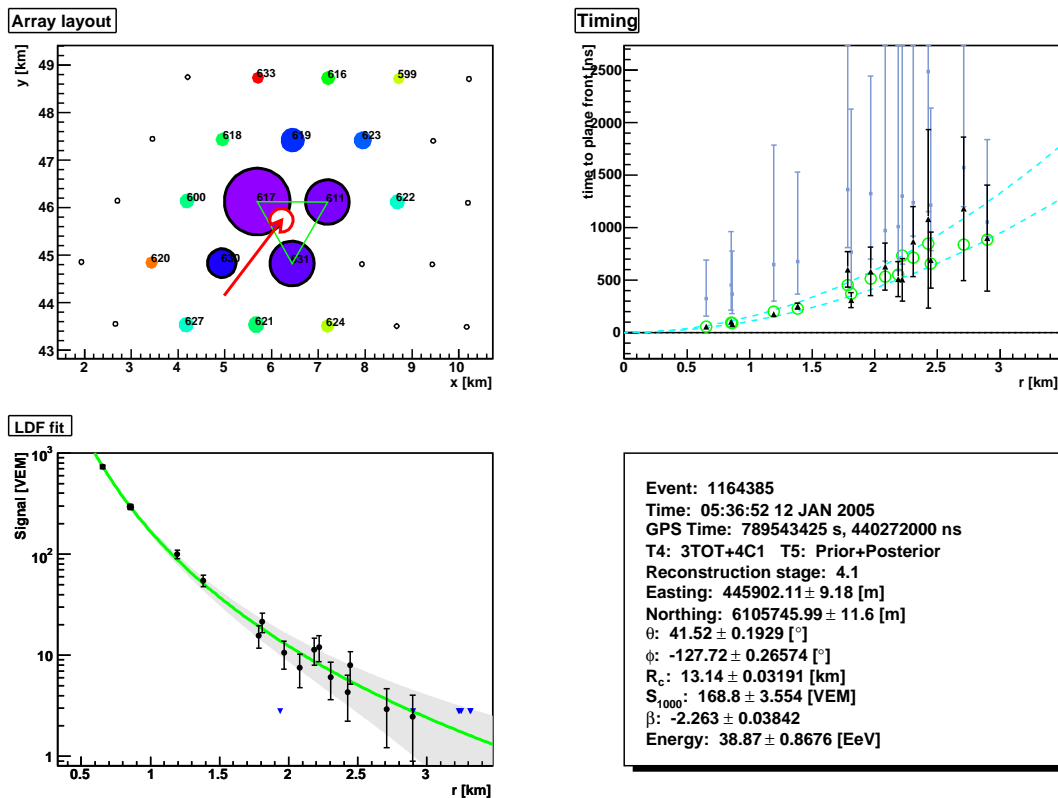


Figure 2.6: Example of an SD reconstructed shower obtained by the SD reconstruction module of the Offline Framework [Veb05]. Top left shows triggered tanks in the field, the circle diameter corresponds to the signal size in the tank; top right contains time information of tanks, time difference to plane shower front is plotted as function of core distance; bottom left plot shows signal size as function of core distance and LDF fit; bottom right window contains event information, reconstructed shower parameters and errors.

circles being related to the corresponding tank's signal size. The top right plot indicates the timing information of particles arriving in the tanks with respect to the expectation of a plane shower front; this issue is essentially correlated with angular reconstruction, which provides horizontal coordinates and curvature by means of timing information and will be discussed in its own chapter (3). The bottom left plot shows the lateral particle density, corresponding to the energy deposit in units of VEM (signal size) in the tanks as a function of core distance. Energy estimation is described more detailed in the following subsection. However, the determination of X_{max} , i.e. the shower maximum considering the longitudinal development, will remain unconsidered here; though having a huge impact on primary cosmic particle composition studies, X_{max} does not have a remarkable influence on coverage computation.

2.3.1 Energy Estimation

The SD measurement of the energy of a primary particle which initiates an EAS is a two step process. On the one hand the signals of triggered surface detectors have to be mea-

sured; on the other hand it is necessary to link these measurements with the initiating primary particle, allowing for each station's individual core distance. It has been shown, that uncertainties due to intrinsic shower to shower fluctuations can be minimized, if a characteristic signal is measured at a shower core distance of $\gtrsim 600$ m [Hil71]; this characteristic signal has to be identified at optimum precision, as it is chosen to be the SD energy estimator. Thus, it is of great importance to know the shower's lateral development, which can be modeled and fitted by an NKG-like LDF (compare equation 1.2)

$$S(r) = k \left(\frac{r}{r_0} \right)^{-\beta} \left(1 + \frac{r}{r_0} \right)^{-\beta}, \quad (2.1)$$

with β the slope parameter and k the shower size parameter [New05]. Ideally, the LDF would be known exactly and the shower size measurement would not depend on core distance, X_{max} , shower muon ratio and zenith angle asymmetries, but be due to only Poissonian signal fluctuations. In a more realistic view the accuracy of the LDF parameters is limited by experimental uncertainties. Therefore, it becomes necessary to define an optimum core distance r_{opt} , that depends solely on the array geometry; at this distance the variation in the predicted signal is supposed to be almost nullified by the correlations to both the slope parameter and the shower size parameter. In case of the PAO SD the signal variation is minimized at an optimum core distance of around 1000 m; the energy estimator therefore is named $S(1000)$. Investigations of alternative core distances or more sophisticated energy estimators are ongoing continuously, e.g. the predicted $S(1000)$ is taken at a zenith angle of 38° , accounting for zenithal dependences and thus improving the reliability of the energy estimator, i.e. $S(38)$ in this case.

The second step now is to find the link from $S(1000)$ to the energy of the cosmic ray primary. This can be done by either Monte Carlo (MC) simulations [Bil02] or FD cross-calibration using hybrid data [All06], as being shown in figure 2.7. Conversion formulae for the latter method are

$$S(38) = S(1000) \cdot \exp \left(\frac{X_0}{\lambda} \cdot \left[\frac{1}{\cos(\theta)} - \frac{1}{\cos(\theta_0)} \right] \right), \quad (2.2)$$

$$\frac{E}{10 \text{ EeV}} = \left(\frac{S(38)}{S_{38^\circ}^{10 \text{ EeV}}} \right)^{\frac{1}{\alpha}}, \quad (2.3)$$

where $S_{38^\circ}^{10 \text{ EeV}}$ is the absolute value of $S(1000)$ at 10 EeV and at 38° zenith angle determining the absolute energy scale, λ is the attenuation length of $S(1000)$ containing the zenith angle dependence, $X_0 = 875 \text{ g/cm}^2$ is the atmospheric depth of the PAO SD and α is the power index of the relation between $S(38)$ and energy.

The estimation of energy then necessitates the measurement of three parameters, i.e. $S_{38^\circ}^{10 \text{ EeV}}$, λ and α . While λ can be estimated relying on SD data only based on the Constant Intensity Cut (CIC) method, the determination of $S_{38^\circ}^{10 \text{ EeV}}$ and α has to rely on hybrid data. The CIC method assumes an isotropic arrival distribution of cosmic rays, so that above a given energy the integral flux is independent of zenith angle. Thus, selection of $S(1000)$ threshold values that lead to equal integral intensities at different zenith angles yields the determination of the zenith angle dependence of $S(1000)$ corresponding to a given energy threshold. This dependence of $S(1000)$ can be fitted to a straight line, commonly

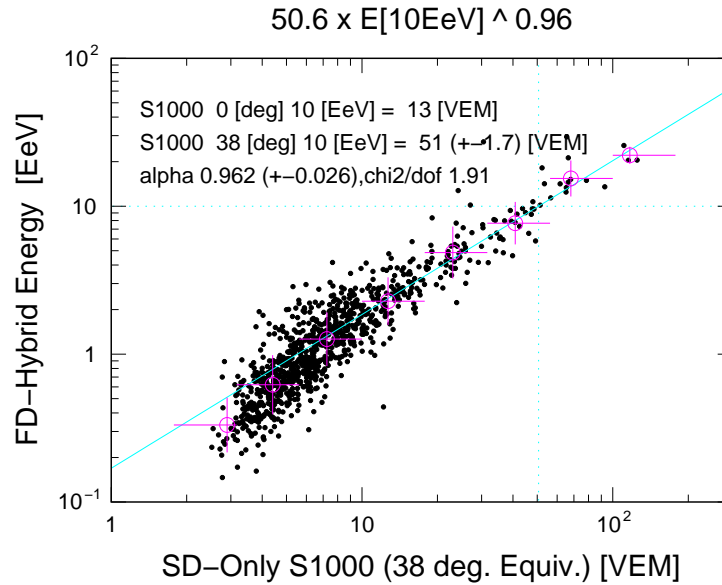


Figure 2.7: SD energy calibration by means of hybrid data [All06]. FD-hybrid energy is displayed as a function of $S(38)$, i.e. $S(1000)$ converted to be equivalent to a zenith angle of $\theta = 38^\circ$. The open circles and error bars indicate the profile of the distribution, while the solid line shows the result of fitting a power law above an energy of 2 EeV.

expressed as

$$S(1000)(\theta_0) = S(1000)(\theta) / \exp\left(-\frac{X_0}{\lambda} \cdot \left[\frac{1}{\cos(\theta)} - \frac{1}{\cos(\theta_0)}\right]\right), \quad (2.4)$$

with the slope (attenuation length) λ being the scaling length for dependence on atmospheric depth (compare equation 2.2), resulting in a value of $\lambda = (959 \pm 60) \text{ g/cm}^2$.

The final step of energy calibration is performed by means of independently reconstructed showers of both FD and SD in such a way, that the calorimetric energy measurement in the fluorescence detector is exploited to calibrate the surface detector energy scale, as indicated in figure 2.7. The results of the linear fit applied are $S_{38^\circ}^{10 \text{ EeV}} = (50.6 \pm 1.7) \text{ VEM}$ and $\alpha = 0.962 \pm 0.026$, respectively. The data is well described, $\chi^2/dof = 1.91$.

Chapter 3

Angular Reconstruction for the Surface Detector

The direction of an air shower is estimated by means of the arrival times of the shower front in the different SD stations. In addition to this timing information the coordinates x_i and y_i of each tank i are needed for angular reconstruction. GPS positioning and the local electronics' sampling frequency of 40 MHz yield a precision of ~ 8 ns in total [Abr04].

Several shower front models (plane, spheric, parabolic) can be used to predict the arrival times in the tanks. Assuming a plane shower front and a particle velocity close to the speed of light, the time difference between the measured arrival time t_i at tank i and the expected arrival time with respect to the tank's individual distance from the shower core can be written as [Pri03]

$$\Delta t_i = t_i - \left(T_0 - \frac{(x_i - x_{core})u + (y_i - y_{core})v}{c} \right), \quad (3.1)$$

where T_0 is the arrival time of the shower core at ground and $u = \sin \theta \cos \phi$ and $v = \sin \theta \sin \phi$ are the direction cosines; x_{core} and y_{core} are the coordinates of the core position, determined by the barycenter of all triggered tanks, weighted by the square root of each tank signal, with a typical accuracy of 150 m. To take into account shower front curvature, an additional term has to be added to equation 3.1, e.g. in case of a spheric shower front $r_i^2/(2Rc)$ (with R the curvature radius and r_i the core distance of station i). The common nomenclature of the horizontal angles is *zenith* = θ and *azimuth* = ϕ . These horizontal angles can be extracted from equation 3.1, by minimization of $\chi^2 = \sum_i (\Delta t_i)^2 / \sigma_{t_i}^2$, where σ_{t_i} is the uncertainty of the measured arrival time t_i .

3.1 Estimation of Arrival Times

The shower front arrival times are computed from the digitized signals of the first particles in the tanks. The precision of arrival time estimation from these raw FADC traces determines the accuracy of angular reconstruction.

A raw FADC trace of a single PMT is shown in figure 3.1(a). Determining the first signal bin is limited by several factors; atmospheric muons, low energy air showers and electric noise are 'seen' by the PMTs and transferred to their individual FADC trace. The

algorithm used to remove such noise and find the start time of the signal comprises the following steps [All06]:

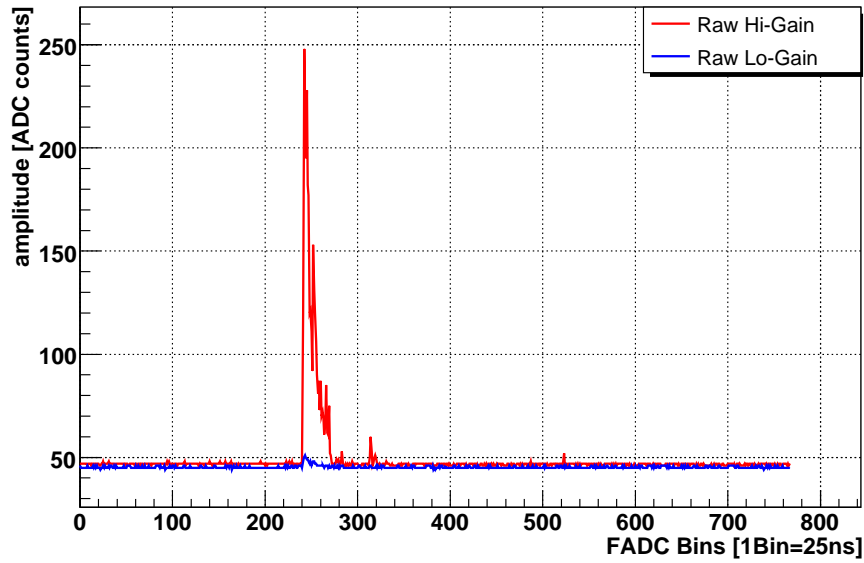
1. Estimate the initial value of the pedestal from the mean of the first 100 FADC bins. Simultaneously estimate the fluctuation of the pedestal from RMS; it will be set to 1 ADC count, if it is smaller than that.
2. Re-estimate the pedestal from the mean of the first 256 FADC bins. The buffer memory is usually read out in such a way, that the signal does start around the 256th bin. To make sure that small peaks preceding to the real signal are ignored in the pedestal computation, the absolute value of pedestal fluctuation in each bin has to be smaller than the RMS computed in step 1 to be included in the pedestal calculation.
3. Subtract the estimated pedestal from each bin of the raw FADC trace. Average binwise over all available PMT signals in one tank and consider the result as the tank signal (see figure 3.1(b)).
4. Search the bin with largest entry (MaxBin) by scanning the entire signal.
5. Search the bin with the first real signal (StartBin, i_{st}) by scanning from first bin to MaxBin and identify a candidate if its entry exceeds 5σ , with

$$\sigma = \sqrt{\frac{\sum RMS^2}{NumberOfPMTs}}. \quad (3.2)$$

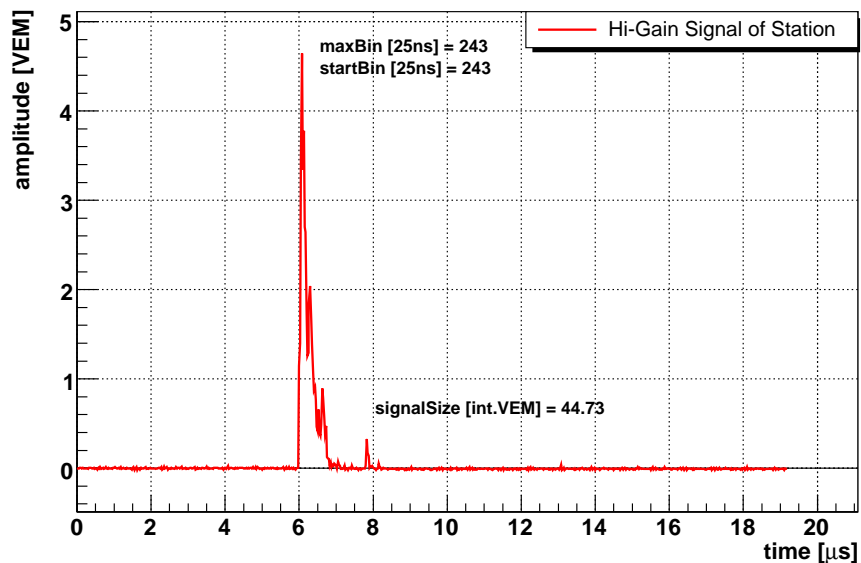
6. Integrate from $i_{st} + 1$ through $i_{st} + 2$; if the integral is larger than $4 \cdot \sqrt{2} \cdot \sigma$ try to pass the next step, otherwise go back.
7. Integrate from $i_{st} + 3$ through $i_{st} + 5$; if the integral is larger than $3 \cdot \sqrt{3} \cdot \sigma$ try to pass the next step, otherwise go back.
8. Integrate from $i_{st} + 6$ through $i_{st} + 12$; if the integral is larger than $7 \cdot \sqrt{7} \cdot \sigma$ try to pass the next step; or, if this value exceeds $\sqrt{7} \cdot \sigma$ try to pass the next step as well; otherwise go back.
9. Integrate from $i_{st} + 13$ through $i_{st} + 27$; if the integral is larger than $7 \cdot \sqrt{15} \cdot \sigma$ i_{st} will be the StartBin, otherwise go back.
10. If no bin fulfills above conditions, MaxBin will be assigned as the StartBin.

This procedure on the one hand aims at identifying small signals that precede large signals (steps 5-7), and on the other hand intends to reject local muons that coincide accidentally with the shower signal (steps 8,9).

Time synchronization within a tank can be verified by analyzing FADC traces of single muons; the shifts in signal peak time between the three PMTs have been found to be less than 10 ns. Relative time synchronization of local stations within the array can be obtained from reconstructed showers; the time offsets of the individual tanks can be estimated from the difference between the measured arrival time and the arrival time obtained by an angular reconstruction fit including all relevant stations but the one considered [Pri03].



(a)



(b)

Figure 3.1: (a) Raw FADC trace on single PMT level; the raw traces are given both for the dynode (Hi-Gain, red) and the anode (Lo-Gain, blue). (b) FADC trace on station level for the dynode signal (same event as (a), after individual pedestal subtraction), averaged over all available PMTs; estimated StartBin (see text) is 243 and integrated signal size is 44.73 VEM; typically 50 ADC counts correspond to 1 VEM (y-axis), depending on the individual calibration of the local station. The integrated signal recorded by a PMT is estimated by adding up all positive bin entries in its FADC trace from 20 bins before to 150 bins after the StartBin. The integrated station signal again is computed by averaging over the signals of all PMTs available.

3.2 Angular Resolution

The angular resolution (AR) is defined as the angular radius, that contains 68% of the showers coming from a point source; with Ω being the solid angle, the mathematical term then is

$$AR = 1.5\sqrt{\sigma^2(\Omega)} \quad (3.3)$$

To obtain the variance of the solid angle, the variances of zenith angle and azimuth angle have to be determined. It is obvious, that $\sigma^2(\Omega) = \frac{1}{2}[\sigma^2(\theta) + \sin^2(\theta)\sigma^2(\phi)]$. The parameters T_0 , θ and ϕ of equation 3.1 are extracted by minimization of $\chi^2 = \sum_i(\Delta t_i)^2/\sigma_{t_i}^2$, where σ_{t_i} is the uncertainty of the measured arrival time t_i . This uncertainty strongly determines the precision of the angular fit method applied. It suffers from two main effects: the sampling effect due to the drop in particle density and the flattening of the rise of the signal, both increasing with increasing shower core distance and decreasing energy, respectively. Analyzing data of showers that triggered at least five tanks, σ_{t_i} was estimated to be 22 ns at the shower core increasing to 50 ns at a core distance of $r = 1000$ m; this effect was parameterized to $\sigma = (22 + 0.03 \cdot r/\text{m})\text{ns}$ and has been taken into account for the angular reconstruction fit.

The angular uncertainties are obtained indirectly via the covariance matrix of the fit, that in turn can be approximated linearly to the covariance matrix (σ_{uv}) for θ and ϕ :

$$\sigma(\theta) = \frac{\sqrt{\cos^2 \phi \sigma_{uu}^2 + \sin^2 \phi \sigma_{vv}^2 + 2 \cos \phi \sin \phi \sigma_{uv}}}{\cos \theta} \quad (3.4)$$

$$\sigma(\phi) = \frac{\sqrt{\cos^2 \phi \sigma_{vv}^2 + \sin^2 \phi \sigma_{uu}^2 - 2 \cos \phi \sin \phi \sigma_{uv}}}{\sin \theta} \quad (3.5)$$

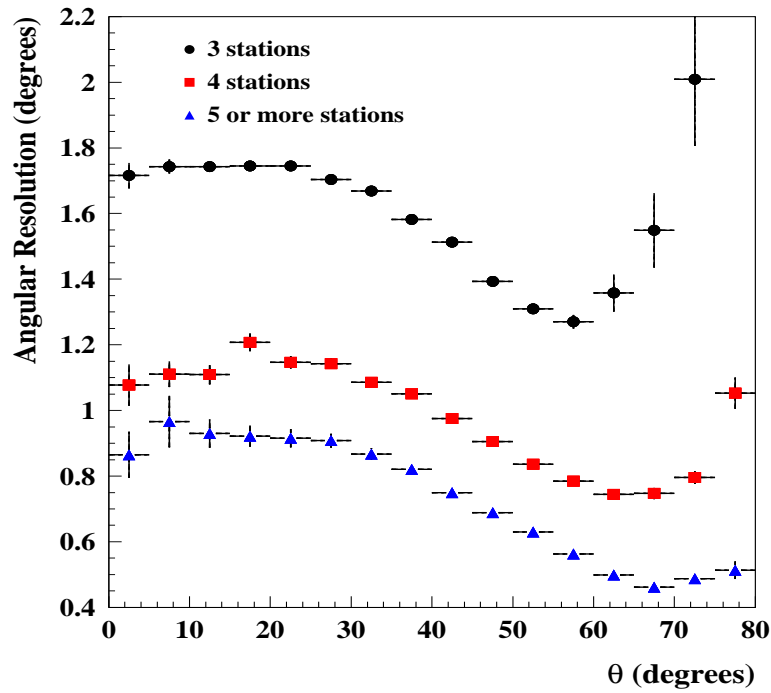
Relying on these terms, the angular resolution can now be calculated for each shower depending on the estimated horizontal angles. Figure 3.2(a) indicates the angular resolution depending on zenith angle for different tank multiplicities, i.e. number of adjacent tanks triggered by the shower. Figure 3.2(b) shows the energy dependence of the angular resolution for reconstructed T5 events with the typical zenith angle cut ($\theta < 60^\circ$).

The available statistics up to 2004 of high multiplicity events, i.e. events with five or more tanks triggered, from the so-called engineering array yield the following values for the mean angular resolution in terms of the uncertainties of zenith angle and azimuth angle [Sil03]:

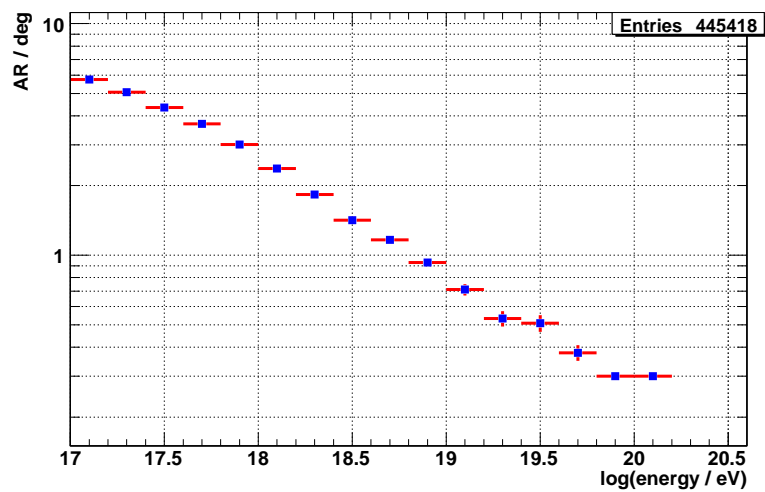
$$\sigma(\theta) = 0.8^\circ, \quad \sigma(\phi) = 1.1^\circ \quad (3.6)$$

3.2.1 Time Variance Model

The angular resolution estimated above shows only little dependence on core position uncertainty and the shower front model applied. The strongest influence on the size of AR is generated by the tank timing resolution. An attempt to reproduce the time measurement uncertainty is the Time Variance Model (TVM) [Bon05][Bon06b]. The TVM models the first particle arrival times in the detector tanks as a Poisson process. The Poissonian treatment yields the following variance, modelling the first particle arrival time T_s out of



(a)



(b)

Figure 3.2: (a) SD angular resolution as a function of zenith angle θ for various tank multiplicities [Bon05]: circles 3 stations (approx. $E < 4$ EeV), squares 4 stations (approx. $3 < E < 10$ EeV) and triangles more than 4 stations (approx. $E > 8$ EeV). (b) Angular resolution as a function of energy up to $10^{20.5}$ eV in a double logarithmic plot; data set contains reconstructed T5 events from 01.2004 until 01.2007 with the typical zenith angle cut ($\theta < 60^\circ$). At 3 EeV $\approx 10^{18.5}$ eV AR drops below 1° for most events.

a set of n particles arriving in a time interval:

$$\sigma^2(T_s) = \frac{n(\Delta T)^2}{(n+1)^2(n+2)} + b^2 \simeq \left(a \frac{T_{50}}{S_{VEM}} \right)^2 + b^2, \quad (3.7)$$

where S_{VEM} is the station signal, T_{50} is the time interval that contains the first 50% of the total signal; n is the number of particles, that can be calculated from the total tank signal and the particles' average track length within the tank, the latter being parameterized by a Monte Carlo. The scaling parameter a is used to allow for approximations made, while b^2 is needed to take into account the known timing uncertainties due to GPS resolution (~ 10 ns) and FADC sampling frequency $\sim 25/\sqrt{12}$ ns.

The expectation for the parameters is $a \approx 1$ and $b = \sqrt{10^2 + (25/\sqrt{12})^2} \approx 12$. In order to adjust them by means of real data, T4 events from twins of the period April 2004 to December 2005 have been used. Defining the time difference $\Delta t = dT_{s,1} - dT_{s,2}$, with $dT_{s,i}$ the time difference from the first particle arrival time measured in tank i of the twins and the expected arrival time with respect to the fitted shower front. With $N = 1390$ events surviving the cuts, the parameters were adjusted by maximizing the Likelihood function

$$L = \prod_{k=1}^N \frac{1}{\sqrt{2\pi\sigma^2[\Delta T_k]}} e^{-\frac{\Delta T_k^2}{2\sigma^2[\Delta T_k]}}, \quad (3.8)$$

where $\sigma^2[\Delta T_k]$ is the sum of the T_s for each twin member and event k using equation 3.7. The results obtained are

$$a^2 = 1.00 \pm 0.06, \quad (3.9)$$

$$b^2 = (147 \pm 23)\text{ns}^2, \quad (3.10)$$

which is consistent with the expectations. So, the TVM seems to provide a pretty good description of the data of arrival time uncertainties.

3.3 Conclusions

In this chapter, angular reconstruction of air showers detected by the PAO SD has been described. The mechanism is based on the first particle arrival times in the tanks triggered by the shower. The uncertainty of this timing information yields the dominant effect with respect to the reconstruction precision, i.e. the angular resolution. The so-called Time Variance Model accounts for the timing uncertainty and describes the data nicely.

Dependencies of the angular resolution on both the energy (figure 3.2(b)) and the zenith angle (figure 3.2(a)) have been shown. Angular resolution improves with increasing energy; considering the zenith angle dependence above full trigger efficiency, $energy > 3$ EeV, the resolution minima, i.e. points of best precision, are located around $\theta = 60^\circ$. For air showers surviving the typically applied zenith angle cut ($\theta < 60^\circ$), the angular resolution of the PAO SD at full efficiency is better than $AR < 1.8^\circ$.

Chapter 4

Celestial Positioning

The frame of reference for the geographically local measurement of arrival directions of cosmic rays and extensive air showers, respectively, is time dependent. Because of the Earth's rotation, a pair of locally measured angles of an incoming shower determines a point on the celestial sphere, that seems to travel. It takes the period of a sidereal day, i.e. 23 h, 56 min and 4.099 s, or simply 360° , until the point will be visible again in the same direction and from the same geographic position. This time is different from the mean solar day (24 h), as the Earth's travel around the sun yields an additional rotation interval of $\sim 1^\circ$ per day. Thus, the number of sidereal days within a year (366.25636042) exceeds the number of mean solar days in the same period (365.25636042). The Earth's axis can be assumed as fixed within a period of 50 years, as only little precession of $1^\circ/180$ y is observed. Thus, epochs are defined referring to the standard equinox (see below for explanation) every 50 years, with the actual period being named J2000.0. Furthermore, considering galactic and intergalactic distances, the Earth's relative position to the sun is negligible, too.

In order to specify a celestial position from the point of view of the PAO, several different coordinates are needed. Obviously, the *horizontal* position of the apparent source of the cosmic ray on the celestial sphere has to be known. Furthermore, this positioning information depends on both the *geographic* position of the observer, i.e. the PAO, and the *time* of the observation. Two fixed reference frames are conventionally used, in order to specify a point on the celestial sphere: Both the *equatorial* and the *galactic* coordinate system are independent of time, observer position and locally measured arrival direction of a shower¹. In this thesis, the equatorial coordinate system was chosen for the display of directional information. The transformations between the various frames of reference are quoted in the following sections [Mee91]. They are used within this thesis in order to transform the directional information obtained by the PAO SD into galactic coordinates. The algorithms applied have been taken from the LIBNOVA library [lib06].

¹The equatorial reference frame is defined by means of the vernal equinox and thus, the respective epoch of the time of measurement has to be specified. This is not valid for galactic coordinates which in fact are fixed on the sky.

4.1 Reference Frames

4.1.1 Geographic Coordinates

A geographic position is specified by a pair of spherical coordinates, i.e. geographic longitude lon , with $lon = 0^\circ$ at the Greenwich prime meridian, and geographic latitude lat , with $lat = 0^\circ$ at the equator. The center of the PAO SD array expressed in geographic coordinates then is located at

$$lon_{PAO} = 69.25^\circ\text{W} \quad , \quad lat_{PAO} = 35.25^\circ\text{S}. \quad (4.1)$$

The maximum array dimension in terms of geographic latitude is $\Delta lat_{PAO} = 0.56^\circ$, which can be accounted for by using the reconstructed shower core position instead; however, the SD angular resolution at full efficiency is of the order of $\sim 1^\circ$ (see chapter 3.2) and thus, the error with respect to the core position, 0.28° , will be neglected in the following coverage computation and analysis. The Earth's equatorial plane is inclined $\sim 23.4^\circ$ with respect to the solar plane, i.e. the plane, in which the Earth travels by the sun. This inclination and the inclination of the solar plane with respect to the galactic plane both have to be taken into account, when transforming into galactic coordinates.

4.1.2 Horizontal Coordinates

The incoming directions of air showers are measured in spherical coordinates of zenith angle θ , with $\theta = 0^\circ$ in case of a vertical shower, and azimuth angle ϕ , starting with $\phi = 0^\circ$ in the north and counting clockwise. Horizontal coordinates, however, may also be given in altitude alt and azimuth angle, where the altitude is the elevation of an object above the horizon, $alt = 90^\circ - \theta$. The reference plane, called the horizontal plane, is a plane tangential to the Earth's surface through the observer position. The positions of celestial objects depend on the observer position and the time of observation. Thus, the horizontal reference frame is inappropriate to be a coordinate system for cataloging celestial positions.

4.1.3 Equatorial Coordinates

The position of a celestial object can be specified independently of time and observer position in an equatorial reference frame. Equatorial coordinates are spherical and the reference plane is given by the Earth's equatorial plane; orientation and position of this plane are fixed, neglecting the relative position of our planet to the sun. The precession of the Earth's axis slightly alters the orientation of the equatorial reference frame with respect to the position of fixed stars. Thus, when considering observations separated by long intervals of time, it is necessary to specify an epoch (J2000.0 currently, B1950.0 for older data), in order to specify coordinates of celestial objects. The declination δ corresponds to the spherical latitude, giving the angular distance of a star to the equatorial plane, while the spherical longitude is called right ascension α ; the reference point for α can be chosen arbitrarily, conventionally it is the vernal equinox, which is defined as the point on the equatorial plane, that coincides with the position of the sun at the beginning of spring.

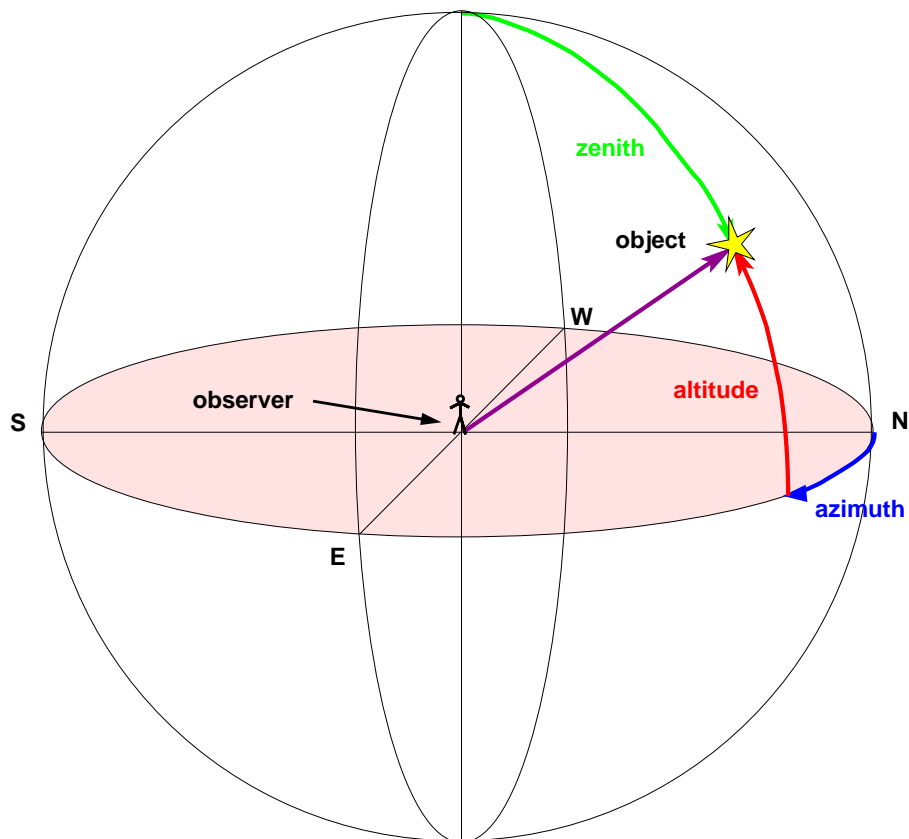


Figure 4.1: The horizontal coordinate system is a spherical coordinate system with the latitude being called altitude and the longitude known as azimuth angle. It covers a half space, as the azimuth angle can take only positive values. It is centered on the observer and the reference plane is defined by the observer's horizon. If in addition to the pair of horizontal coordinates time and observer position are known, the celestial position of an object can be determined.

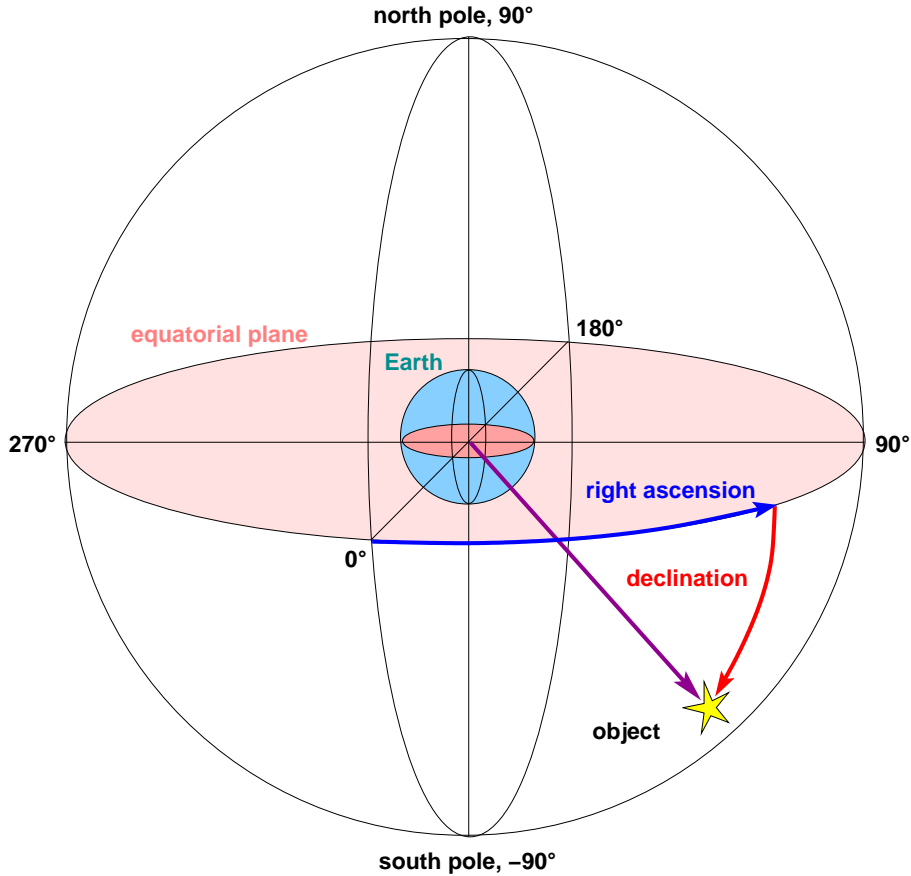


Figure 4.2: The equatorial reference frame is a spheric coordinate system in declination (latitude) and right ascension (longitude). It is centered on the Earth and the reference plane is given by the equatorial plane of our planet; correspondingly, the Earth and the equatorial system share the directions of the poles as well. Celestial directions can be specified independently on time (neglecting epochal conventions, see text), without providing information about distances.

In order to find a visible object in an appropriate catalog, its celestial coordinates have to be specified: δ is well defined, as the equatorial plane is fixed and so is the angular distance of the object,

$$\delta = \arcsin[\cos(\theta) \sin(lat) - \sin(\theta) \cos(lat) \cos(\phi)]. \quad (4.2)$$

In order to find α , it is necessary to introduce the local time information. The hour angle h is defined as the difference in geographic longitude between the positions of observer and the point on the Earth's surface, where the object appears at zenith angle ($\theta = 0$); α then is simply given by the difference between local sidereal time LST and hour angle h , which can be converted from time to angular units ($360^\circ = 2\pi \approx 23.9344719$ h)

$$LST - \alpha = h = \arcsin \left[\frac{\sin(\theta) \sin(\phi)}{\cos(\delta)} \right]. \quad (4.3)$$

4.1.4 Galactic Coordinates

The sun has been chosen to be the origin of the galactic reference frame; its distance to the galactic plane, i.e. the plane of the milky way, is negligible (a few lightyears). The galactic longitude l is $l = 0$ at the galactic center, which is located at $\alpha = 17$ h, 45.7 min and $\delta = -29^\circ$; l is counted counterclockwise. The angular distance of an object from the galactic plane is specified by the galactic latitude b ; it is positive for northern directions, while north is defined by the thumb in a right-hand principle of counting l . The inclination i of the galactic plane with respect to the equatorial plane amounts to $i = 62.6^\circ$. As the intersection of galactic and celestial (i.e. equatorial) equator is given by $l_0 = 33^\circ$ in the galactic or $\alpha_0 = 282.25^\circ$ in the equatorial reference frame, respectively, the transformation is a simple rotation, that in total accounts for both the inclination of the equatorial plane and of the plane of the Earth's orbit.

$$b = \arcsin[\sin(\delta) \cos(i) - \cos(\delta) \sin(i) \sin(\alpha - \alpha_0)], \quad (4.4)$$

$$l = l_0 + \arccos\left[\frac{\cos(\delta) \cos(\alpha - \alpha_0)}{\cos(b)}\right], \quad (4.5)$$

In order to account for time dependences of directions and positions due to the precession of the Earth's axis, the referenced values of l_0 and α_0 , respectively, have to be linked to the epoch of their validity: $l_0 = 33^\circ$ and $\alpha_0 = 282.25^\circ$ are valid in the so-called epoch J2000.0, as mentioned before. However, while planetary precession is the dominant gyroscope effect, further smaller influences such as nutation and aberration can be neglected seeing that the SD angular resolution is clearly larger, as shown in chapter 3.2; even under the assumption of a detector operating period of some ~ 10 y, none of the latter effects is expected to be visible for the PAO.

4.2 The HEALPix Pixelization

In order to operate on a set of continuously distributed data of arrival directions in celestial coordinates, it is necessary to discretize the solid angle digitizing the spherical surface. Therefore, the directional information has to be binned appropriately.

HEALPix is a Hierarchical, Equal Area, and iso-Latitude Pixelization of the sphere designed to support efficiently local operations on the pixel set, a hierarchical tree structure for multi-resolution applications, and the global Fast Spherical Harmonic transform [Gor05b]. Providing mathematical algorithms related to the distinctive nature of the spherical spatial domain, it is a useful tool to investigate astronomical data distributed on the entire sky, or a considerable fraction thereof. HEALPix has been widely explored in CMB research groups in order to cope with huge data sets on the one hand, and can be exploited to obtain scientific results concerning anisotropy on the other hand.

It is advantageous to use equal areas of discrete elements of partition, as it allows to sample sky signals without regional dependence; thus, problems due to the latitude dependence of the solid angle in a spherical coordinate system for example can be avoided. The hierarchical structure of the data base is essential for very large data sets, as it provides that the elements which are nearby on the surface of a sphere, are also nearby within the tree structure of the data base; this method facilitates topological analyses, especially concerning the runtime. Finally, the iso-latitude of discrete elements on a sphere is essential

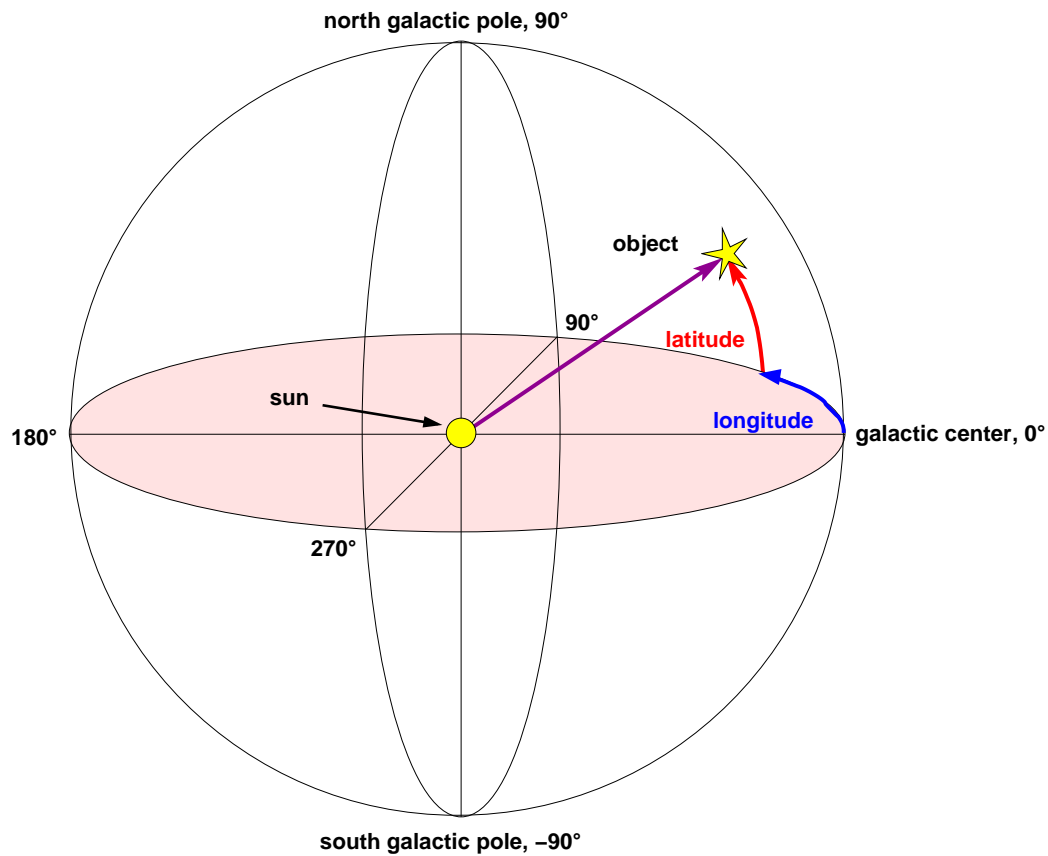


Figure 4.3: The galactic reference frame is a spherical coordinate system with galactic longitude and latitude. It is centered on the sun and the reference plane is given by the plane of our galaxy, i.e. the milky way. It is fully sufficient to independently specify both galactic and extragalactic directions, without providing information about distances.

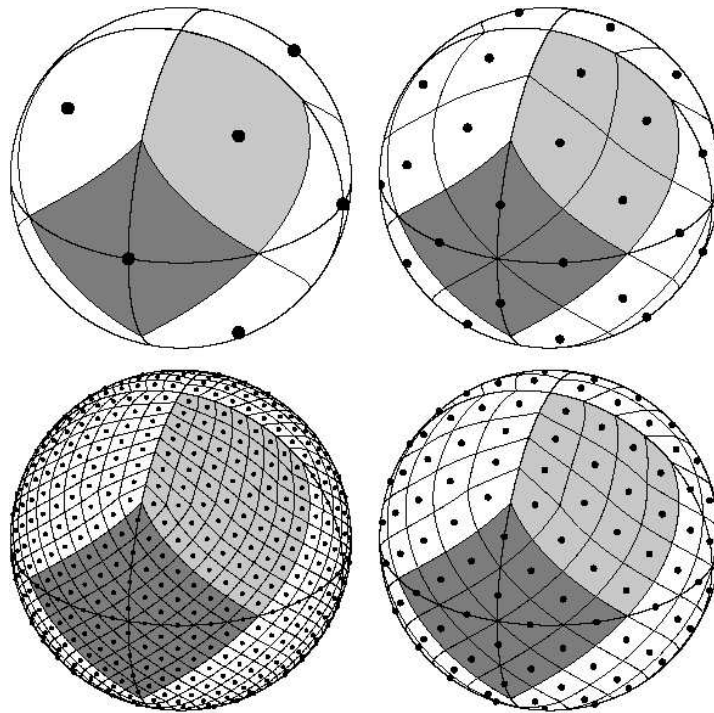


Figure 4.4: HEALPix pixelization for various resolutions, starting from $N_{pix} = 12$ pixels ($N_{side} = 1$, top left panel) and increasing clockwise to $N_{pix} = 48$, 192 and 768 pixels ($N_{side} = 2$, 4 and 8). Light-gray shading shows one of the eight (four north, and four south) identical polar base-resolution pixels. Dark-gray shading shows one of the four identical equatorial base-resolution pixels. Within each panel the areas of all pixels are identical [Gor05a], while the azimuthal distance within one ring of iso-latitude is constant.

again to improve computational performance; operations that involve slow recursions to evaluate associated Legendre polynomials will cause an increase in runtime, if the sampling grid deviates from an iso-latitude distribution [Gor05a]. Moreover, this aspect is heavily exploitable in the analysis of coverage maps in equatorial coordinates, which will be shown in chapter 6.

The resolution of a sphere pixelized by HEALPix is specified by the resolution parameter N_{side} ; it can have discrete values, that are a power of 2. The least resolution, given by $N_{side} = 1$, corresponds to a subdivision of the sphere into 12 pixels of equal area. A step towards better resolution subdivides each pixel into four new pixels; thus, the number of pixels is $N_{pix} = 12 \cdot N_{side}^2$, see figure 4.4. All pixel centers are located on $N_{ring} = 4 \cdot N_{side} - 1$ rings of constant latitude. Within each panel the areas of all pixels are identical. The CDAS HERALD data files generated and filled by the PAO reconstruction chain contain information about all reconstructable shower parameters, such as energy, directional information and the respective resolution. The directional analysis of the bulk of reconstructed showers at the PAO necessitates the creation of digitized sky maps. They are the intermediate stage in information processing between the entry point of data acquisition and the final stage of astrophysical anisotropy analysis.

Chapter 5

Sky Coverage

The visible part of the sky from the position of the PAO can be computed by transforming locally observable directions into celestial coordinates. During the period of one sidereal day, the view of the surface detector covers more than half of the full sky. This is valid even for the typical zenith angle cut $\theta < 60^\circ$, that is applied in order to account for the reconstructability of incoming showers. Stronger inclined and horizontal showers necessitate a different reconstruction chain consisting of different algorithms. They provide less statistics, due to the exponentially increasing attenuation of particles in the atmosphere, and thus are ignored in the following analysis.

The knowledge of the coverage map, i.e. the skymap of the expected number of events in each accessible celestial direction, is crucial for anisotropy studies. The main difficulty in estimating the coverage is given by the surface detector acceptance, that depends on various shower parameters, such as the zenith angle and the energy, especially at energies below full trigger efficiency ($\sim 3 \text{ EeV}$). The combination of the visible part of the sky and the SD acceptance, which shows dependence on the locally measured arrival directions, yield the coverage. Through evaluation of the expected number of showers from each direction assuming an isotropic distribution, these surface detector acceptance effects can be disentangled from real anisotropies.

Fully analytical attempts to compute the coverage fail so far, as no model describes the detector acceptance sufficiently. Thus, there are basically two applicable computation methods that have to rely on extrapolations of real shower data: shuffling and semi-analytical [San07]. This chapter deals with the presentation of both methods, while their characteristics are explored in more detail in the next chapter 6.

5.1 Data Set of Real Showers

The data set included in the coverage computation and analysis consists of all 445815 showers with zenith angle of less than 60° , seen by the PAO SD from the beginning of 2004 until the end of 2006, and fulfilling the T5 trigger condition. In case a different data set is analyzed or alternative cuts have been applied, respectively, this will be mentioned explicitly. The shower parameters are obtained by the CDAS reconstruction chain, stored in the so-called HERALD data files and made accessible for PAO data analysts. Arrival directions of all showers fulfilling the cut conditions can be filled into a pixelized sphere of equatorial coordinates, building the skymap of events shown in figure 5.1.

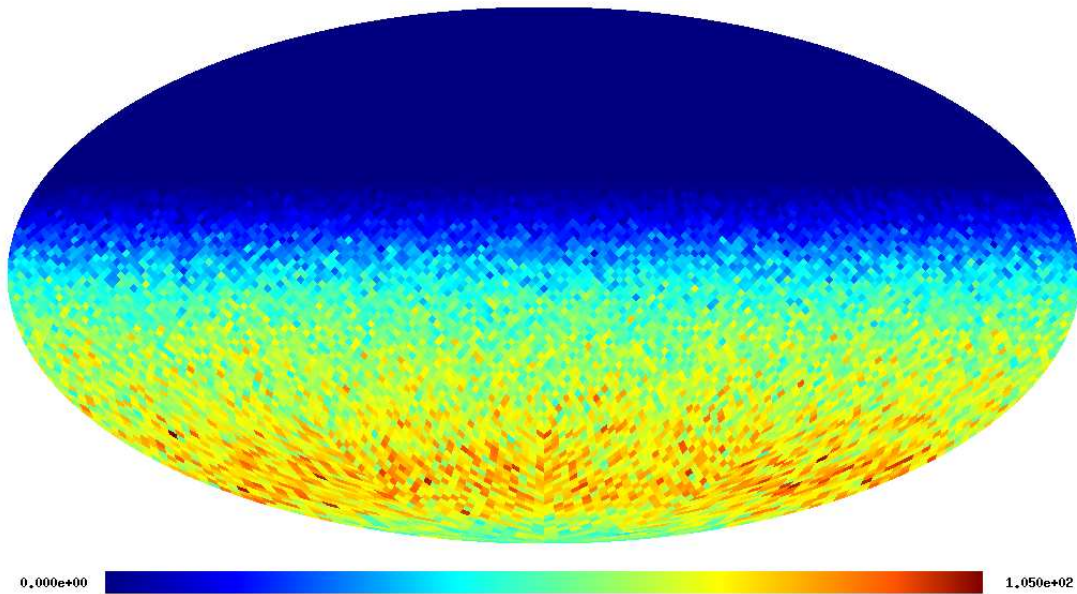


Figure 5.1: Skymap of reconstructed events in equatorial coordinates; the map resolution is $N_{pix} = 12288$ equal area pixels on the sphere, the area accurate projection preserves the parallelism of latitudes (Mollweide projection). Due to the relatively small number of entries, a rather coarse pixelization had to be chosen.

5.1.1 Skymap of Events

Figure 5.1 shows the so-called Mollweide projection of a sphere in equatorial coordinates. This projection preserves both the parallelism of latitudes and area accuracy. Equatorial declination is plotted vertically; it is centered on zero at the equator, while ranging from -90° in the south (bottom) to $+90^\circ$ in the north (top). Equatorial right ascension is counted horizontally, starting at zero in the center, being counted anti-clockwise (from left to right) between 0° and 360° . The color indicates the number of events falling in the 12288 pixels, ranging from 0 entries (dark blue) to 105 entries (dark red) out of a total number of 445815 events.

The geographic latitude of the observatory is $lat_{PAO} = -35.25^\circ$. Thus, a vertical line starting from the PAO intersects the equatorial sphere at a declination of $\delta_{PAO} = lat_{PAO} = -35.25^\circ$, so that the declination values limiting the view of the observatory simply can be obtained by adding or subtracting the zenith angle limit. After applying the typical zenith angle cut ($\theta < 60^\circ$), the declination limit of the visible part of the sky is $\delta = 24.75^\circ = \delta_{PAO} + 60^\circ$ in the north. The sky beyond (north of $\delta = 24.75^\circ$) is not taken into account in the skymap of events, and causes the unstructured dark blue region in the upper part of the plot. Instead of providing a similar cut-off in the south, subtracting the zenith angle limit from the PAO position, $\delta_{PAO} - 60^\circ = \delta = -95.25^\circ$, leads to the following insight: A circle of 5.25° angular radius centered on the south pole is always visible from the point of view of the PAO. If no zenith angle cut had been applied, the upper limit of the PAO's view in terms of declination would be at $\delta = 54.75^\circ$, while the angular radius of the always visible circle around the south pole would increase to 35.25° , obviously.

Only considering data taking periods of full years minimizes the amount of fake anisotropy being introduced into the coverage, as temperature effects are supposed to

be averaged out more or less; variations of the detector size, however, still are a problem, as they may systematically enlarge the expectation for directions, that correspond to times of a bigger detector.

5.1.2 Azimuth Angle Distribution

Furthermore, taking into account full years also prevents biasing the coverage map through the so-called east-west anisotropy, that is caused by the Earth's magnetic field and has an impact on the distribution of the locally measured azimuth angle of an incoming shower; via deflection, particles can be impeded from reaching the Earth's surface depending on particle charge, energy and incoming direction, i.e. azimuth angle. As a huge amount of the secondary particles finally triggering the SD array are electrons, showers arriving from the east are supposed to trigger more easily. In fact, out of 500000 showers at zenith angle $\theta < 60^\circ$, 251279 ± 501 came in from the east ($0^\circ < \phi < 180^\circ$), while 248721 ± 499 arrived from western ($180^\circ < \phi < 360^\circ$) directions, yielding a significance level of $\sim 5\sigma$. This effect is one of the observable features in the azimuth angle distribution, given in the top histogram of figure 5.2.

A second feature, caused by the SD array geometry, can be observed when applying certain cuts: Below an energy limit of $E \lesssim 0.5$ EeV and beyond a zenith angle limit of $\theta \gtrsim 50^\circ$ the detector acceptance shows azimuthal dependence due to the hexagonal grid structure of the SD array, shown in the bottom histogram of figure 5.2. In order to display the sixfold periodicity, a sine-like fit has been applied to the distribution ($p_0 + p_1 \cdot \sin[\frac{\phi \cdot \pi}{6 \cdot 180^\circ} + p_2]$), yielding $\chi^2/dof = 1.06$. This describes the data better than for example a flat fit does ($\chi^2/dof = 1.41$). The event rate after the given energy and zenith angle cuts is negligibly small (2306 compared to 500266, corresponding to a ratio of 0.5%). The actual event rate ratio will be even smaller, and the effect of the hexagonal grid structure will be weaker, if only events at zenith angles between 50° and 60° are considered. Hence, both features can be neglected for data taking periods of a multiple of full years and a generally flat azimuth angle distribution still fits the data quite well, which is also verified by the $\chi^2/dof \approx 1.06$ for a flat fit.

5.2 Shuffling

Shuffling (or scrambling, equivalently) methods produce fake events by shuffling the reconstructed parameters of real showers. The information necessary to determine a celestial position is the collection of arrival direction in horizontal coordinates, observer position in geographic coordinates, and time information. The observer position, i.e. the position of the PAO is given by $lon_{PAO} = 69.25^\circ$ W and $lat_{PAO} = 35.25^\circ$ S; the core position of the respective shower will be neglected, as the angular dimension of the SD array is $\sim \pm 0.25^\circ$, which is less than the angular resolution of the shower direction reconstruction, $\sim 1^\circ$ (chapter 3.2). Horizontal arrival directions are reconstructed individually to zenith angle θ and azimuth angle ϕ , while timing information is provided by the time of the shower core reaching ground level. The two shuffling methods, that will be presented in the following subsections, both operate with the time information being shuffled.

Basically, in the shuffling method the shower parameter distributions provided by the

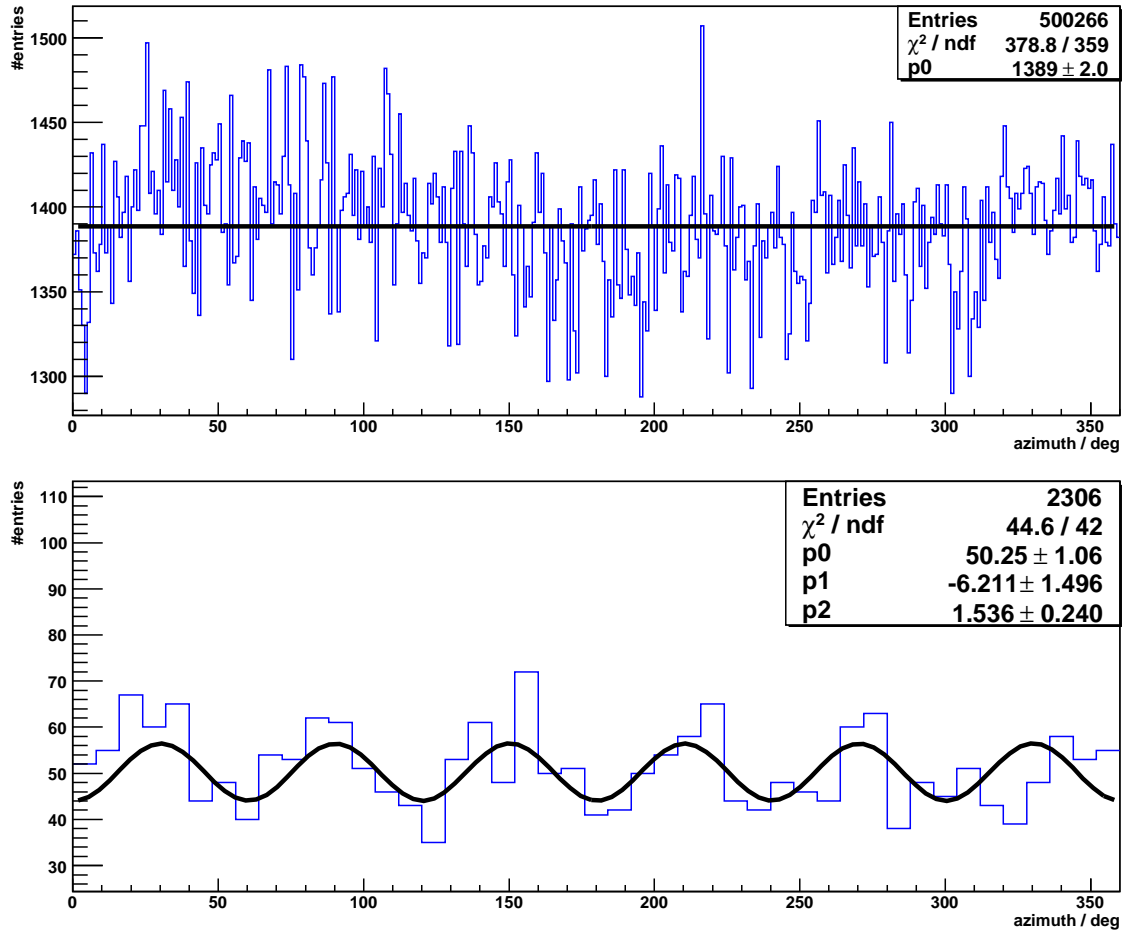


Figure 5.2: Azimuth angle distribution with and without cuts for events fulfilling the T5 condition from 01.2004 until 03.2007: The top histogram shows the azimuth angle distribution for no further cuts applied, except the typical zenith angle cut $\theta < 60^\circ$; taking into account the null suppression on the y-axis, it can be assumed reasonably as equally distributed corresponding to the satisfying result of a fit by a polynomial of zeroth order: $\chi^2/dof \approx 1.06$. Higher entries are observable for “eastern” bins at $0^\circ \leq \phi < 180^\circ$, see text for details. The following cuts were applied to obtain the bottom histogram from the same data set: $energy < 0.5 \text{ EeV}$, $\theta > 50^\circ$; the sixfold periodicity of the distribution due to the hexagonal array structure is clearly visible for these cuts. The simple sine-like fit with $p_0 + p_1 \cdot \sin[\frac{\phi \cdot \pi}{6 \cdot 180^\circ} + p_2]$ provides a good agreement with the expectation of periodicity, corresponding to $\chi^2/dof = 1.06$. A flat fit gives $\chi^2/dof = 1.41$, implicitly yielding support for the periodic fit

bulk of showers taken from the data set are preserved. This is not valid explicitly for the distribution of the azimuth angle, which will be assumed as and forced to be equally distributed, according to its attributes discussed above (section 5.1.2).

5.2.1 Shuffling JD

As the name implies, this method shuffles the full time information in Julian Day (JD) format. The JD originally is defined as an integer, that starts from zero at noon Universal Time (UT) Monday, January 1, 4713 BC in the proleptic Julian calendar; the information of the time of day can be appended simply as the decimal places of the JD understood as a decimal number, then. The Julian day can easily be derived from the UTC (Universal Time Coordinated) format given by the HERALD data files, that also provide the shower arrival direction in horizontal coordinates. This information is sufficient to specify a point in the sky, e.g. in equatorial coordinates, see chapter 4.1.

As mentioned above, the azimuth angle distribution is assumed to be flat, whereas the original zenith angle values are kept in a list. The JD is kept in a list as well, which is supposed to be shuffled after each run, i.e. after iterating through the whole list. The coverage map computation stepwise takes the following very simple actions, based on a set of N_e real events:

1. get one value from each of the lists of zenith angle θ and Julian day JD ; randomly select an azimuth angle ϕ
2. transform the collected information to equatorial coordinates
3. fill the corresponding pixel obtained by HEALPix
4. having iterated through all values in the full lists element-wise taking the actions 1. to 3., shuffle the list of Julian day and re-start at 1.

This procedure is repeated as often as necessary in order to create the desired number of data samples (i.e. N_s times).

5.2.2 Shuffling JD_{int} and JD_{rest}

This method is strongly based on a study by Antoine Letessier-Selvon [LS05], who proposes the hypothesis that the domain of the variables (θ , ϕ and a set of other physical parameters) covered by the detector, can be split in complementary regions, over which the time part of the acceptance can be factorized. He introduces the factorizable acceptance model (FAM), assuming that the time variations of the acceptance are the product of a daily variation in JD_{rest} and of a seasonal variation in JD_{int} (see appendix A). Thus, in order to compute the coverage map, the full time information is subdivided into an integer and the decimal places. Now, basically the same steps are taken as for the shuffling JD method: Again the azimuth angle distribution is assumed as flat, while the zenith angle distribution is kept by using the event data. The time information, i.e. both JD_{int} and JD_{rest} , is kept in two list now, and both are shuffled after each run. Then they are recombined for the generation of each fake event.

1. get one value from each of the lists of zenith angle θ , Julian day integer JD_{int} and Julian day decimal places JD_{rest} ; randomly select an azimuth angle ϕ
2. transform the collected information to equatorial coordinates
3. fill the corresponding pixel obtained by HEALPix
4. having iterated through all values in the full lists, shuffle the lists of Julian day integer and Julian day decimal places and re-start at 1.

This procedure is repeated as often as necessary in order to create the desired number of data samples (i.e. N_s times). The impact of the FAM on the coverage computation is independent on the computation method; thus, it can also be exploited for the semi-analytical method described in section 5.3.

5.2.3 Julian Day Distributions

The distributions of Julian day as a double (JD) and subdivided into integer (JD_{int}) and decimal places (JD_{rest}) are given in figure 5.3. The histogram of JD shows the growth of the surface detector (more or less linear) as well as seasonal variations: Three equidistant peaks are visible within the steady rise of entries, corresponding to the three summers (in southern hemisphere) in the years of data taking: Larger trigger rates are expected for periods of higher temperatures. Furthermore, local minima are visible, which have been caused by maintenance and operation problems in the respective periods, e.g. in the middle of 2005.

Basically, the distribution of JD_{int} would look the same, apart from possible binning effects. Therefore, the JD_{int} histogram has been produced differently: A linear function has been fitted to the distribution of JD_{int} , in order to model the detector growth under the assumption, that the deployment of surface detector tanks has been carried out linearly; this fit function, which is displayed in the upper histogram for convenience, was subtracted from the JD_{int} histogram, and the periods of all three years have been overlaid to the interval of one year. The aim was to display a periodicity of the seasonal variations. These variations are observable within the JD_{int} histogram obtained, indicated by the fact, that larger entries are observed for the rather warm seasons of spring and summer. Nevertheless, the assumption of a constant tank deployment frequency may be incorrect, as tanks may be deployed less likely during the cold season, for example; secondly, results may also be biased by detector downtime effects and insufficient statistics of only three years. A clearer view upon seasonal effects can only be gained for data taking periods at a constant detector size and a 100% duty cycle.

The JD_{rest} histogram with the x-axis in hours of the day, centered on noon, shows the daily variation; it is mostly due to expected periodical temperature effects [Arm04] and the distribution can be fitted by a simple sine function $p_0 + p_1 \cdot \sin[\frac{2\pi \cdot JD_{rest}}{24} + p_2]$, which yields $\chi^2/dof = 0.96$. This fit is applied only in order to show the periodicity, without claiming that a simple sine function is the best model for these daily variations. A flat fit for example is not so much supported by the data, giving $\chi^2/dof = 10.4$, which is significantly worse. These daily effects are supposed to be averaged out for data taking periods of full years, as the beginnings of sidereal and solar day coincide every ~ 365.25 solar days.

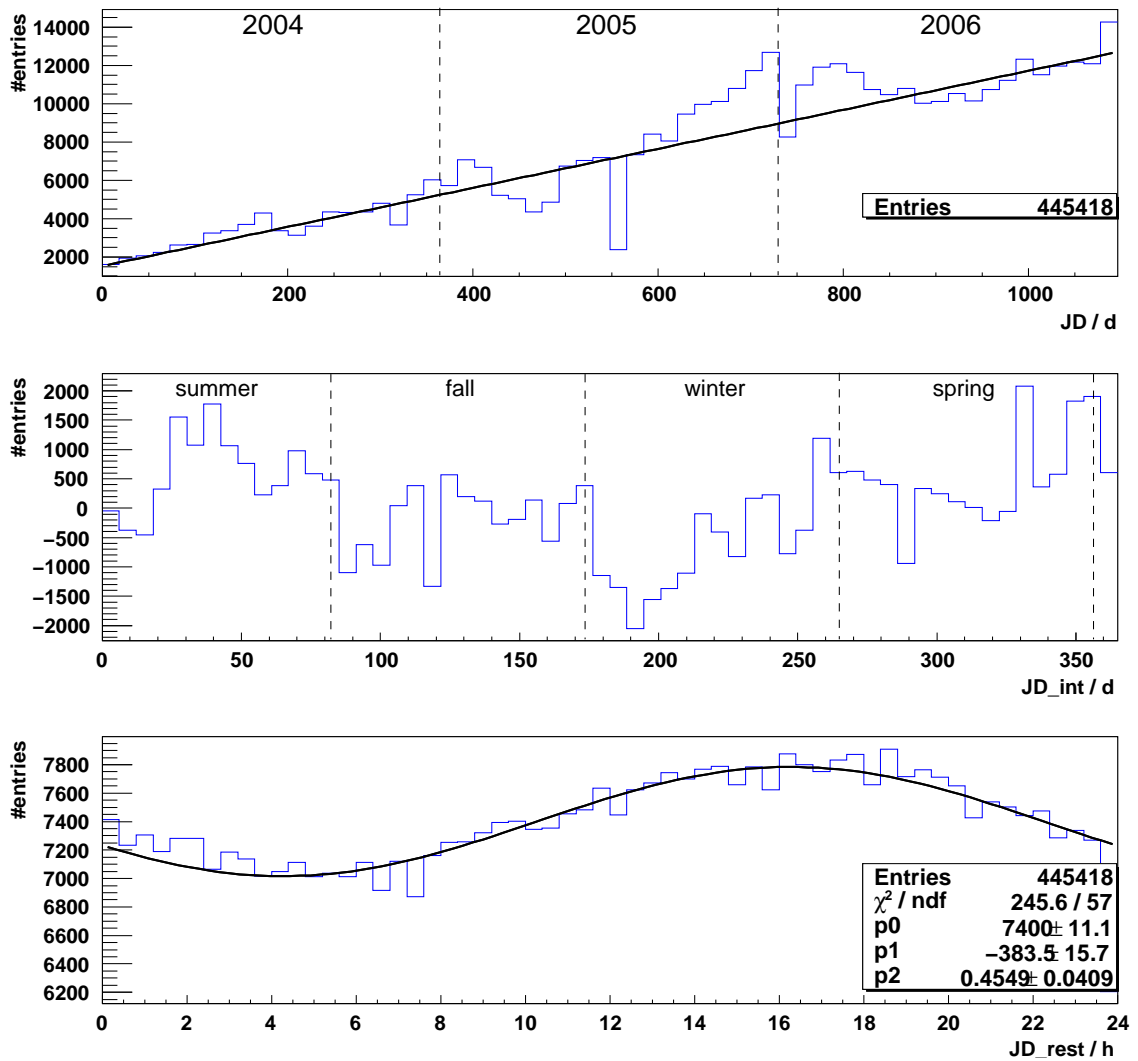


Figure 5.3: Distributions of Julian day as a double (JD, upper histogram, full timing information) and subdivided into integer (JD_{int}, middle histogram) and decimal places (JD_{rest}, lower histogram). See text for details.

5.2.4 Advantages and Drawbacks

The main advantage of the shuffling method is its simplicity considering both the principle and the implementation. Furthermore, it takes into account detector acceptance effects naturally, and scrambling the splitted time information in addition allows for both daily and seasonal variations.

Nevertheless, both techniques suffer from partially introducing true anisotropy into the coverage on the one hand, and creating fake anisotropy on the other hand. Firstly, real anisotropy modifies the arrival time distribution, because the time information is not independent of the right ascension, being shifted from one to another by an amount that varies from 0 to 24 hours in one year [Ham04]. Both time shuffling methods preserve this distribution and thus introduce real anisotropy into the coverage; this can be reduced by considering only data periods that span full years at a constant detector size, with the latter not being realistic for now. The second drawback is created by statistical fluctuations in the initial data sample of real events, that are preserved during the scrambling process. These initial fluctuations limit the precision regardless of the number of fake data samples produced, and therefore even may introduce fake anisotropies. Depending on the number of events in the initial sample, the magnitude of such self-made anisotropies amounts to a few percent in terms of deviation from the true coverage [d'O05]. This can be shown by means of the basic quality check for the coverage, i.e. creating fake anisotropy in a map of events and comparing this manipulated observation with the expectation obtained from the coverage map. Thus, especially for the statistically limited number of high energy events, these fluctuations rise.

5.3 Semi-Analytical

The semi-analytical coverage computation method relies on applying fits to the distributions that determine the detector acceptance. It is very challenging to obtain a realistic model, that takes into account time dependence of the acceptance due to array growth, weather effects etc. To do so, however, there basically are two options: (i) make use of the knowledge of the detector, i.e. exploit correlations that may be found in the monitoring data, such as temperature, pressure, number of available tanks, trigger and event rates, etc. (ii) obtain it directly from the arrival times, the way the shuffling methods do, and apply fits to the respective distributions.

In principle, this thesis follows the path of (ii), taking into account, that the PAO SD design provides an acceptance, that is almost independent of both azimuth angle and sideral time [Ham05]. So, in this chapter only the quantity, that the distribution of shower detections depends upon most, i.e. the zenith angle, will be fitted, while the azimuth angle will be assumed as equally distributed, as before, and the time information will be taken randomly out of its original distribution:

1. randomly select θ from the fit function of the zenith angle distribution; randomly select a value from the original distribution of Julian days JD (alternatively select random values from the original distributions of JD_{int} and JD_{rest} and recombine them); randomly select an azimuth angle ϕ
2. transform the collected information to equatorial coordinates

order of polynomial	3	4	5	6	7	8	9
χ^2/dof	4.66	3.61	1.18	1.10	1.10	1.10	1.09

Table 5.1: χ^2/dof -test results for various polynomial fits to the zenith angle distribution.

- fill the corresponding pixel obtained by HEALPix

This procedure is repeated as often as necessary in order to create the desired number of fake events (i.e. “ N_f ” times). In order to establish comparability of the maps computed by the different methods, the set of real events should be the same in any case, and the number of fake events created should be equal for all methods (i.e. $N_f = N_e \times N_s$).

There are several ways of fitting the zenith angle distribution; two methods will be presented in the following sections, one of them being chosen as the best polynomial, and the other one being motivated physically.

5.3.1 Polynomial Zenith Angle Fit

In this first method, the zenith angle distribution is fitted by a simple polynomial of sixth order without any physical motivation. However, the polynomial fit function is forced to intersect the y-axis at the point of origin, i.e. $p_0 \equiv 0$, to account for the infinitely small solid angle at $\theta \approx 0^\circ$:

$$p_0 + p_1 \cdot \vartheta + p_2 \cdot \vartheta^2 + p_3 \cdot \vartheta^3 + p_4 \cdot \vartheta^4 + p_5 \cdot \vartheta^5 + p_6 \cdot \vartheta^6, \quad (5.1)$$

with $\vartheta = \frac{\pi}{180^\circ} \theta$ and θ in degree; a polynomial of lower order does not fit the distribution well, while higher order polynomials do not lead to any improvement. This can be verified by checking χ^2/dof , as given in table 5.1. The fit, its parameters and the original distribution are shown in the upper plot of figure 5.4: It describes the data well, which is supported by a value of $\chi^2/dof = 1.10$.

5.3.2 Physical Zenith Angle Fit

A physically motivated fit of the zenith angle distribution should account for some basic physically explicable characteristics of this distribution. Firstly, assuming full detector acceptance, the distribution is supposed to be proportional to $\cos \theta \sin \theta$ for geometrical considerations. The $\cos \theta$ part comes from the effective detector surface corresponding to the scalar product of its normal and the arrival direction of the respective shower, while the $\sin \theta$ part is due to the solid angle element on the sphere in horizontal coordinates equivalent to the cosmic ray’s origin. At large zenith angles, the increasing atmospheric depth causes an increase of the attenuation of shower particles, which results in an exponential drop of shower detections at ground. This cutoff can be modeled through a Fermi-Dirac function. Such showers commonly are referred to as old showers, being a sign of the amount of atmospheric depth penetrated after initiation. Furthermore, the depletion at small zenith angles is not sufficiently described by the $\sin \theta$ part from solid angle consideration, but can be modeled by a polynomial of small degree n ; at this angular range, showers are rather young, thus having produced rather few particles so far, which

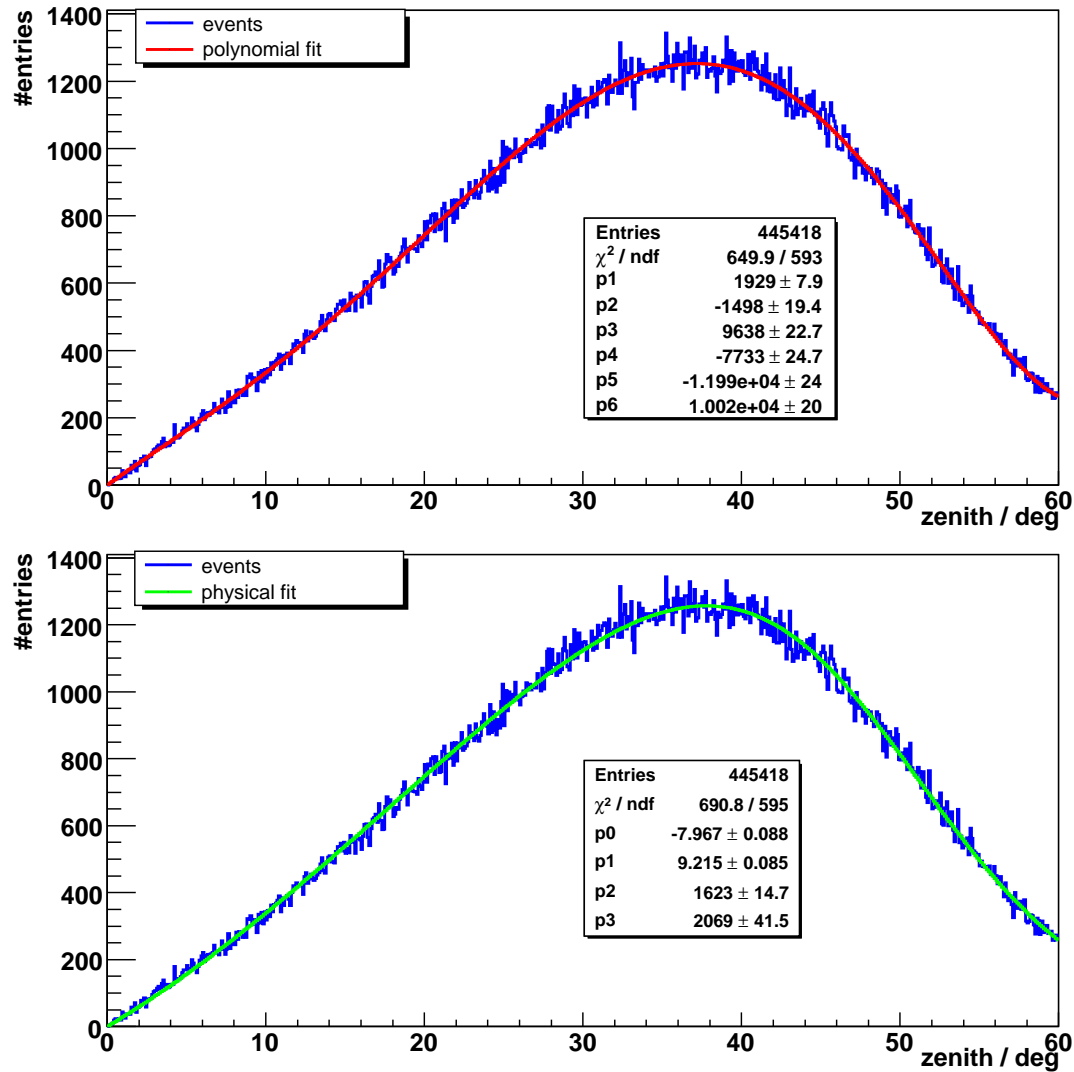


Figure 5.4: Zenith distribution (blue) with polynomial fit (top, red) and physical fit (bottom, green), respectively. Fit parameters and errors are given in the central box. Both fits seem to describe the data well, with the polynomial fit of sixth degree (equation 5.1) performing slightly better than the physically motivated fit (equation 5.2): $(\chi^2/\text{dof})_{\text{poly}} = 1.10 < 1.16 = (\chi^2/\text{dof})_{\text{phys}}$.

reduces the trigger probability. It has been shown, that $n = 1$ is sufficient to model the zenith angle distribution, so that finally the following model is obtained [Ham04]:

$$\cos(\vartheta) \sin(\vartheta) \cdot \frac{1}{1 + \exp(p_0 + p_1 \cdot \vartheta)} \cdot (p_2 + p_3 \cdot \vartheta), \quad (5.2)$$

with $\vartheta = \frac{\pi}{180^\circ} \theta$ and θ in degree. The fit, its parameters and the zenith angle distribution are shown in the bottom plot of figure 5.4: The physically motivated fit yields a good description of the zenith angle distribution, which is also verified by the result of the χ^2 -computation, $\chi^2/dof = 1.16$

5.3.3 Comparison of Fits

The simple assumption of a polynomial description of the zenith angle distribution leads to a slightly better value for χ^2 , $(\chi^2/dof)_{poly} = 1.10$, compared to the result obtained by means of the physically motivated fit function, $(\chi^2/dof)_{phys} = 1.16$. A more detailed comparison of both zenith angle fits is given in figure 5.5. The upper plot shows both functions; they intersect six times, even though the differences do not seem to be large. In order to display the relative behavior of both fit functions, the relative difference has been computed and plotted in the bottom figure. The discrepancies amount to 2% for the full zenith angle range at worst, except for values of θ below 6° , where it increases to $\sim 16\%$. Such larger differences have to be seen in connection with the evanescent event rate for vertical showers ($\theta \approx 0$), which reduces the contribution of this effect to the coverage map. Investigation of further impact of these differences on coverage computation will be performed in the next chapter 6.

5.4 Coverage Maps

The resulting maps of all coverage computation methods are shown in figure 5.6; based on the set of 445418 real events, 4,454,180,000 fake events have been generated to fill the maps. No big difference is visible to the naked eye between the maps, and they all show the necessarily fundamental features of a coverage map: They are almost smooth, although no smoothing algorithm has been applied, and all maps are more or less symmetric around the axis of the Earth, which agrees with the isotropy assumption as expected. However, some differences are observable without further investigation: The maps computed by the shuffling method are slightly asymmetric around the southpole, which is caused by daily and seasonal variations observable in the JD distributions, and has been explained in subsection 5.2.4. This feature is not observable in the resulting maps for the semi-analytical method, as here random values out of fit functions are used, which averages out the effect. However, small differences are also observable between the semi-analytically computed coverage maps in the southpole region. Further exploration of these aspects follows in chapter 6, providing a more convenient method of investigating and displaying the coverage maps and their differences.

Making use of all 445418 T5 events with zenith angle $\theta < 60^\circ$ without applying an energy cut has an impact on the possible applications of the resulting coverage maps: The bulk of lower energy events, especially below full trigger efficiency ($energy < 3 \text{ EeV}$),

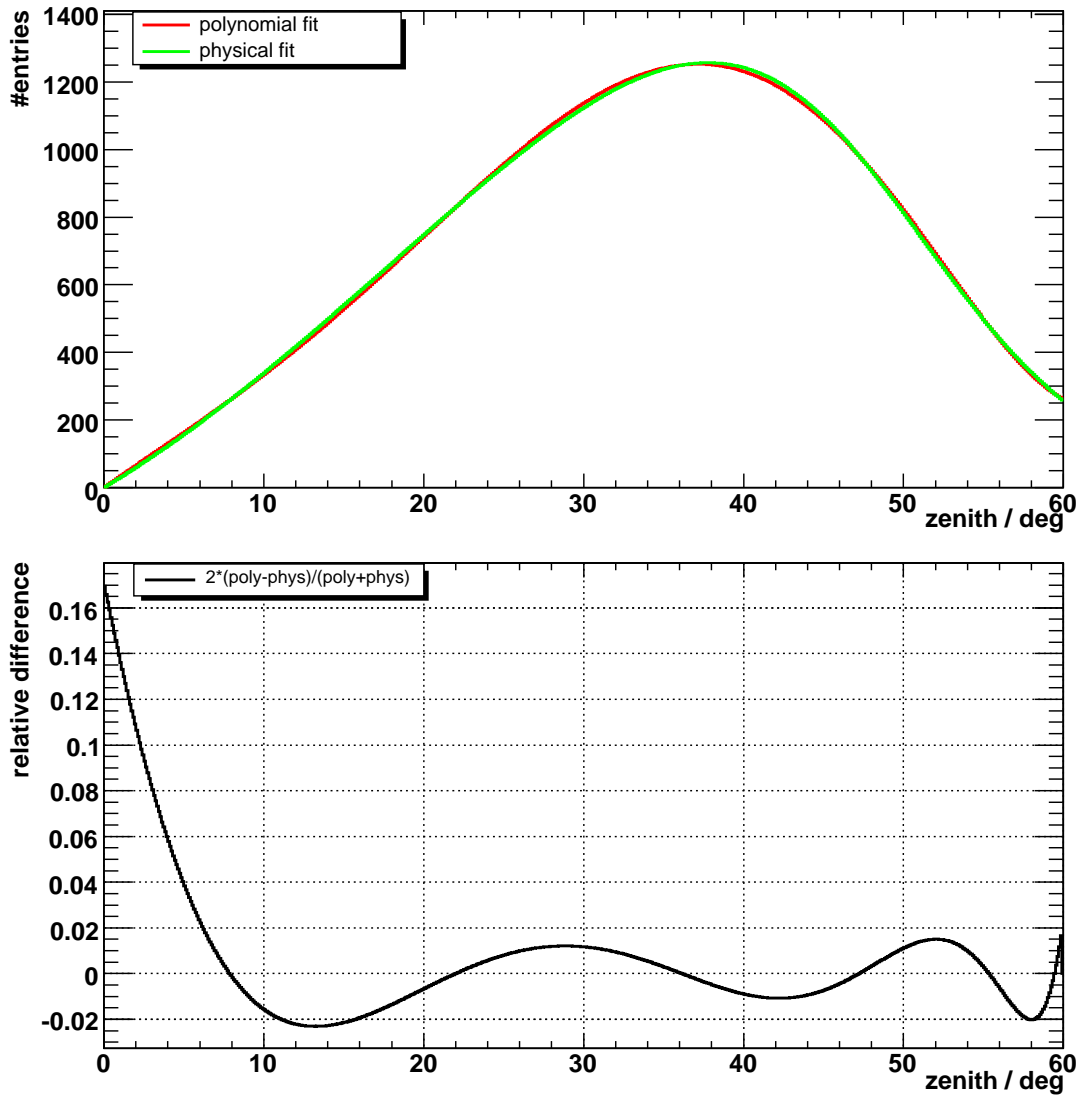


Figure 5.5: Comparison of zenith angle fits: The top plot shows a direct comparison of both zenith angle fits with the polynomial fit in red and the physically motivated fit in green. The bottom figure displays the relative difference of both fit functions. At worst it amounts to 2% for zenith angles above 6° , while increasing to $\sim 16\%$ for smaller θ .

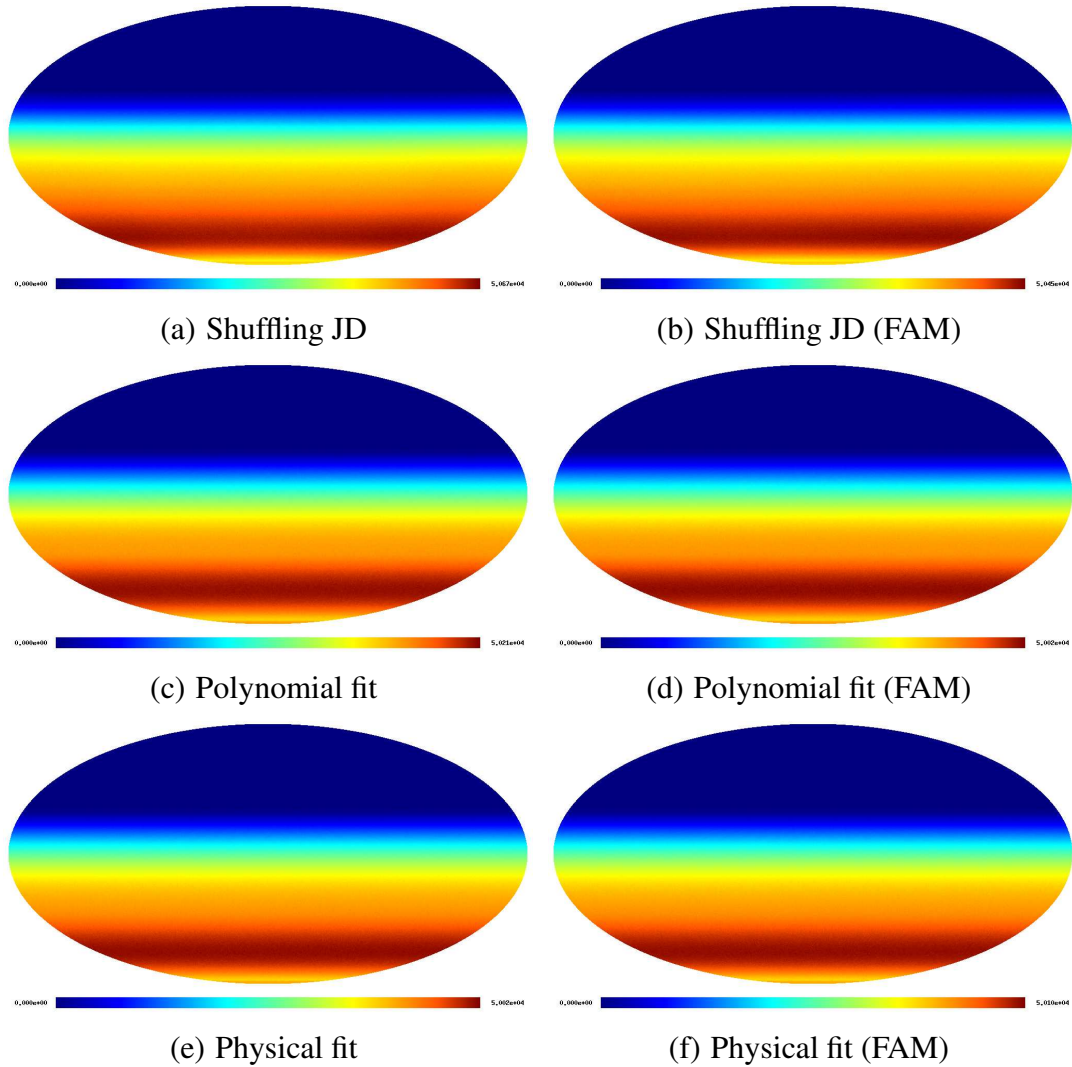


Figure 5.6: Coverage maps for various coverage computation methods; declination is plotted vertically, while the horizontal axis shows right ascension. The Mollweide projection of the sphere displays latitude, i.e. declination, in parallel lines. The resolution is $N_{pix} = 196608$. The two maps on top show the results obtained by shuffling the time information, the other maps display the coverage obtained from the semi-analytical method when using the polynomial fit (middle) or the physically motivated fit (bottom), respectively. On the left only the simple version of the respective method is applied, while the maps on the right show the results for the FAM based versions, i.e. for the subdivision of the time information into JD_{int} and JD_{rest} .

which dominates the number of entries in the shower parameter distributions, makes these maps most appropriately applicable to large scale anisotropy search. Firstly, the angular resolution of lower energy events is poor, which basically does not allow any point source search. In addition, deflection due to galactic and extra-galactic magnetic fields is stronger for primary particles carrying lower energies. Secondly, it is much more difficult, to reach a level of minimum significance with respect to the identification of sources of highly energetic cosmic rays. The following section is dedicated to describing, how to provide a coverage applicable for small scale anisotropy search.

5.5 Full Acceptance

The distributions of some shower parameters depend on the energy of the incoming cosmic ray primary. With respect to coverage computation, this is especially relevant for the zenith angle distribution; applying a lower limit cut to the energy is supposed to have no influence on the azimuth angle and Julian day distributions. The particles of an air shower, that arrives at a larger zenith angle of up to 60° , suffer from a greater atmospheric depth. Thus, these particles are attenuated more likely before the cascade reaches ground level, which diminishes the trigger probability of the corresponding showers. The value of this phenomenon depends on energy, of course. Above an energy of 3 EeV, it is supposed to vanish and full shower trigger efficiency is expected for zenith angles below 60° .

The impact of energy dependent detector acceptance and trigger efficiency on the coverage is obvious: In order to search for point sources of highly energetic particles, i.e. so-called small scale anisotropies, it makes sense to compute the coverage only from events above the full efficiency limit. Otherwise, the bulk of lower energy events unnecessarily biases the estimated coverage in the following way: It becomes more difficult to detect anisotropy, especially in regions corresponding to zenith angles of overestimated (with respect to energies beyond 3 EeV) trigger rate. More events of highest energy are then necessary to provide a certain level of significance, when in turn calculating the excess map, i.e. comparing observed and expected number of events arriving from accessible celestial directions. Secondly, the angular resolution of the SD array improves with increasing energy, while the loss of directional information due to (extra-)galactic magnetic fields decreases, which also is a fundamental necessity for the goals of point source search.

5.5.1 Zenith Angle Distribution

In order to account for this impact, the zenith angle distributions have been computed for the same set of events again, but only considering showers of energies above 3 EeV; the energies have been estimated via cross calibration with FD events by means of hybrid data, as described in chapter 2.3.1. Particle attenuation due to atmospheric depth that increases with zenith angle does not play any role beyond full efficiency; only purely geometric effects are expected. Therefore, the zenith angle distribution should feature the shape of $\cos(\theta) \cdot \sin(\theta)$ in case of isotropic arrival directions of the events. There are two obvious differences between the zenith angle distribution for data without and with the energy cut: On the one hand, the maximum of the distribution is shifted from $\sim 38^\circ$ to

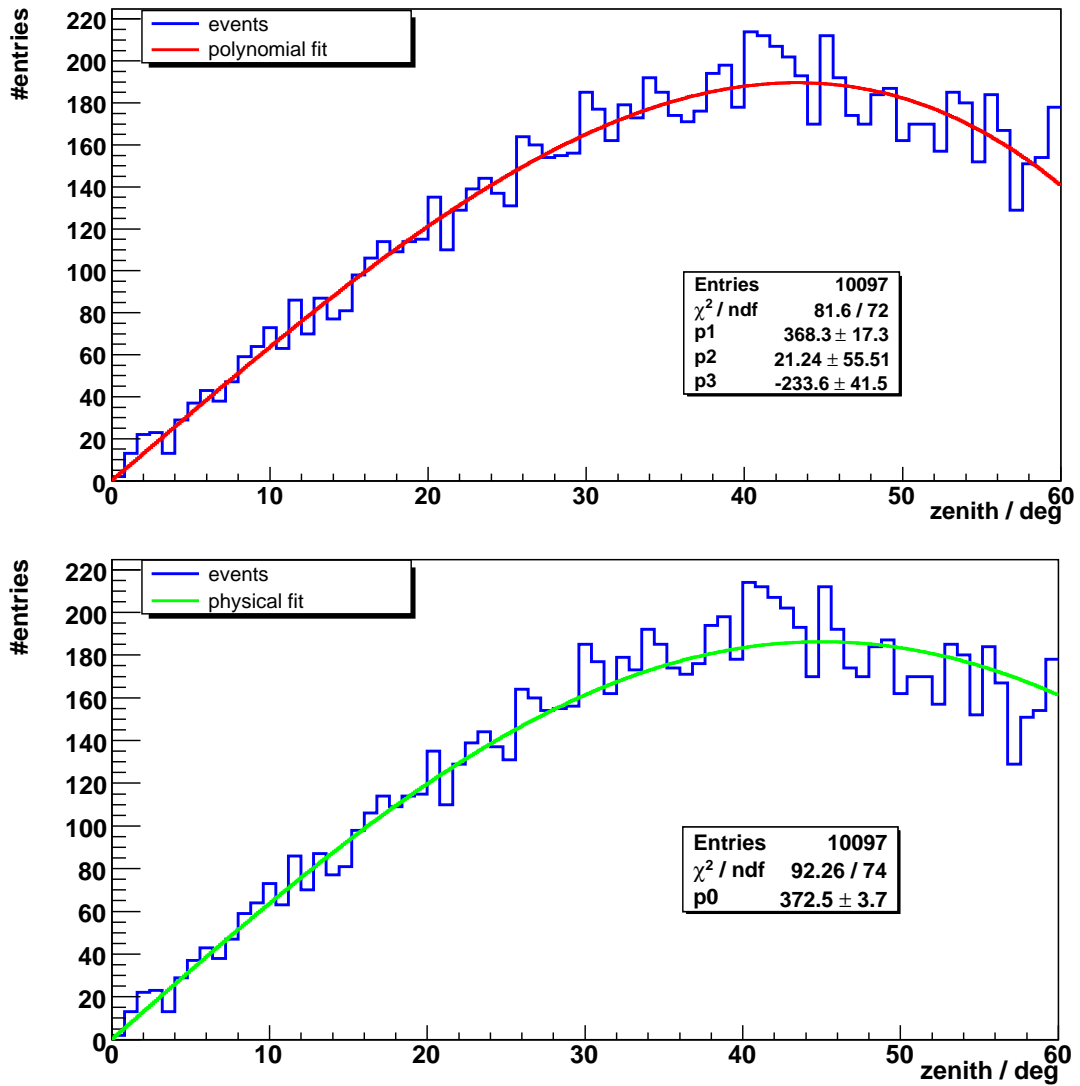


Figure 5.7: Zenith distribution (blue) above full efficiency with polynomial fit (top, red) and physical fit (bottom, green), respectively. Fit parameters and errors are given in the central box. Both fits describe the data well, while the polynomial fit of third degree (equation 5.3) performs slightly better than the physically motivated fit (equation 5.4): $(\chi^2/\text{dof})_{\text{poly}} = 1.13 < 1.25 = (\chi^2/\text{dof})_{\text{phys}}$.

$\sim 45^\circ$ and on the other hand, the decrease of entries for large zenith angles is less strong. The impact of the differences noted on coverage computation will be investigated in the next section 5.5.2. It has to be mentioned, that the distributions of azimuth and Julian day do not feature such energy dependence.

In order to compute the corresponding coverage with the semi-analytical methods, new fit functions had to be found and applied to the distribution. As before, a simple polynomial fit (equation 5.3) has been performed, as well as a physically motivated fit (equation 5.4). The polynomial fit could be reduced to an order of 3, still providing a good description of the data, $(\chi^2/dof)_{poly} = 1.13$. Again, the function is forced to intersect the y-axis at the point of origin, i.e. $p_0 \equiv 0$

$$p_0 + p_1 \cdot \vartheta + p_2 \cdot \vartheta^2 + p_3 \cdot \vartheta^3, \quad (5.3)$$

with $\vartheta = \frac{\pi}{180^\circ} \theta$, θ in degree and $p_0 \equiv 0$. The physically motivated fit only accounts for zenith angle dependent geometry this time, as all acceptance effects are supposed to vanish at full efficiency:

$$\cos(\vartheta) \sin(\vartheta) \cdot p_0, \quad (5.4)$$

with $\vartheta = \frac{\pi}{180^\circ} \theta$ and θ in degree. This approach provides sufficient description of the data as well, $(\chi^2/dof)_{phys} = 1.25$. The fits, their parameters and the zenith angle distribution are shown in the upper and bottom plot of figure 5.7, respectively. As before, the polynomial fit performs slightly better, $(\chi^2/dof)_{poly} = 1.13 < 1.25 = (\chi^2/dof)_{phys}$. In addition, the same comparison of the fit functions is performed, that already has been performed for the case of no energy cut applied. The results are displayed in figure 5.8. The functions intersect two times, while agreeing well for most of the zenith angle range. The relative difference amounts up to three percent below 54° and increases up to $\sim 14\%$ for angles close to the cut value of $\sim 60^\circ$. Anyway, one has to bear in mind, that smaller statistics are available for this energy range. From this point of view, the zenith angle distribution agrees remarkably well with the expectation of purely geometric detector acceptance. This supports the idea of an isotropic distribution of sources, as long as cosmic rays can be assumed as directly pointing back to their origin, i.e. as long as deflection mechanisms via magnetic fields are negligible.

5.5.2 Coverage Maps

The coverages are computed in the same way as described in the respective section above. By means of 10097 real showers, 100,970,000 fake events have been generated to fill the maps; This is about a factor of 45 less events available compared to the case of no energy cut applied. The resulting maps are plotted in figure 5.9. They differ strongly from the maps obtained when applying no energy cut (figure 5.6), which is expected due to the differences between the corresponding zenith angle distributions. Both clearly show the limit of the visible sky above $\delta \sim 25^\circ$. The maximum in the event distribution at energies above 3 EeV is located at the south pole, where a local maximum is observable for the maps without energy cut as well. This can be explained by the fact, that this region is covered by the view of the observatory continuously. Moreover, this is amplified in case of applying the energy cut, as the zenith angle range necessary to reach that south pole region

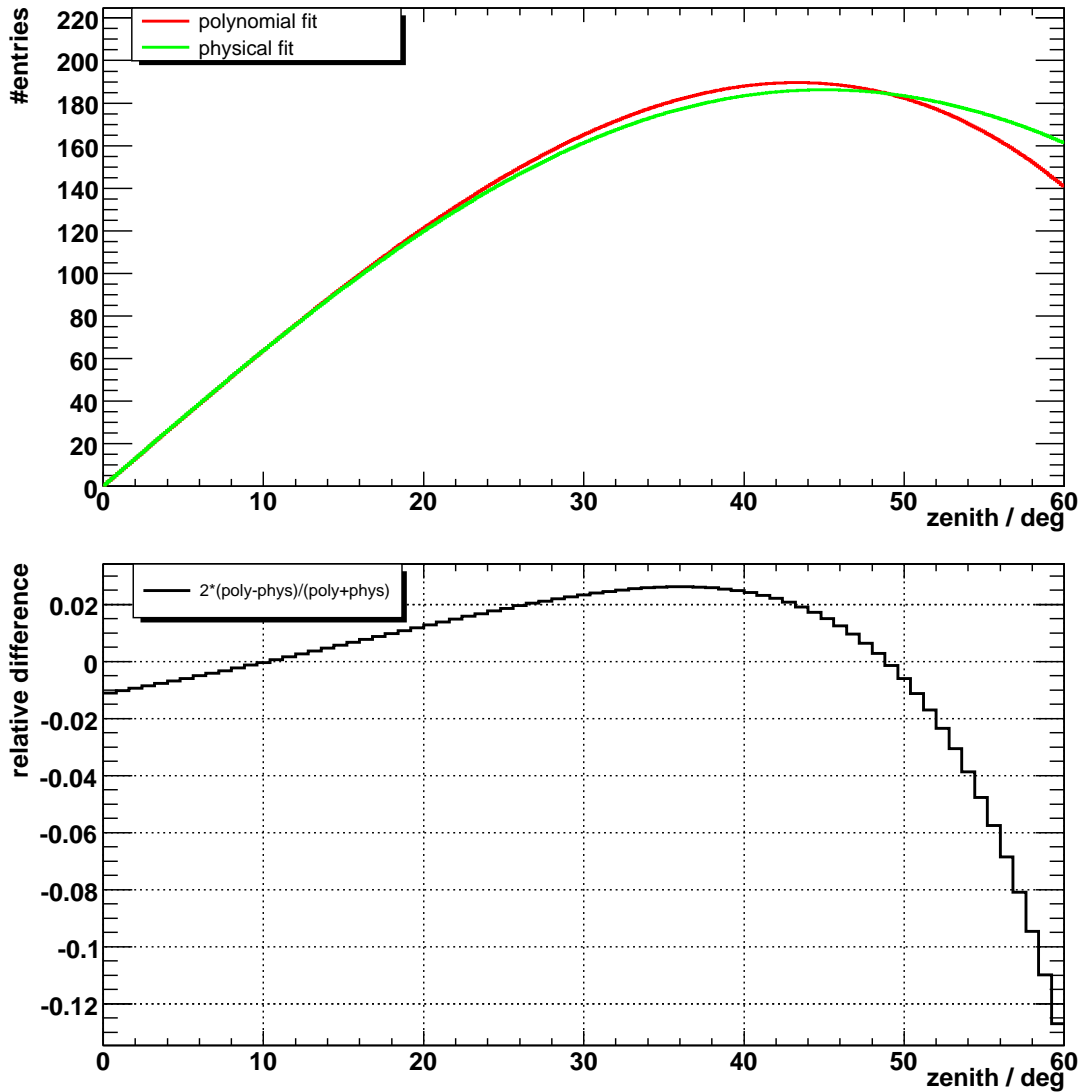


Figure 5.8: Comparison of zenith angle fits above full efficiency: The top plot shows a direct comparison of both zenith angle fits with the polynomial fit in red and the physically motivated fit in green. The bottom figure displays the relative difference of both fit functions. It amounts to a few percent for most of the zenith angle range, while increasing to $\sim 20\%$ for $\theta \rightarrow 0$.

($50^\circ < \theta < 60^\circ$) provides comparatively larger entries. Furthermore, the relative flatness of the maximum in the zenith angle plot prevents larger entries at moderate declination, which can be observed though in case of no energy cut at $\delta \sim -60^\circ$.

The maps in figure 5.9 do not show huge differences between each other, and again all of them agree with the impact of an isotropy assumption. However, small differences in color can be observed between the results obtained from the different zenith angle fits: Between declination values of $\sim -60^\circ$ and $\sim -80^\circ$, the entries of the polynomial fit map are relatively larger. This can be derived directly from the comparison of the fit functions, as the declination range considered corresponds to zenith angles between $\sim 25^\circ$ and $\sim 45^\circ$, where the polynomial fit provides larger entries as well. Notwithstanding the small statistics available for energies above 3 EeV, such coverage maps have to be computed providing a more appropriate tool necessary for the search of point sources of highly energetic particles, i.e. small scale anisotropy. The aspect of point sources and their impact on the zenith angle distribution will be investigated in chapter 7.

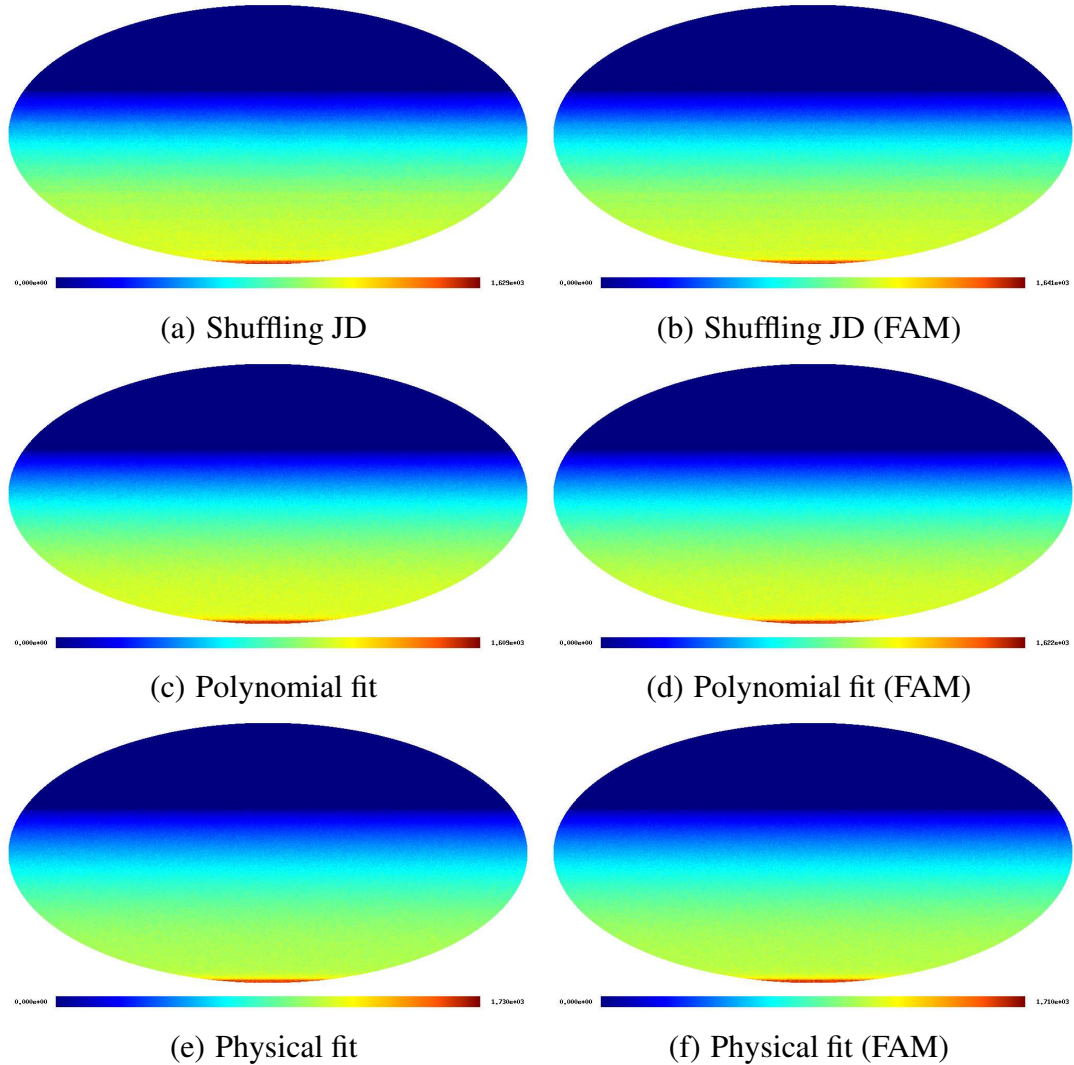


Figure 5.9: Coverage maps above full acceptance ($energy > 3$ EeV) for various coverage computation methods; declination is plotted vertically, while the horizontal axis shows right ascension. The Mollweide projection of the sphere displays latitude, i.e. declination, in parallel lines. The resolution is $N_{pix} = 196608$. The two maps on top show the results obtained by shuffling the time information, the other maps display the coverage obtained from the semi-analytical method when using the polynomial fit (middle) or the physically motivated fit (bottom), respectively. On the left only the simple version of the respective method is applied, while the maps on the right show the results for the FAM based versions, i.e. for the subdivision of the time information into JD_{int} and JD_{rest} .

Chapter 6

Averaging on Lines of Constant Declination

After the creation of a coverage map, it is necessary to check, whether it meets the requirements, that it has been computed for. As the coverage is supposed to provide a tool for anisotropy searches, the fundamental method to check its quality is to create fake anisotropy in the map of events. Then the excess map can be computed by building the difference or the ratio of the manipulated events map and the coverage map. Now, the significance level for identifying the artificial excess as an anisotropy can be calculated [d'005]. However, this is not the aim of this thesis. Instead, an attempt is made to create an inherent method for the quality check of coverage maps.

The assumption of isotropy, that is the fundamental precondition of all coverage computation methods, can be verified in the corresponding map in equatorial coordinates. Isotropy is supposed to lead to a flat distribution of events for a fixed value in declination, as long as either the daily variations of the detector acceptance mostly due to temperature effects can be neglected, or such effects are averaged out more or less through taking into account only data taking periods of full years. Having a look at equation 4.2 again, it is obvious, that an arbitrarily chosen pair of horizontal coordinates determines declination. The observer position is assumed as fixed anyway, and equatorial declination does not depend on time. However, taking into account the time information, i.e. the rotation of the Earth, constant values of declination are displayed as horizontal rings in the equatorial reference frame, as basically noticeable from figure 5.6 (here, due to the projection of the sphere lines are visible instead of rings).

The HEALPix scheme supports this principle of iso-latitudes, as it provides a distribution of pixels on a sphere on lines of constant latitude, see chapter 4.2. On these lines, a one-dimensional averaging can be performed, leading to a constant, i.e. independent of right ascension, number of expected events for a given declination. This is the main exploitable impact of the isotropy assumption on coverage maps. The resulting maps are shown in figure 6.1. Now, it can be checked how strongly a coverage map supports the precondition of isotropy, by comparing the raw map and the map that results from the one-dimensional smoothing; to this end, declination profiles of one-dimensionally smoothed maps obtained from different coverage computation methods are compared.

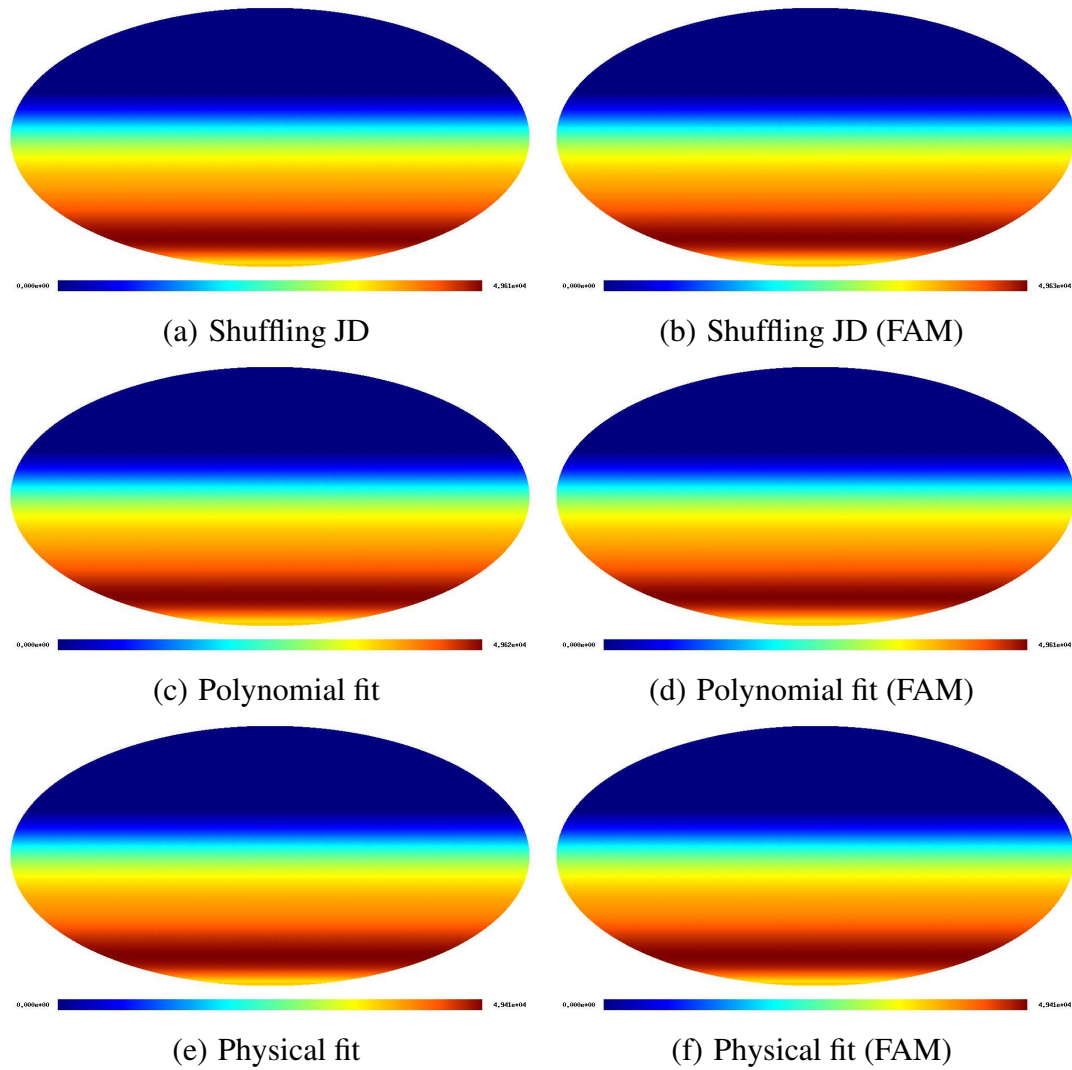


Figure 6.1: The same coverage maps as in figure 5.6, after averaging lines of constant declination. The two maps on top show the results obtained by shuffling the time information, the other maps display the coverage obtained from the semi-analytical method when using the polynomial fit (middle) or the physically motivated fit (bottom), respectively. On the left only the simple version of the respective method is applied, while the maps on the right show the results for the FAM based versions, i.e. for the subdivision of the time information into JD_{int} and JD_{rest} .

6.1 Declination Profiles

A declination profile can be obtained from the smoothed maps by applying a cut at zero right ascension (or anywhere else, due to symmetry), intuitively corresponding to a vertical cut in the horizontal middle of the maps in figure 6.1: The average number of events expected then can be plotted against declination. The resulting profiles can be compared for the different coverage computation methods, in order to possibly find significant disagreement; they contain the full information of the sky maps after applying the one-dimensional smoothing.

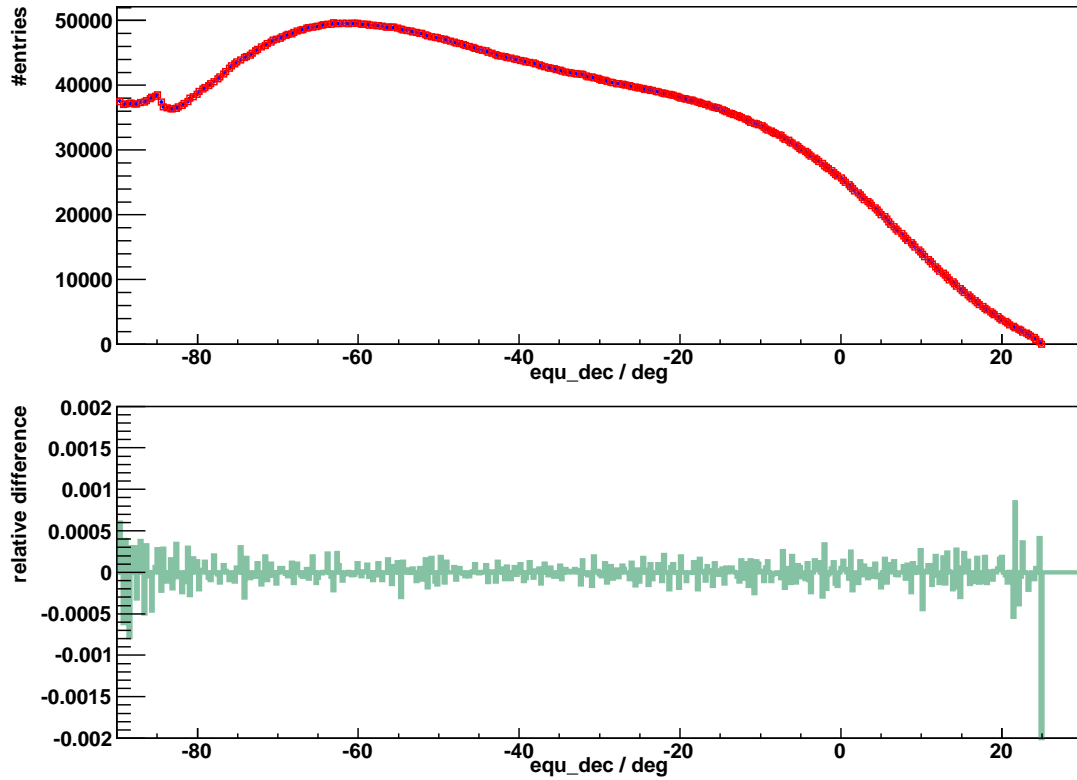
Profile plots are shown in figure 6.2, indicating the results for both raw and FAM-based version of each of the methods. The errors have been determined as the errors of the mean; in the plot they are smaller than the dimension of the markers. Obviously, there are no huge differences for the respective profiles obtained from a raw method and its FAM-based equivalent: Both profiles overlay in such a way, that only one of them is visible in the respectively upper plot. A closer look to the relative difference of these profiles, performed in the respectively lower plot, provides analogy to this observation, as almost the whole range in declination shows a relative difference below 0.5 per mill. Thus, in this section only the FAM-based methods are considered, while further investigation of the differences between raw and FAM-based versions is performed in the next section.

With respect to the comparison of these FAM methods, shown in figure 6.3, it is remarkable that all profiles obtained from the various techniques agree well with each other and all of them show a peaky feature in the south pole region at declination $\delta \sim 85^\circ$. This discontinuous peak in the profile at that value of declination is reasonable, which can be explained as follows: The full aperture angle, i.e. the angular diameter, of the PAO SD view after applying the zenith angle cut $\theta \leq 60^\circ$ amounts to 120° , obviously. The declination range only covers an interval of $\sim 115^\circ$. This is caused by the latitudinal position of the observatory ($\sim 35^\circ$ S), that in turn results in a $\sim 5^\circ$ angular radius cone around the southpole, covering the part of the sky, that is visible continuously, and independently of time. So, a discontinuity is expected between the part of the sky, that is always visible ($-90^\circ < \delta < -85^\circ$), and the part that is not.

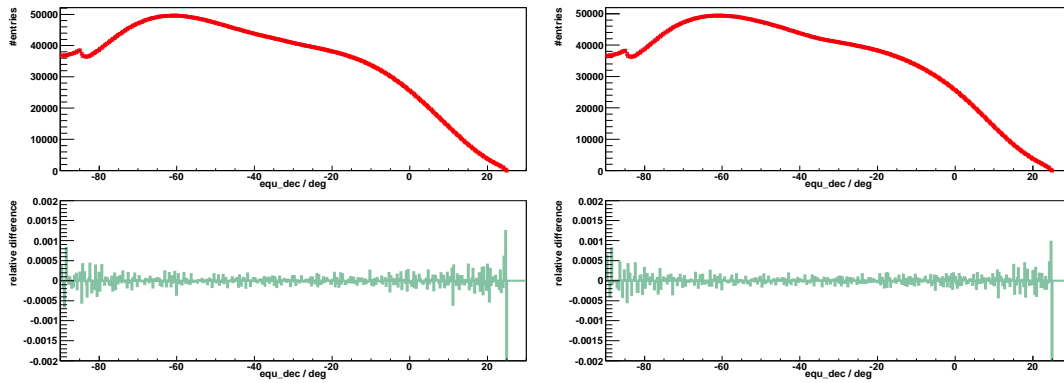
6.2 Spread around Mean

In order to perform further comparison of the declination profiles and the aspect of isotropy, the spread of the distribution of entries for each of the declination values is investigated. The average number of entries at a certain declination, discretized by the pixelization of the sphere, is obtained by building the mean for the corresponding line of constant declination from the raw maps. The distributions of entries on such lines are expected to be flat more or less due to the isotropy assumption. Thus, the deviation from flatness provides a measure of how well the raw map supports or already includes the isotropy assumption. For each line i , the distribution of the relative difference of the entry $N_{i,j}$ in pixel i, j and the mean $mean_i$ is plotted:

$$\frac{N_{i,j} - mean_i}{mean_i}. \quad (6.1)$$



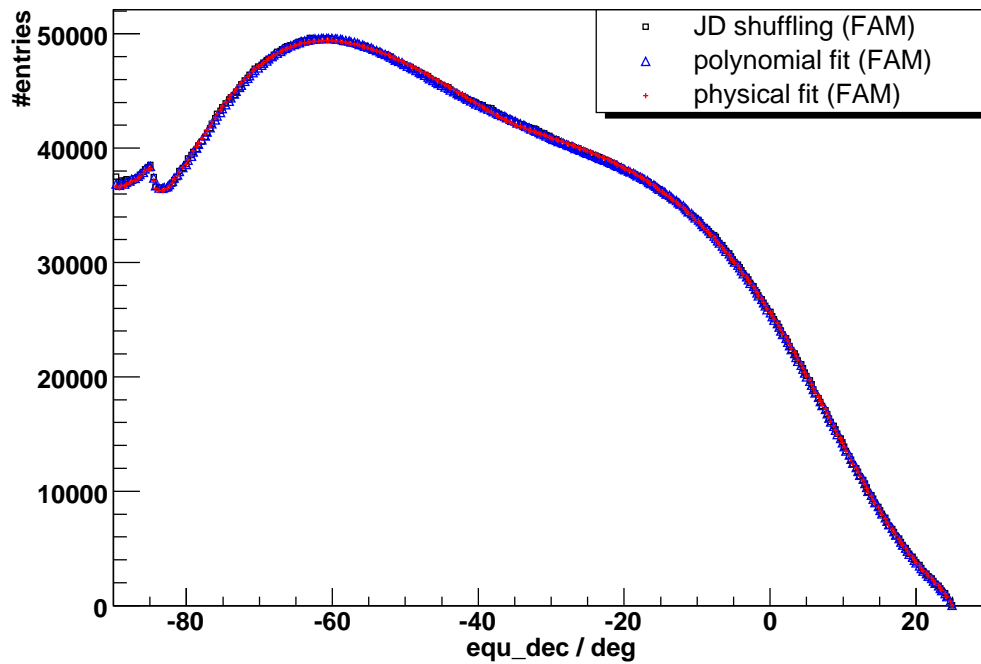
(a) Shuffling JD



(b) Polynomial fit

(c) Physically motivated fit

Figure 6.2: Declination profiles and relative difference between raw (blue) and FAM-based (red) versions of one method; the blue histograms are overlaid by the red ones and thus, they cannot be seen. Declination profiles show the mean number of entries obtained from averaging lines of constant declination for each declination value. The plots show the profiles (the respectively upper histogram) for shuffling the time information (a), applying the semi-analytical method with a polynomial zenith angle fit (b) or the physically motivated zenith angle fit (c), respectively. The bottom plot (green) displays the relative differences between raw and FAM-based versions within the respective method.



(a) Declination profiles for FAM-based methods

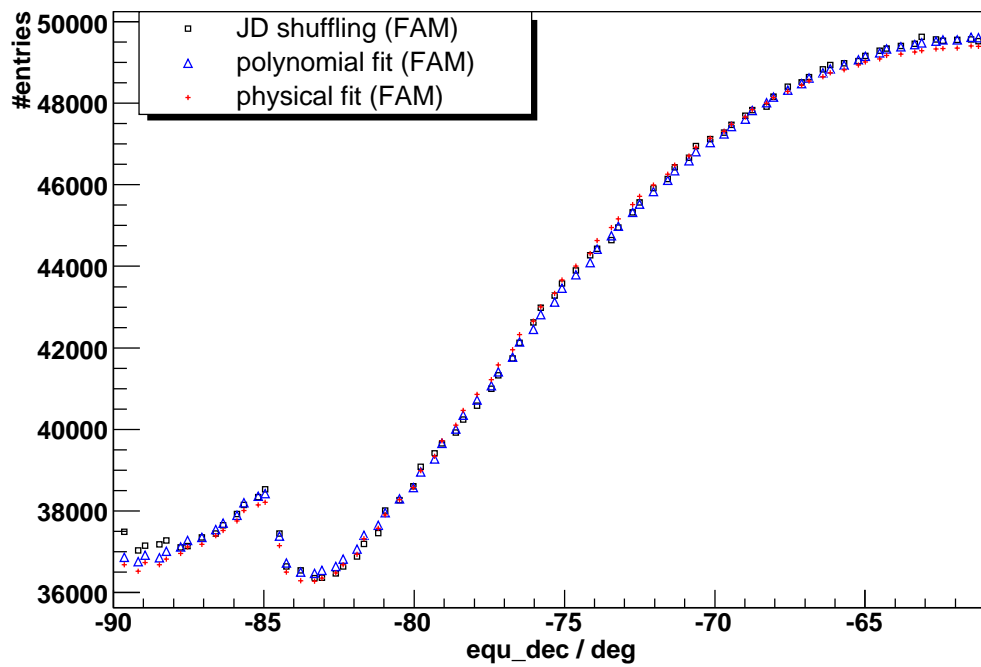
(b) Zoom for declination profiles below -60°

Figure 6.3: The plot on top (a) shows the full profile obtained by shuffling the time information (black squares), applying the semi-analytical method with a polynomial zenith angle fit (blue triangles) or the physically motivated zenith angle fit (red crosses), respectively. The bottom plot (b) provides a zoom into the declination interval showing a peaky feature.

This yields something similar to $\sigma/mean$, which at first view can be written as $\sqrt{N}/N = 1/\sqrt{N}$ with N being the number of entries in an arbitrarily selected pixel. Taking into account, that maximum values of N are of the order of 10^4 , which can be read from the color scale of the maps in figure 6.1, deviations from the mean of the order of 10^{-2} are expected. The RMS (root mean square) of all distributions can be plotted against the associated declination value, providing a profile of the spread, which is shown for each relevant declination value and different coverage computation methods in figure 6.4. The estimated value for the RMS is of the order of 10^{-3} - 10^{-2} , which is close to expectation. Of course, the estimation of the relative difference presented here is rather rough, as it does not account for the fact, that coverage computation already smoothes the entries in one line of constant declination inherently (q.v. outlook 8).

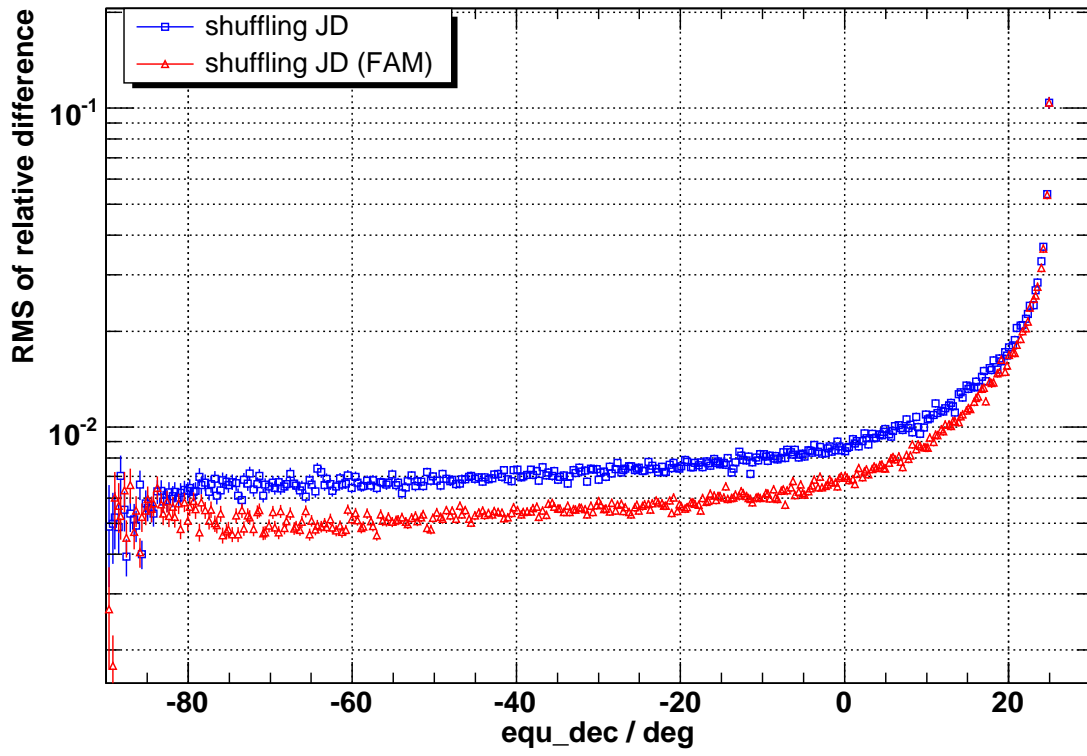
Regardless of the respective computation method of the coverage, for all relevant declination values up to 5° the RMS of the relative difference is below 1 percent; it increases to 10% only in the border area of declination above 5° , for which smaller statistics are available considering the number of entries. It should also be mentioned, that the error bars of the RMS increase for decreasing declination below -45° , which again is caused by smaller statistics, this time due to the decreasing number of pixels. The results of a raw method and its FAM-based equivalent do not differ much, except for the shuffling technique, but systematically: The FAM-based version provides slightly smaller spreads in the respective case. This agrees with expectation, as the separation of the time information into seasonal and daily part multiplies the number of possible times through recombinations, that in principle provide the factorial of the original possibilities. Considering the fact, that time information, rotation of the Earth and right ascension are heavily correlated, it becomes obvious, that rising continuity in the set of available times results in an increase of smoothness for lines of constant declination. For a fixed declination value, specified by a pair of horizontal coordinates, a more smoothly (i.e. flatter) distributed right ascension will be expected, if the time information features a similarly smooth distribution.

Another observation is that, considering the FAM-based versions of the respective computation methods only, the shuffling technique provides a slightly larger RMS, than the semi-analytical ones, see figure 6.7. However, they agree within the errors for declinations smaller than -80° and larger than $\sim 15^\circ$, respectively, with the latter observation being a bit biased by the size of the markers.

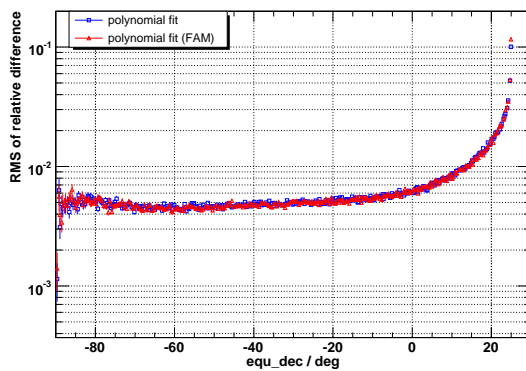
6.3 Conclusions

The main conclusion of this chapter is that the performance of any coverage computation technique can be improved easily by making use of the FAM-based versions in the respective case. This approach automatically yields smoother coverage maps, as it provides the factorial of the originally available number Julian days. Figure 6.4 indicates this effect. Secondly, it could be shown that the semi-analytical methods fundamentally lead to smoother results as well (figure 6.7).

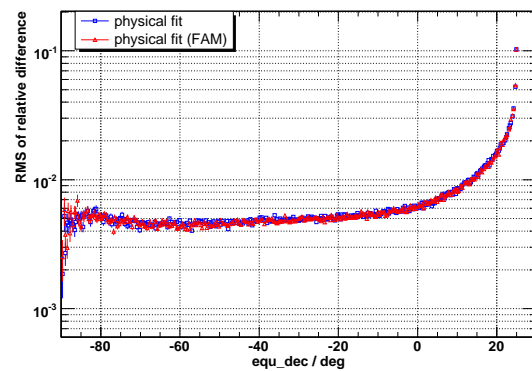
With regard to the declination profiles of the averaged maps, the following conclusion can be drawn: As the profiles agree with each other quite well, all coverage computa-



(a) Shuffling JD



(b) Polynomial fit



(c) Physically motivated fit

Figure 6.4: Relative error of mean from averaging on lines of constant declination. The plot on top (a) shows the result obtained by shuffling the time information, the other plots display the relative error obtained from the semi-analytical method when using the polynomial fit (b) or the physically motivated fit (c), respectively. Blue squares display the results of the simple version of the respective method, while red triangles belong to the FAM-based versions.

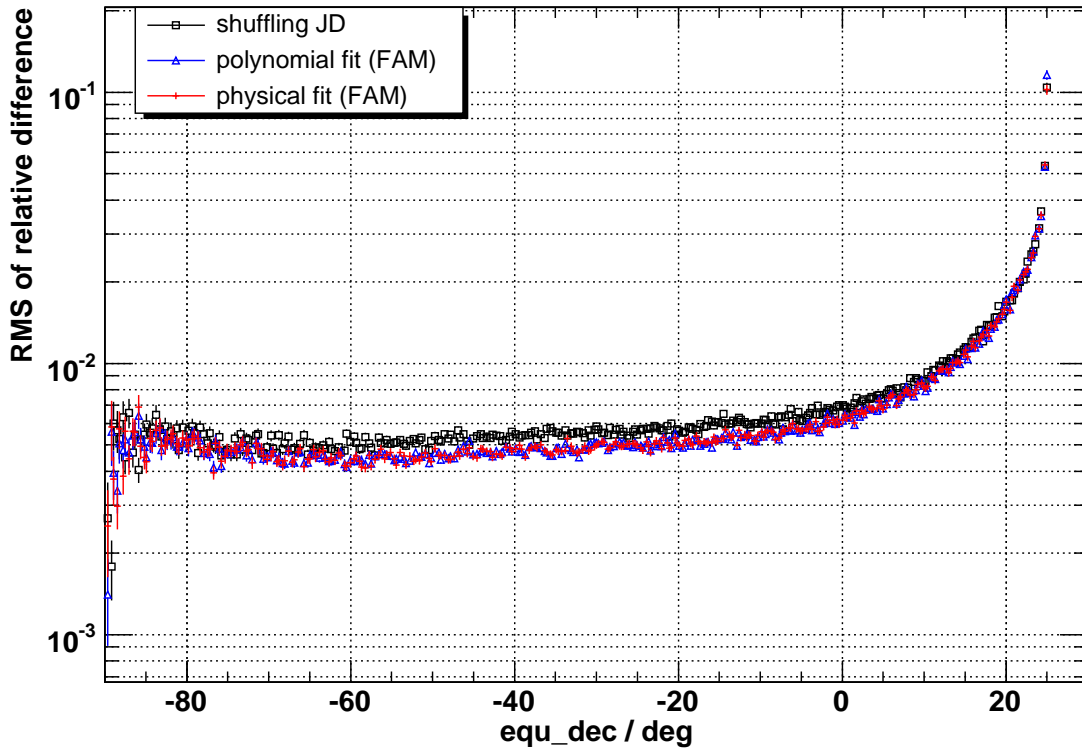


Figure 6.5: Profile of the relative error of the mean value obtained by shuffling the time information (black squares), applying the semi-analytical method with a polynomial zenith angle fit (blue triangles) or the physically motivated zenith angle fit (red crosses), respectively.

tion methods provide similar results on average. This implies, that the idea of averaging on lines of constant declination provides a powerful tool of not only testing and comparing, but also improving coverage maps. As mentioned before, such one-dimensional smoothing is reasonable according to the isotropy assumption. Nevertheless, it has to be remarked once again, that the procedures developed do not provide a tool to judge the quality of coverage maps with regard to anisotropy searches.

For the sake of completion, one-dimensionally smoothed coverage maps are displayed in the galactic reference frame for both considering all events, figure 6.5, and taking into account only events passing the energy cut criterion, figure 6.6. These maps basically show the same results as those in figures 6.1 and 5.9; only the FAM based map obtained from the physically motivated zenith angle fit has been selected in each case, and the same averaging has been applied to the energy cut map, as was described in this chapter.

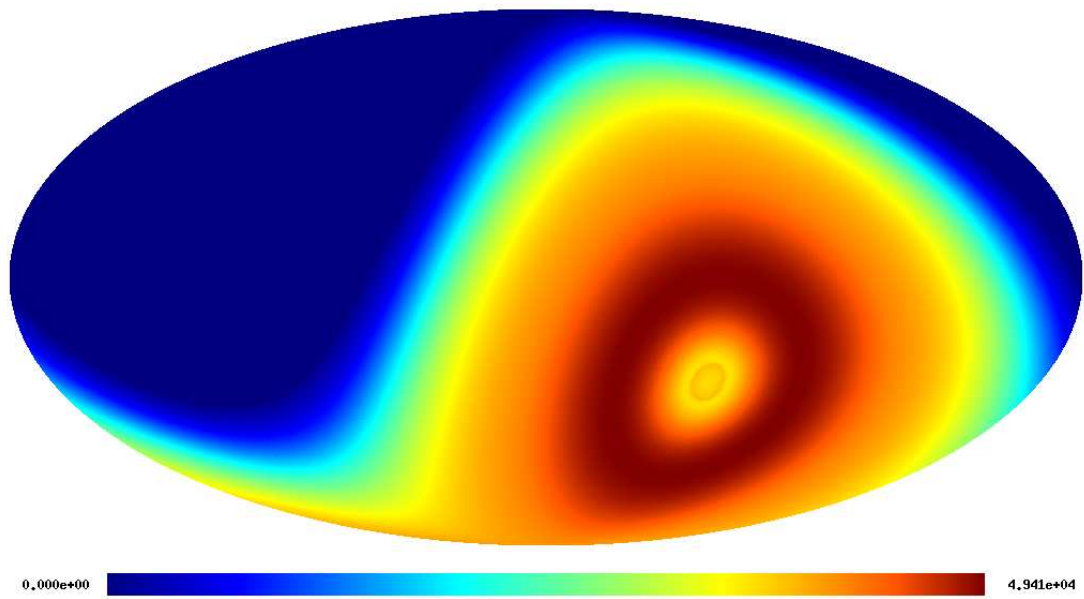


Figure 6.6: Galactic coverage map

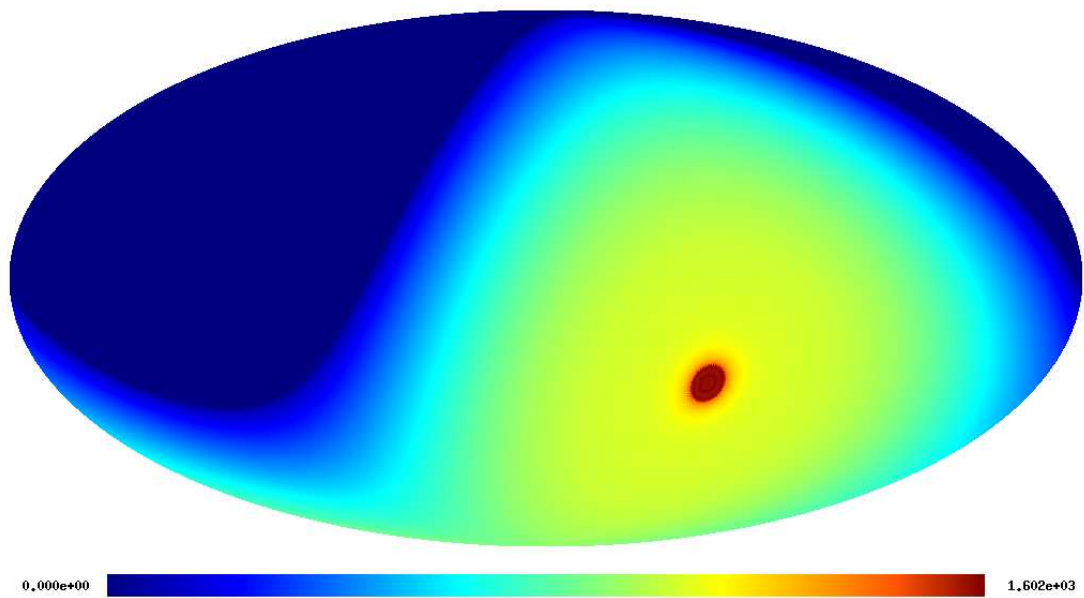


Figure 6.7: Galactic coverage map above full acceptance

Chapter 7

Zenith Angle Distributions of Fake Sources and Fake Isotropy

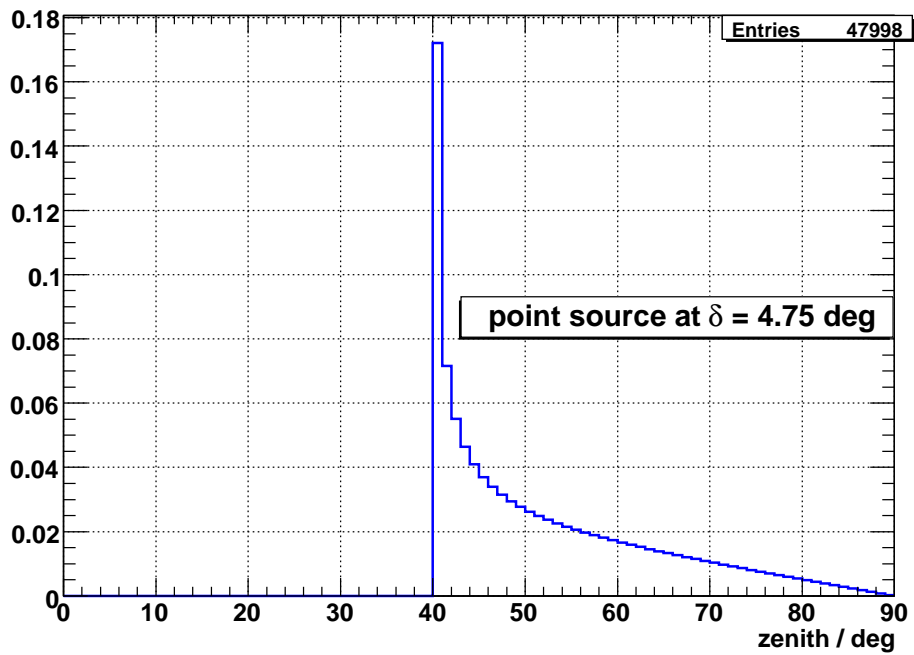
In this chapter, zenith angle distributions of fake point sources are generated. For this purpose, a point source is created at a certain value of equatorial declination, and forced to periodically (every ~ 8.64 seconds) emit a cosmic ray particle. For the sake of simplicity, the distance of the source is neglected, so that the corresponding air shower is assumed to trigger the SD array immediately. The arrival direction in horizontal coordinates can be calculated for every single particle by means of the geographic position of the PAO, the time of emission and the equatorial position of the source. Only one full sidereal day is taken into account, which includes the full directional information available for cosmic rays originating from the respective fake source. Therefore, it is sufficient to specify the equatorial declination of the fake object, as right ascension corresponds to only a shifting in time. Finally, the zenith angle distributions of both single sources and an isotropically distributed bulk of sources are extracted.

7.1 Point Sources

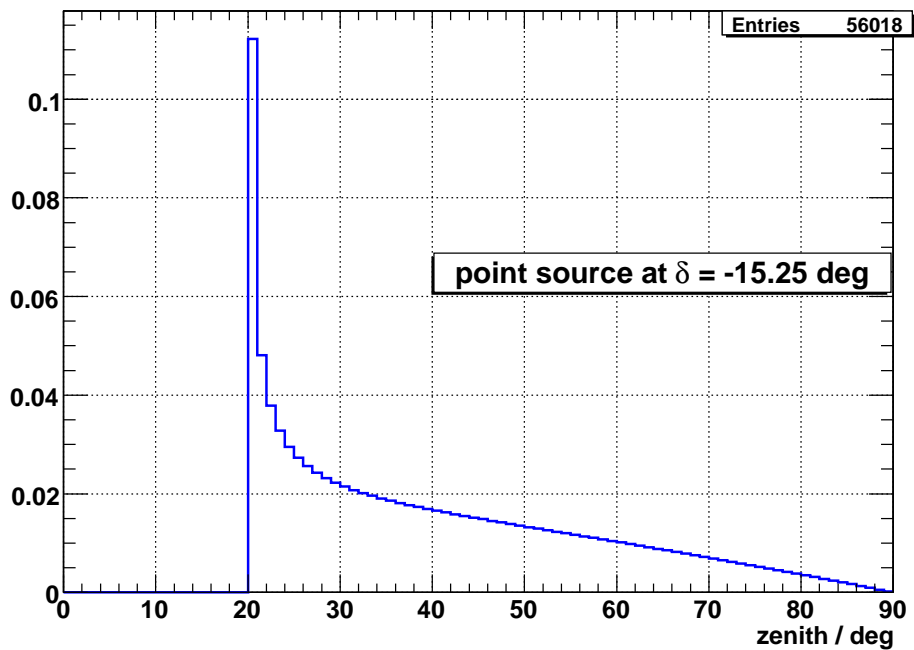
In order to display a representative part of the accessible celestial directions for the PAO, certain values of equatorial declination have been selected to compute the zenith angle distributions for. These values are indicated in table 7.1. The bottom row shows the position of the source relative to the observatory, i.e. to the declination corresponding to a zenith angle of $\theta \equiv 0$ from the PAO's point of view. In this case, the geographic latitude of the PAO simply becomes the declination value.

declination $\delta / ^\circ$	4.75	-15.25	-35.25	-55.25	-75.25	[-90 : 90]
rel. to PAO / $^\circ$	+40	+20	0	-20	-40	± 90

Table 7.1: Declination values of the fake point sources selected



(a) Zenith angle distribution for fake source at $\delta = 4.75^\circ$



(b) Zenith angle distribution for fake source at $\delta = -15.25^\circ$

Figure 7.1: Zenith angle distributions as being measured for fake point sources located at declinations of $\delta = 4.75^\circ$ (a) and $\delta = -15.25^\circ$ (b).

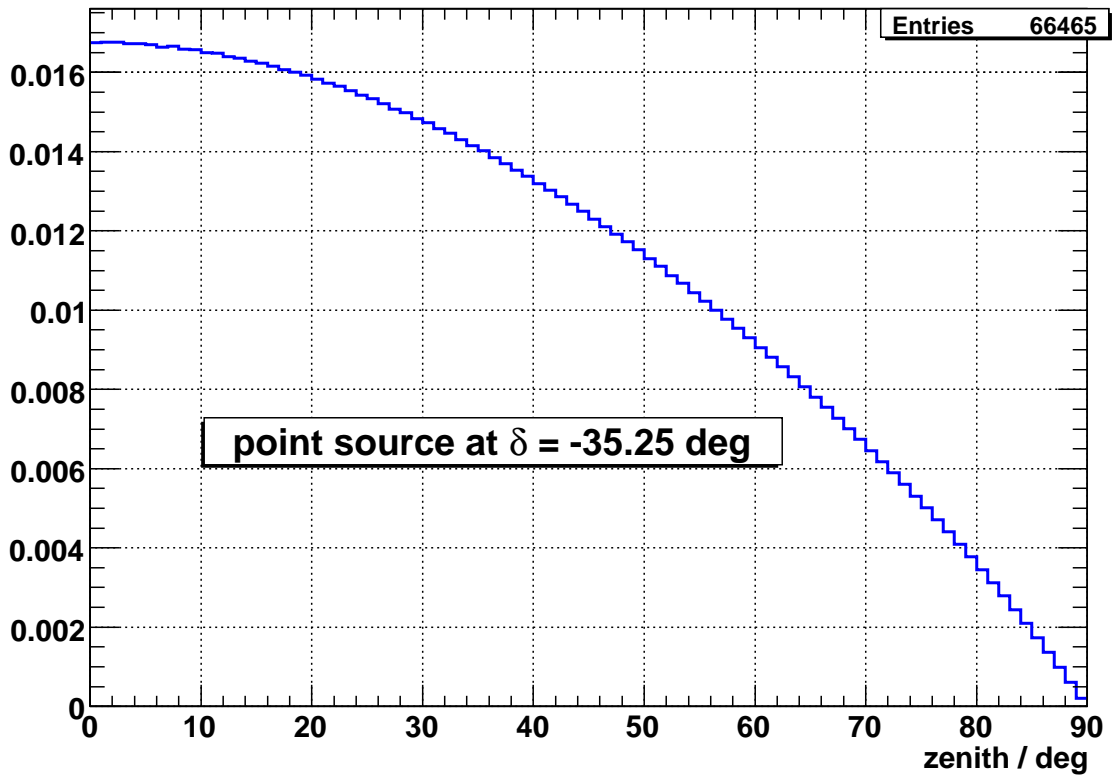


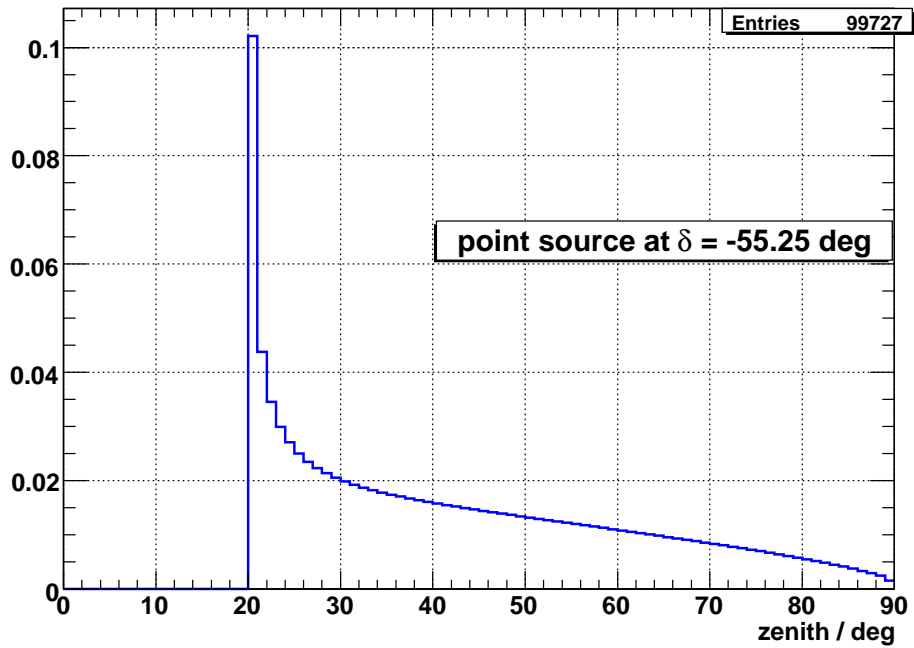
Figure 7.2: Zenith angle distribution as being measured for a fake source located at a declination of $\delta = -35.25^\circ$.

7.2 Zenith Angle Distributions

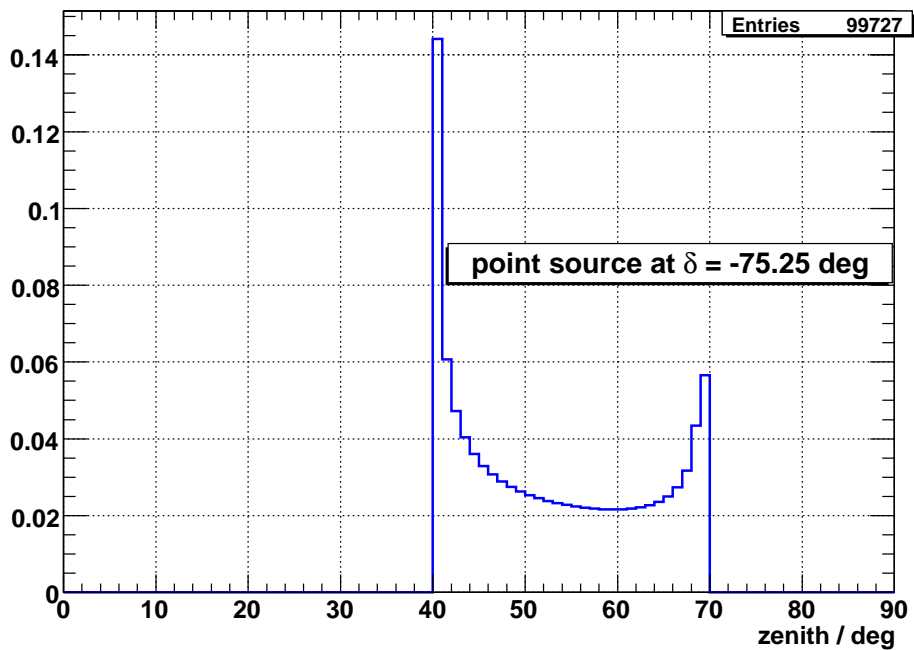
The raw zenith angle distributions for the respective fake point sources are displayed in figures 7.1 - 7.4. Assuming that all sources create cosmic rays at energies above full trigger efficiency, only a geometric factor of the SD acceptance is taken into account when producing these plots: $\cos(\theta)$ allows for the effective area of the surface detector. Figure 7.1 shows the zenith angle distribution for a point source located 40° (upper histogram) and 20° (bottom) north in declination relative to the PAO. The cut-off of the zenith angle at the corresponding value is clearly visible.

A fake object generated at the same position as the PAO, i.e. at a declination of $\delta = -35.25^\circ$, covers the full zenith angle range, as shown in figure 7.2. It has to be mentioned that this case represents a singularity, as the width of the right ascension line for $\delta \equiv -35.25^\circ$ is zero (as it is for any other discrete line); this is the only declination value, that causes entries at zero zenith angle $\theta = 0$, i.e. at zero solid angle.

Figure 7.3 indicates the lower limit of the zenith angle accessible for fake point sources located at 20° (upper histogram) and 40° (bottom) south in declination relative to the PAO. Furthermore, the plot for a source at $\delta = -75.25^\circ$ shows an upper limit for the zenith angle as well. This results from the fact that an object below $\delta < -54.75^\circ$, can be



(a) Zenith angle distribution for fake source at $\delta = -55.25^\circ$



(b) Zenith angle distribution for fake source at $\delta = -75.25^\circ$

Figure 7.3: Zenith angle distributions as being measured for fake point sources located at declination of $\delta = -55.25^\circ$ (a) and $\delta = -75.25^\circ$ (b).

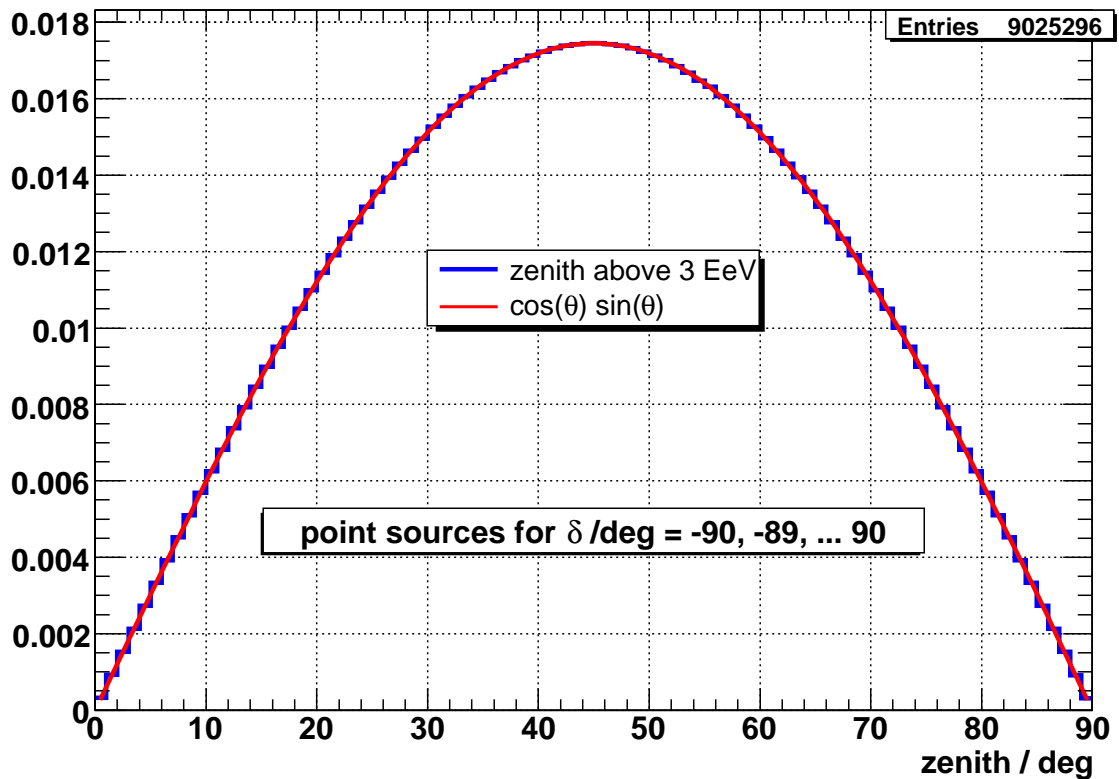


Figure 7.4: Zenith angle distribution (blue) as being measured for isotropically distributed fake sources located at discrete integral values of declinations. The overlaid function (red) represents the purely geometric acceptance effects, $\cos(\theta) \cdot \sin(\theta)$.

observed by the PAO permanently, if no zenith angle cut is applied. As mentioned before, this corresponds to a cone with angular radius of 35.25° . Otherwise, for the typical cut, $\theta < 60^\circ$, the declination limit for continuous observation is $\delta < -84.75^\circ$, corresponding to a cone of 5.25° opening angle.

Figure 7.4 finally shows the zenith angle distribution for the superposition of sources located equidistantly in latitudinal steps of $\Delta\delta = 1^\circ$: Fake point sources have been created for all integer values of declination, and have been forced to emit cosmic rays every ~ 8.64 seconds through the period of one sidereal day. To this end, the solid angle in equatorial coordinates has been allowed for by weighting all entries with a factor of $\cos(\delta)$. The resulting distribution agrees perfectly with the expected geometric acceptance indicated by the overlaid function (red) of simply $\cos(\theta) \cdot \sin(\theta)$.

7.3 Conclusions

In this chapter, zenith angle distributions have been generated for five discretely located point sources emitting cosmic rays every few seconds. The zenith angle range for each

of the sources has been displayed and the limits have been explained. Secondly, fake isotropy has been created by point sources distributed equidistantly in declination, providing the expected result of a purely geometrically explainable zenith angle distribution. As assumed already before from the zenith angle distribution obtained from real data above full acceptance, figure 5.4, showers with energies that provide negligible deflection and full trigger efficiency support the idea of a geometric acceptance under the assumption of isotropically distributed sources. This interpretation is especially assisted by the fact, that zenith angle distributions obtained from single fake point sources do not indicate such purely geometric behavior at all.

The next step would be to create a coverage map biased by a (few) point source(s) and, furthermore, investigate their impact on the zenith angle distribution. The latter, however, is expected to be rather small, especially in case of sources that cover almost the full zenith angle range accessible, i.e. sources located close to the observatory in terms of declination. Contrariwise, sources located at larger angular distance are supposed to more likely introduce anisotropy into the coverage maps; e.g. a source situated in the part of the sky that is continuously observable from the PAO's point of view contributes more strongly to the rather limited zenith angle range.

Chapter 8

Summary and Outlook

The aim of this thesis was to present coverage computation methods for the surface detector of the Pierre Auger Observatory. The results have been displayed and exploited for further investigation of the characteristics of these maps. All methods described do not allow to judge the absolute quality of coverage maps, i.e. whether they provide good expectation values for the number of events arriving from a certain direction; however, they allow to judge the compliance of the coverage to the assumption of isotropy.

In chapter 5, currently used coverage computation methods have been described. The shuffling technique has been presented as well as a semi-analytical approach that contained two different fit functions for the zenith angle distribution. Both the raw and the so-called FAM-based versions have been computed for each method. Computations have been performed both for all data in a first step and for a set of events at energies above 3 EeV, corresponding to full detector acceptance and shower trigger efficiency. The zenith angle distribution of the latter provided good agreement with the expectation of purely geometric acceptance effects, accounting for the solid angle via $\sin(\theta)$ and the effective area of the detector via $\cos(\theta)$, respectively.

An inherent quality check has been introduced in chapter 6. One aspect of the assumption of isotropy, understood as a precondition for any coverage computation, is the independence of the expected number of events on right ascension. Thus, averaging of the expectation has been performed on lines of constant declination. Subsequently, a method to compare a raw map and its one-dimensionally smoothed equivalent has been presented; the results in turn allowed a comparison of the various coverages.

Even though somewhat expected, it is remarkable that the FAM-based versions of the coverage computation methods perform slightly better with respect to the relative error of the mean obtained from averaging. Furthermore, the shuffling technique produces slightly worse results, than the semi-analytical ones. Considering the profiles of the coverage maps, i.e. the expected number of events as a function of declination, a feature has been found around the southpole region; all techniques show a discontinuity at $\sim -85^\circ$ declination, corresponding to the transition from the “sometimes” to the continuously visible part of the sky below $\delta = -85^\circ$.

Moreover, the averaging procedure can be considered as a tool that is capable of improving the coverage maps, as it only processes the impact of the isotropy assumption without introducing bias on the declination profile which could happen when applying a two-dimensional smoothing.

Finally, fake sources have been created in order to investigate their zenith angle distributions. It has been shown, that the range of accessible zenith angles can be limited according to the declination of the respective source. An isotropic distribution of point sources has been generated as well proving, that detector acceptance above full shower trigger efficiency only is limited by geometric conditions, i.e. solid angle and effective detection area.

Further investigation of the effect of fake anisotropy in terms of point sources on coverage computation may provide interesting results. To this end, it is necessary to create a certain number of fake events arriving from a defined celestial position; in a first approach, this could be done under the assumption that no loss of directional information occurs. Making use of the shuffling method for example, the extracted parameters, i.e. zenith angle and Julian day of these events would be filled into the appropriate lists. Thus, the existence of a small scale anisotropy is simulated, and one can investigate its impact on the coverage map as a function of the number of faked events related to the amount of real showers. Then, maps resulting from this procedure could be compared both among one another and with the underlying coverage map that has been obtained from shuffling only real events.

It should be mentioned again, that the approach for calculating the spread of the relative difference in chapter 6 is only a first attempt; it may be wiser to plot

$$\frac{N_{i,j} - \text{mean}_i}{\sqrt{\text{mean}_i}}, \quad (8.1)$$

instead of using equation 6.1 for the following reasons:

- This value is independent of both the number of entries and the number of pixels.
- For a map of real events only, e.g. figure 5.1, the expected value for the spread of the distribution obtained from equation 8.1 is 1.
- Thus, the value of the spread obtained for coverage maps in turn would yield another measure of its inherent smoothness, i.e. the inclusion of the precondition of isotropy.

Therefore, this issue is subject to further investigation as well.

Appendix A

Factorizable Acceptance Model

The Factorizable Acceptance Model (FAM, by Antoine Letessier-Selvon, [LS05]) is based on the hypothesis, that the domain of the variables (θ , ϕ and X , with X representing a set of physical parameters, like energy) covered by the detector, can be split in complementary regions over which the time part of the acceptance can be factorized. Over each such region we have the property:

$$A_{a,\Omega}(j, s, \theta, \phi, X) = A(j, s) \times A_{\Omega}(\theta, \phi, X), \quad (\text{A.1})$$

with $A(j, s)$ dimensionless and $A_{\Omega}(\theta, \phi, X)$ an area times a solid angle. In the FAM one assumes that the time variations of the acceptance is the product of a daily variation $E_s(s)$ in solar time s and a seasonal variation $E_j(j)$ in Julian days j as integers within a year; these functions are normalized dimensionless efficiency corrections. With A_0 the size of the detector averaged over the data taking period considered one can write

$$A(j, s) = A_0 \varepsilon_j(j) \times \varepsilon_s(s). \quad (\text{A.2})$$

This factorizability can be argued for by the fact, that daily variations are not subject to the particular day, but to the solar time of this day. The cosmic ray flux integrated over one of the regions mentioned above in units of number of particles per unit time depends on the sidereal time ST only

$$F(ST) = \int_{X_1} \int_{\Omega_1} A_{\Omega}(\theta, \phi, X) F_{\Omega}(j, s, \theta, \phi, X) dX d\Omega. \quad (\text{A.3})$$

The rate of cosmic ray detections is a function of time as well and can be written as

$$R(j, s) = A(j, s) \times F(ST) \quad (\text{A.4})$$

The assumption, that acceptance correction along the day D or the year Y , respectively, as well as possible anisotropies in the sky, are small, allows the development of the functions given by equations A.2 to A.4 around their mean values. Furthermore, correction factors are supposed to be small compared to one, which leads to the following equations for efficiency functions and flux:

$$E_j(j) = \frac{1}{Y}(1.0 + \varepsilon_j(j)), \quad (\text{A.5})$$

$$E_s(s) = \frac{1}{D}(1.0 + \varepsilon_s(s)), \quad (\text{A.6})$$

$$F(ST) = F_0(1.0 + \varepsilon_f(ST)), \quad (\text{A.7})$$

with F_0 the average of the integrated cosmic ray flux over a sidereal day in number of particles per unit time. By definition it is $\int_D \varepsilon_s(s) ds = 0$ and $\int_Y \varepsilon_j(j) dj = 0$, as well as $\int_D \varepsilon_f(ST(j,s)) ds \simeq 0$ and $\int_Y \varepsilon_f(ST(j,s)) dj \simeq 0$ due to the respective periodicity of the ε -functions. Thus, the rate of cosmic rays detected is

$$R(j,s) = \frac{A_0 F_0}{YD} (1.0 + \varepsilon_j(j) + \varepsilon_s(s) + \varepsilon_f(ST) + O(\varepsilon^2)). \quad (\text{A.8})$$

In first order approximation, this can be expressed split as

$$R_j(j) = \int_D R(j,s) ds = \frac{A_0 F_0}{Y} (1.0 + \varepsilon_j(j) = A_0 F_0 E_j(j)), \quad (\text{A.9})$$

$$R_s(s) = \int_Y R(j,s) dj = A_0 F_0 D (1.0 + \varepsilon_s(s) = A_0 F_0 E_s(s)). \quad (\text{A.10})$$

The only information contained in these equations are detector efficiency functions, and no anisotropy possibly present on the sky is included. The left hand side shows simply the distributions of seasonal time j within a year and solar time s within a day, that both are provided by the data itself. The main result for an approximation at first order is

$$A(j,s) \propto R_j(j) \times R_s(s) \quad (\text{A.11})$$

The estimations shown are valid for an almost constant detector size and acceptance in time. However, the growth of the PAO SD is monitored by the so-called T2 data files, that store information on the T2 trigger rates of the individual local station [Bon06a]. By means of these files, the instantaneous detector size can be calculated easily, as every second the number of active hexagons in the array is recorded. With $A_0 S(j,s)$ the weight extracted from the T2 files, equation A.4 can be rewritten:

$$R(j,s) = \tilde{A}(j,s) \times F(ST) = A_0 S(j,s) A(j,s) F(ST). \quad (\text{A.12})$$

Basically the same hypothesis and steps then lead to the following full variation of the detector acceptance

$$\tilde{A}(j,s) \propto R'_j(j) \times R'_s(s) \times S(j,s) \quad (\text{A.13})$$

The idea of factorizing the detector acceptance provides an efficient tool for coverage computation, through taking into account both daily and seasonal variations.

List of Figures

1.1	Cosmic ray energy spectrum	3
1.2	Schematic view of an extensive air shower	5
2.1	Map of the Pierre Auger Observatory	10
2.2	Surface detector tank	12
2.3	Hybrid detection principle	13
2.4	Zenith angle distribution for events satisfying the T4 condition	15
2.5	Trigger efficiency depending on signal size, zenith angle and core distance	16
2.6	SD reconstructed shower	17
2.7	SD energy calibration by means of hybrid data	19
3.1	Example of analyzed FADC trace of station signal	23
3.2	SD angular resolution	25
4.1	Horizontal coordinate system	29
4.2	Equatorial coordinate system	30
4.3	Galactic coordinate system	32
4.4	HEALPix pixelization for various resolutions	33
5.1	Skymap of events	36
5.2	Azimuth angle distribution and cuts	38
5.3	Julian day distributions	41
5.4	Zenith distribution with polynomial and physical fit	44
5.5	Comparison of zenith angle fits	46
5.6	Coverage maps for various coverage computation methods	47
5.7	Zenith distribution with polynomial and physical fit above full efficiency .	49
5.8	Comparison of zenith angle fits above full efficiency	51
5.9	Coverage maps above full acceptance for various coverage computation methods	53
6.1	Coverage maps after averaging on lines of constant declination	56
6.2	Declination profiles for physical fit, and relative difference between raw and FAM-based versions of one method	58
6.3	Declination profiles for FAM-based methods	59
6.4	Relative error of mean from declination profiles: raw vs. FAM	61
6.5	Relative error of mean from declination profile: shuffling vs. semi-analytical	62
6.6	Galactic coverage map	63
6.7	Galactic coverage map above full acceptance	63

7.1	Zenith angle distribution for fake sources at $\delta = 4.75^\circ$ and $\delta = -15.25^\circ$.	66
7.2	Zenith angle distribution for fake source at $\delta = -35.25^\circ$	67
7.3	Zenith angle distribution for fake sources at $\delta = -55.25^\circ$ and $\delta = -75.25^\circ$	68
7.4	Zenith angle distribution for isotropically distributed fake sources $-90^\circ <$ $\delta < 180^\circ$	69

List of Tables

1.1	Typical values for correlation between primary energy and particle flux	2
1.2	Integral composition of secondary particles	4
1.3	Muon production / decay of charged mesons	6
5.1	χ^2/dof -test results for various polynomial fits to the zenith angle distribution	43
7.1	Declination values of fake point sources	65

List of Acronyms

Acronym	Explanation
ADC	Analog-to-Digital Converter
AR	Angular Resolution
CDAS	Central Data Acquisition System
CIC	Constant Intensity Cut
CMB	Cosmic Microwave Background
EA	Engineering Array
EAS	Extensive Air Shower
FADC	Fast/Flash Analog-to-Digital Converter
FD	Fluorescence Detector
GPS	Global Positioning System
GZK	Greisen-Zatsepin-Kuzmin
HEALPix	Hierarchical, Equal Area, and iso-Latitude Pixelisation (of the sphere)
HERALD	data files, that contain reconstructed parameters of showers measured by the PAO SD
JD	Julian Day
LDF	Lateral Density Function
LST	Local Sidereal Time
LTP	Lateral Trigger Probability
MC	Monte Carlo
NKG	Nishimura-Kamata-Greisen
PAO	Pierre Auger Observatory
PMT	Photo Multiplier Tube
RMS	Root Mean Square
SD	Surface Detector
ST	Sidereal Time
UHECR	Ultra High Energy Cosmic Rays
UT	Universal Time
UTC	Universal Time Coordinated

Bibliography

- [Abr04] J. A. Abraham (Pierre Auger Collaboration), *Properties and performance of the prototype instrument for the Pierre Auger Observatory*, Nucl. Instr. Meth. **A523** (2004), 50–95.
- [Alk75] O. C. Alkhofer, *Introduction to Cosmic Radiation*, Verlag Carl Thieme, 1975.
- [All05] P. S. Allison (Pierre Auger Collaboration), *Calibration of the surface array of the Pierre Auger Observatory*, Proc. ICRC 2005, 2005.
- [All06] D. Allard, M. Ave, N. Busca, A. Chou, C. Newman-Holmes, P. Privitera, G. Rodriguez, A. Watson, T. Yamamoto, and E. Zas (Pierre Auger Collaboration), *A guide-line to the Auger-Surface-Detector Analysis*, GAP-Note 2006-024, internal report, not for public display, 2006.
- [Arm04] E. Armengaud, T. Beau, P. Billoir, P. D. Silva, O. Deligny, J.-C. Hamilton, C. Lachaud, A. Letessier-Selvon, C. Medina, and B. Revenu (Pierre Auger Collaboration), *First Auger angular power spectrum estimate II/III - Effects of weather conditions on the SD acceptance at low energies*, GAP-Note 2004-041, internal report, not for public display, 2004.
- [Ask65] G. A. Askaryan, 1965, p. 658.
- [Aug38] P. Auger, P. Ehrenfest, R. Maze, J. Daudin, Robley, and A. Fréon, *Extensive Cosmic-Ray Showers*, Rev. Mod. Phys. **11** (1938), 288–291.
- [Bau03] P. Bauleo and J. Harton (Pierre Auger Collaboration), *Auger Surface Detector Tank Trigger Efficiency*, GAP-Note 2003-055, internal report, not for public display, 2003.
- [Bil02] P. Billoir (Pierre Auger Collaboration), *Parametrization of the Relation between Primary Energy and $S(1000)$ in Surface Detector*, GAP-Note 2002-075, internal report, not for public display, 2002.
- [Bon05] C. Bonifazi (Pierre Auger Collaboration), *Angular resolution of the Pierre Auger Observatory*, Proc. ICRC 2005, 2005.
- [Bon06a] C. Bonifazi and P. L. Ghia (Pierre Auger Collaboration), *Selection of data periods and calculation of the SD geometrical acceptance*, GAP-Note 2006-101, internal report, not for public display, 2006.

- [Bon06b] C. Bonifazi and A. Letessier-Selvon (Pierre Auger Collaboration), *Angular Resolution of the Auger Surface Detector*, GAP-Note 2006-016, internal report, not for public display, 2006.
- [d'005] B. R. d'Orfeuil, J.-C. Hamilton, and B. Revenu (Pierre Auger Collaboration), *Comparison of the coverage estimation methods in the presence of anisotropies and acceptance effects*, GAP-Note 2005-083, internal report, not for public display, 2005.
- [Fal03] H. Falcke and P. W. Gorham, *Detecting Radio Emission from Cosmic Ray Air Showers and Neutrinos with a Digital Radio Telescope*, *Astropart. Physics* **19** (2003), 477.
- [Fer07] Pierre Auger Collaboration, 2007, online accessed 12.06.2007, http://www.fnal.gov/pub/presspass/press_releases/Auger_photos/auger-design-graphic.jpg.
- [Gor05a] K. M. Gorski, E. Hivon, A. J. Banday, B. D. Wandelt, F. K. Hansen, M. Reinecke, and M. Bartelman, *HEALPix – a Framework for High Resolution Discretization, and Fast Analysis of Data Distributed on the Sphere*, *The Astrophysical Journal* **622** (2005), 759.
- [Gor05b] K. M. Gorski, B. D. Wandelt, E. Hivon, F. K. Hansen, and A. J. Banday, *The HEALPix Primer*, 2005.
- [Gre56] K. Greisen, *Progress in Cosmic Ray Physics*, vol. 3, 1956.
- [Gre66] K. Greisen, *End to the Cosmic-Ray Spectrum?*, *Phys. Rev. Lett.* **16** (1966), 748.
- [Gru00] C. Grupen, *Astroteilchenphysik - Das Universum im Licht der kosmischen Strahlung*, Friedr. Vieweg & Sohn Verlagsgesellschaft mbH, Braunschweig/Wiesbaden, 2000.
- [Gru05] C. Grupen, *Astroparticle Physics*, Springer-Verlag Berlin Heidelberg, 2005.
- [Ham04] J.-C. Hamilton, E. Armengaud, T. Beau, P. D. Silva, O. Deligny, C. Lachaud, A. Letessier-Selvon, C. Medina, B. Revenu, and B. R. d'Orfeuil (Pierre Auger Collaboration), *First Auger angular power spectrum estimate I/III - A method for computing the Auger coverage map directly from the event dataset*, GAP-Note 2004-040, internal report, not for public display, 2004.
- [Ham05] J.-C. Hamilton (Pierre Auger Collaboration), *Coverage and large scale anisotropies estimation methods for the Pierre Auger Observatory*, Proc. ICRC 2005, 2005.
- [Hes12] V. F. Hess, *Über Beobachtungen der durchdringenden Strahlung bei sieben Freiballonfahrten*, *Phys. Z.* (1912), no. 13, 1084–1091.

- [Hil71] A. M. Hillas (Pierre Auger Collaboration), *Measurement of Primary Energy of Air Showers in the Presence of Fluctuations*, vol. 3, Proc. ICRC 1971, 1971, p. 1001.
- [Hor06] A. Horneffer, *Measuring Radio Emission from Cosmic Ray Air Showers with a Digital Radio Telescope*, Ph.D. thesis, 2006.
- [Kah66] F. D. Kahn and I. Lerche, *Radiation from Cosmic Ray Air Showers*, vol. 289, 1966, pp. 206–213.
- [Kam04] K.-H. Kampert (Pierre Auger Collaboration), *The Pierre Auger Observatory -Status and Prospects-*, Proc. XIII ISVHECRI, Pylos (Greece), 2004.
- [Lhe03] I. Lhenry, E. Parizot, D. Allard, P. Ghia, J. Aublin, and T. Suomijarvi (Pierre Auger Collaboration), *The Lateral Trigger Probability function (LTP) for UHE Showers detected by the Pierre Auger Observatory Surface Detector*, GAP-Note 2003-088, internal report, not for public display, 2003.
- [lib06] Celestial Mechanics, Astrometry and Astrodynamics Library Collaboration, 2006, online accessed January 2007, <http://libnova.sourceforge.net/>.
- [Lon92] M. S. Longair, *High energy astrophysics*, vol. 1, Cambridge University Press, 1992.
- [LS05] A. Letessier-Selvon (Pierre Auger Collaboration), *Detector studies and Coverage estimation with the Factorizable Acceptance Model (FAM)*, GAP-Note 2005-097, internal report, not for public display, 2005.
- [LY05] I. Lhenry-Yvon (Pierre Auger Collaboration), *The trigger system of the Pierre Auger Surface Detector: operation, efficiency and stability*, Proc. ICRC 2005, 2005.
- [Man05] P. Mantsch (Pierre Auger Collaboration), *The Pierre Auger Observatory - Progress and First Results*, Proc. ICRC 2005, 2005.
- [Mee91] J. Meeus, *Astronomical Algorithms*, Willmann-Bell Inc., 1991.
- [Mos05] M. A. Mostafá (Pierre Auger Collaboration), *The Hybrid Performance of the Pierre Auger Observatory*, Proc. ICRC 2005, 2005.
- [Nag00] M. Nagano and A. A. Watson, *Observations and implications of the ultrahigh-energy cosmic rays*, Rev. Mod. Phys. **72** (2000), 689–732.
- [New05] D. Newton, J. Knapp, and A. Watson (Pierre Auger Collaboration), *The Optimum Ground Parameter, $S(r_{opt})$* , GAP-Note 2005-013, internal report, not for public display, 2005.
- [PAO07] Pierre Auger Collaboration, 2007, online accessed 12.06.2007, <http://www.auger.org.ar/survey/Ozi/sd-array-full-1673-SD-20041116.jpg>.

- [Par05] E. Parizot (Pierre Auger Collaboration), *Aperture Calculation of the Pierre Auger Observatory surface detector*, Proc. ICRC 2005, 2005.
- [PDR97] Pierre Auger Collaboration, *Pierre Auger Project Design Report*, 1997, Second Edition - November 1996; Revised - March 1997.
- [Pen65] A. Penzias and R. W. Wilson, *A Measurement of Excess Antenna Temperature at 4080 Mc/s*, Ap. J. **142** (1965), 419–421.
- [Pri03] P. Privitera (Pierre Auger Collaboration), *The Angular Reconstruction and Angular Resolution of Air Showers Detected at the Auger Observatory*, Proc. ICRC 2003, 2003.
- [Rao98] M. V. S. Rao and B. V. Streekantan, *Extensive Air Showers*, World Scientific Publishing Co. Pte. Ltd., 1998.
- [Rot07] M. Roth (Pierre Auger Collaboration), *Measurement of the UHECR energy spectrum using data from the Surface Detector of the Pierre Auger Observatory*, Proc. ICRC 2007, 2007.
- [San07] E. M. Santos, 2007, private communication.
- [Sil03] P. D. Silva and A. Letessier-Selvon (Pierre Auger Collaboration), *Status and proposal for the shower direction reconstruction*, GAP-Note 2003-012, internal report, not for public display, 2003.
- [Tak99] M. Takeda, *Small Scale Anisotropy of Cosmic Rays above 10 EeV Observed with the Akeno Giant Air Shower Array*, Ap. J. **522** (1999), 225–237.
- [Veb05] D. Veberic and M. Roth (Pierre Auger Collaboration), *Offline Reference Manual - SD Reconstruction*, GAP-Note 2005-035, internal report, not for public display, 2005.
- [Wul09] T. Wulf, *Über die in der Atmosphäre vorhandene Strahlung von hoher Durchdringungsfähigkeit*, Phys Z. **10** (1909), 152–157.
- [Yam07] T. Yamamoto (Pierre Auger Collaboration), *The UHECR spectrum measured at the Pierre Auger Observatory and its astrophysical implications*, Proc. ICRC 2007, 2007.

Acknowledgement

My gratefulness goes out to all those, who made this thesis possible.

Firstly, I would like to thank Prof. Dr. Ivor Fleck for the opportunity to take part in the research for the Pierre Auger Observatory. It has been a great experience working on this exciting experiment.

I am thankful to Prof. Dr. Claus Grupen as well, for agreeing to revise this thesis and for arousing and encouraging my interest in astroparticle physics during the advanced laboratory courses.

Furthermore, I would like to thank all collaboration members I met and had fruitful discussions with, e.g. during the collaboration meetings in Argentina. I want to thank especially the local staff, who made my FD shift in Malargüe a very pleasant and instructive time.

Thanks to all the people of the high energy particle physics group at the physics department of the University of Siegen. I was close to dedicating a whole section to specify my gratefulness to Thomas Bäcker, Dr. Marc Brüggemann and Dirk Kickelbick; thank you for proofreading, questioning and discussing the contents of my thesis over several cups of coffee after lunch.

My gratitude also goes to my friends in Oberberg for everything you are, just friends. Special thanks to Julia, for your incredible patience, peace, love, empathy.

Last but not least, I am proud to express my gratefulness to my family. My parents and brothers have been and still are an important part of my personality, providing a base of tranquility during the previous 27 years. Thanks for your support!

Erklärung

Hiermit versichere ich, dass ich diese Arbeit selbstständig verfasst habe und keine anderen als die angegebenen Quellen und Hilfsmittel benutzt habe.

Marius Grigat

